UNIVERSITY OF TURIN

DOCTORAL SCHOOL OF
SCIENCES AND INNOVATIVE TECHNOLOGIES

PHD PROGRAMME IN
AGRICULTURAL, FOREST AND FOOD SCIENCES

CYCLE: XXXIV

DETECTION AND ASSESSMENT OF FOREST DISTURBANCE DYNAMICS AT THE LANDSCAPE SCALE BASED ON REMOTE SENSING AND FIELD DATA

Donato Morresi

Supervisor:
Prof. Matteo Garbarino

Cycle coordinator:
Prof. Eleonora Bonifacio

YEARS
2019; 2020; 2021

Acknowledgments

I am deeply thankful to my supervisor, Professor Matteo Garbarino, for giving me the opportunity to do research on what I am passionate about. I truly appreciated his continuous support and vivid enthusiasm in the research projects I was involved in during the last few years. Collaborating with him has always been very pleasant and fruitful. I am also very grateful to him for providing me with financial support throughout the PhD course.

I would like to thank my colleagues and the other people at the Department of Agricultural, Forest and Food Sciences at the University of Torino, with whom I enjoyed working and exchanging ideas throughout these years. In particular, I give special thanks to Raffaella Marzano, Fabio Meloni, Emanuele Sibona, Giulia Mantero and Nicolò Anselmetto for creating such a positive working environment.

Finally, I am especially grateful to my family and Arianna for always sustaining me and encouraging me in many different ways.

Abstract

Understanding temporal and spatial patterns of forest disturbance dynamics is becoming increasingly crucial due to global change-induced shifts of disturbance regimes. Anthropogenic climate change compounding with land-use change worsens the extent, frequency and severity of many natural disturbances. Furthermore, tree mortality triggered by exceptional drought and heat is increasing, with high impacts on carbon cycling and forest resilience. Remote sensing data like optical satellite imagery is a powerful tool for assessing forest disturbance dynamics at the landscape scale. Landsat imagery provides a unique opportunity for ecologists to track changes to forests over the last four decades. The recent Sentinel-2 mission expands the availability of medium-resolution multispectral imagery, complementing Landsat data. This thesis focuses on different aspects of forest disturbance dynamics: post-fire forest recovery, burn severity assessment and automated disturbance detection.

We first assessed post-fire forest spectral recovery in four wildfires occurred in the central Apennines in 2007, using inter-annual Landsat time series and field data. We evaluated the ability of different commonly used spectral indices to track ecological processes associated with the encroachment of forest regeneration and we proposed the use of a novel spectral index, the Forest Recovery Index 2 (FRI2). Results from different burn severity classes and forest types highlighted that the novel index we proposed was more sensitive to forest regeneration dynamics compared to other spectral indices.

Secondly, we developed a novel approach for mapping burn severity based on Sentinel-2 reflectance composites and bi-temporal indices. Our study areas were 10 wildfires occurred in the Piedmont region in 2017. Field data consisted of Composite Burn Index plots distributed across the burnt areas. Pre- and post-fire reflectance composites embedding long-term phenology metrics provided significantly higher classification accuracy compared to paired images. Improvements offered by phenologically coherent reflectance composites over

paired images were related to higher radiometric consistency and increased contrast between healthy and burnt vegetation.

Lastly, we present Change Detection by Multispectral Trends (CDMT), a Landsat time series-based automated algorithm for forest disturbance detection that exploits the full spectral information in Landsat imagery. CDMT segments inter-annual multispectral time series to detect both abrupt and gradual changes using a novel statistical procedure. We tested CDMT in the Aosta Valley region (Italy) and analysed trends in disturbances over a 34-year period. Our results highlighted that the user's and producer's accuracy of the disturbed class systematically increased when moving from the univariate to the multivariate setting. The inclusion of multiple bands, i.e. both original spectral bands and indices, allowed CDMT to leverage complementary information carried by different portions of the electromagnetic spectrum. Moreover, CDMT was sensitive toward an ample range of disturbance severities. For instance, it effectively captured abrupt and gradual changes associated with drought-induced tree mortality.

Table of contents

Acknowledgments ..... **i**

Abstract ..... **ii**

Table of contents ..... **iv**

Chapter 1 ..... **8**

Introduction **8**

1.1 Forest recovery 8

1.2 Burn severity 10

1.3 Disturbance detection 12

1.4 Thesis objectives and outline 14

References 15

Chapter 2 ..... **27**

Forest spectral recovery and regeneration dynamics in stand-replacing wildfires of central Apennines derived from Landsat time series **27**

Abstract 27

2.1 Introduction 28

2.2 Materials and methods 31

2.2.1 Study areas 31

2.2.2 Dataset and preprocessing 34

2.2.3 Fire perimeter and burn severity assessment 35

2.2.4 Area of interest within fire perimeters 36

2.2.5 Spectral vegetation indices 37

2.2.6 Field data and SVI correlation 39

2.2.7 Post-fire recovery metrics and temporal trajectories 39

2.2.8 Statistical analysis of recovery trends 40

2.3 Results 42
2.3.1 Relationship between field data and Landsat-derived SVIs . 42
2.3.2 Temporal trajectories of post-fire RDSVIs 43
2.3.3 Percentage of SVI recovered pixels 44
2.3.4 Long-term trends of RDSVIs 45
2.4 Discussion 48
2.4.1 Main differences between SVIs when tracking forest spectral recovery dynamics 48
2.4.2 Forest spectral recovery of different burn severity classes and forest types 50
2.4.3 Forest spectral recovery time derived from monotonic trends 50
2.5 Conclusions 52
Acknowledgments 53
References 53
Supplementary material 64
Chapter 3 68
Mapping burn severity in the western Italian Alps through phenologically coherent reflectance composites derived from Sentinel-2 imagery 68
Abstract 68
3.1 Introduction 70
3.2 Materials and Methods 75
3.2.1 Study area 75
3.2.2 General overview 77
3.2.3 Satellite data and preprocessing 78
3.2.4 Field data 80
3.2.5 Fire severity 81

3.2.6 Burn severity 82
3.2.7 Sentinel-2 reflectance composites 82
3.2.8 Weighting system 84
3.2.9 Evaluation of long-term LSP metrics and radiometric consistency of reflectance composites 87
3.2.10 Classification and validation of burn severity maps 88
3.3 Results 89
3.3.1 Reflectance composites 89
3.3.2 Regression models 94
3.3.3 Burn severity maps 96
3.4 Discussion 100
3.4.1 Reflectance composites 100
3.4.2 Burn severity mapping 102
3.5 Conclusions 105
Acknowledgments 106
Data availability statement 106
References 107
Supplementary material 119
Chapter 4 126
Change detection by multispectral trends: a Landsat time series-based algorithm for forest disturbance mapping and beyond 126
Abstract 126
4.1 Introduction 127
4.2 Materials and methods 132
4.2.1 Study area 132
4.2.2 Landsat data 133
4.2.3 Overview of the algorithm 135
4.2.4 Processing of multispectral time series 136

4.2.5 Impulsive noise filter 137
4.2.6 Modified HiTS procedure 137
4.2.7 Classification of changepoints 141
4.2.8 Spectral change magnitude and disturbance severity 142
4.2.9 Algorithm parametrisation 143
4.2.10 Accuracy assessment 144
4.3 Results 146
4.3.1 Algorithm assessment: impulsive noise 146
4.3.2 Algorithm assessment: weights and change thresholds 149
4.3.3 Algorithm assessment: bands combinations 150
4.3.4 Disturbance detection and severity assessment in the Aosta Valley 155
4.3.5 Trends in forest disturbances in the Aosta Valley 159
4.4 Discussion 160
4.4.1 Assessment of the algorithm 160
4.4.2 Disturbance severity assessment and trends in forest disturbances 163
4.5 Conclusions 165
Data availability statement 165
Acknowledgments 166
References 166
Supplementary material 178
Chapter 5 183
Conclusions 183
References 184

Chapter 1

Introduction

1.1 Forest recovery

Forest recovery is an ecological process referring to the re-establishment or re-development of several forest structural properties, e.g. canopy cover, biomass, tree height, stand basal area (Bartels et al., 2016; Frolking et al., 2009; Senf et al., 2019). Post-disturbance recovery is crucial for evaluating the resilience of forest ecosystems in relation to shifts in disturbance regimes and provision of ecosystem services (Kulakowski et al., 2016; Seidl et al., 2016). Climate warming alters patterns of forest recovery, either directly or indirectly, by modifying disturbance regimes and the post-disturbance environment (Johnstone et al., 2016; Stevens-Rumann et al., 2018). For instance, increases in frequency, severity and size of disturbances reduce the availability of biological legacies, e.g. seed propagules, survived tree individuals and woody debris, which are key elements that drive patterns of tree regeneration (Bartels et al., 2016; Johnstone et al., 2016; Swanson et al., 2011). Moreover, hotter and drier conditions, associated with climate change that occurs after a disturbance, negatively impact forest recovery by hindering the establishment of tree regeneration (Johnstone et al., 2016; Rodman et al., 2020; Stevens-Rumann et al., 2018). Failures in forest recovery can lead to transitions into non-forest vegetation and trigger land degradation (Doblas-Miranda et al., 2017; Johnstone et al., 2016; Rodman et al., 2020). Therefore, post-disturbance management should primarily focus on facilitating early-successional forests (Donato et al., 2012). In particular, both spatial heterogeneity of forest landscapes (Turner, 2010) and stand structural complexity in early-seral stages (Donato et al., 2012) are key factors that promote forest recovery.

Optical satellite data at medium-resolution, such as multispectral Landsat imagery, has been long employed to assess post-fire vegetation recovery in Mediterranean-type ecosystems (e.g. Röder et al., 2008; Veraverbeke et al., 2012;

Viedma et al., 1997). Studies focusing on post-disturbance forest recovery were relatively recent, and typically employed multi decadal, inter-annual Landsat time series (e.g. Bolton et al., 2015; Kennedy et al., 2012; Schroeder et al., 2007; White et al., 2017). Tracking gradual spectral changes associated with forest recovery requires maximising spatial and spectral consistency of inter-annual Landsat time series. Fitting curves to spectral trajectories is effective to minimise inter-annual differences arising from phenological and atmospheric mismatches (Kennedy et al., 2010; Senf et al., 2019). The effectiveness of this approach depends on the enhancement of Landsat time series for reducing biases generated by outliers and missing data. Filtering residual noise (e.g. Kennedy et al., 2010), producing gap-free image composites (e.g. White et al., 2014) and inferring missing values through contextual analysis (e.g. Hermosilla et al., 2015) are among the main techniques. Most of the studies focusing on forest recovery employed original Landsat bands (Pickell et al., 2016) or spectral indices such as the Normalized Burn Ratio (NBR; Kennedy et al., 2012), the Tasseled Cap wetness (TCW; Senf et al., 2019) and the integrated forest z-score (IFZ; Zhao et al., 2016). The Shortwave Infrared (SWIR) bands are the most sensitive toward forest biomass and structure (Banskota et al., 2014; Pickell et al., 2016). Furthermore, spectral indices contrasting the SWIR bands and the near infrared (NIR) band have been extensively employed for tracking forest recovery (e.g. Kennedy et al., 2012; White et al., 2017). It is worth noting that forest recovery measured with spectral indices and bands is not directly related to the structural properties of the stands (Kennedy et al., 2012; White et al., 2017). Yet, recovery metrics derived from spectral indices and computed either in absolute or relative terms are useful indicators of short- to long-term forest recovery dynamics, providing information of spatial heterogeneity at the regional scale (e.g. Kennedy et al., 2012; White et al., 2017). Furthermore, several studies highlighted the effectiveness of disturbance and recovery metrics derived from Landsat time series for predicting stand structure when compared with LiDAR data, (e.g. Pflugmacher et al., 2012; Vogeler et al., 2016).

1.2 Burn severity

The severity of a disturbance event is defined as its ecological effect on organisms, communities and ecosystems and is directly related to the intensity of a disturbance (Turner, 2010). Along with frequency and size, severity is one of the main components of disturbance regimes, largely influencing the ecological responses of forest ecosystems (Johnstone et al., 2016; McDowell et al., 2020). Post-disturbance management strategies that promote forest resilience and the recovery of ecosystem services rely on the assessment of severity to address interventions (Leverkus et al., 2018). In fire ecology, the terms fire and burn severity are often used to indicate a different timing for the assessment of severity (Cansler and McKenzie, 2012; Lentile et al., 2006; Veraverbeke et al., 2010a). Fire severity refers to an initial assessment, i.e. within weeks after fire occurrence and within the same season, of the effects directly related to fire intensity, such as fuel consumption and instant tree mortality. The term burn severity is widely used in remote sensing applications (Keeley, 2009) and refers to an extended assessment of severity, i.e. during the first growing season following the fire. Burn severity includes both the effects of combustion and the initial ecosystem response, e.g. delayed tree mortality and survivorship (Key, 2006).

Key and Benson (2006) developed an operational approach for mapping burn severity at the landscape scale based on medium-resolution satellite imagery, i.e. Landsat data. Though this approach was initially developed for forests in the U.S., it has been successfully applied in different ecosystems globally, e.g. Soverel et al. (2011); Tanase et al. (2011); Veraverbeke et al. (2010a). The approach proposed by Key and Benson (2006) relies on integrating remote sensing-based change detection and field data collected using the Composite Burn Index (CBI) protocol. Specifically, the Normalized Burn Ratio (NBR; García and Caselles, 1991) derived from Landsat images acquired in the pre- and post-fire growing seasons is employed to compute several bi-temporal indices, i.e. the differenced Normalized Burn Ratio (dNBR; Key and Benson, 2006), the Relative dNBR (RdNBR; Miller and Thode, 2007) and the Relativized Burn Ratio (RBR; Parks

et al., 2014). Thresholding bi-temporal indices into ecologically relevant burn severity classes is performed by including field measures of burn severity, e.g. CBI scores, in parametric models (Key and Benson, 2006; Kolden et al., 2015). The CBI protocol has proven to be effective when compared with other measures of burn severity, such as the percentage change in tree canopy cover and tree basal area (Miller et al., 2009). Matched acquisition timing and optimal seasonal timing determine the effectiveness of bi-temporal indices in capturing fire-induced spectral changes while reducing the influence of external factors (Key, 2006; Miller and Thode, 2007; Veraverbeke et al., 2010b). These latter include plant phenology, solar elevation angle, differences in illumination due to topography, and moisture content. A method for minimising non-fire induced inter-annual changes is the calibration of bi-temporal indices based on spectral variations in unburnt areas outside fire perimeter (Key, 2006; Meddens et al., 2016; Miller and Thode, 2007; Parks et al., 2014). The optimal seasonal timing for pre- and post-fire image acquisition corresponds to early-to-middle growing season dates, as the vegetation reaches the peak in terms of photosynthetic activity (Eidenshink et al., 2007; Key, 2006; Picotte et al., 2020). Recently, limitations related to the availability of cloud-free image pairs with matched acquisition timing have been overcome through pixel-based compositing algorithms based on the complete set of Landsat images acquired during the growing season (Parks et al., 2018; Whitman et al., 2020). Frantz et al. (2017) produced pixel-based Landsat composites at the regional scale embedding spatial patterns of land surface phenology. They achieved phenological coherence of the land surface relative, for example, to the peak of the growing season. Among compositing approaches, those based on the median (Sagar et al., 2017) or multidimensional medians, e.g. the medoid (Flood, 2013) and the geometric median (Roberts et al., 2017), are robust towards invalid pixels that were missed by clouds and cloud shadows detection algorithms. Therefore, these algorithms produce spatially consistent image composites which can serve as input in several processing pipelines, e.g. Kennedy et al. (2018).

1.3 Disturbance detection

By altering state and trajectories of forest ecosystems, disturbances have a pivotal role in regulating spatiotemporal heterogeneity of these ecosystems (Turner, 2010). Disturbance regimes characterise temporal and spatial dynamics of disturbances, e.g. frequency, timing, size and severity, over long time periods (Johnstone et al., 2016; Turner, 2010). During recent decades, climate warming and land-use change caused shifts in disturbance regimes, intensifying frequency, size and severity of disturbance events and modifying their interactions (Johnstone et al., 2016; Mantero et al., 2020; McDowell et al., 2020; Seidl et al., 2017). Gradual and non-stand replacing disturbances such as forest decline associated with drought and heat waves, insect outbreaks and pathogens emerged as a pervasive phenomenon in many forest ecosystems (Allen et al., 2010; Cohen et al., 2016; Coops et al., 2020). The impact of non-stand replacing disturbances is expected to worsen with current trends of climate warming, significantly impairing forest carbon storage (Allen et al., 2015). The increased vulnerability of forests to climate-driven disturbances has strong implications for forest management (Leverkus et al., 2021). Increasing the resilience of forest ecosystems should be pursued in several ways, such as promoting tree growth through forest thinning or assisting the migration towards disturbance-adapted tree species (Allen et al., 2015; Leverkus et al., 2021; Seidl, 2014).

Landsat time series provide unprecedented opportunities for reconstructing forest disturbance dynamics over the last four decades thanks to their consistency in space, time and spectral characteristics (Kennedy et al., 2014; Wulder et al., 2019). A plethora of Landsat time series-based algorithms has been developed since the opening of the U.S. Geological Survey Landsat archive in 2008 (Wulder et al., 2012). These algorithms were aimed at automating the detection of either a broad range of land cover changes or forest disturbance dynamics (Zhu, 2017). Differences between automated algorithms were mainly related to the frequency of Landsat time series, i.e. intra- or inter-annual, and to the mathematical approach they rely on, e.g. thresholding, segmentation, statistical boundary (Zhu,

2017). Another characteristic discriminating between algorithms is the capability of analysing one spectral band/index per run, i.e. univariate approach, or multiple spectral indices/bands, i.e. multivariate approach. While many algorithms were developed to target both abrupt and gradual disturbances, several authors found that they struggle in detecting low-severity events (Cohen et al., 2020, 2017; Rodman et al., 2021). Noise in Landsat time series generated by uncertainties in preprocessing operations like geometric and atmospheric correction can mask the signal of low-severity events (Cohen et al., 2017; Rodman et al., 2021). Ensemble approaches like those proposed by Cohen et al. (2020, 2018) and Healey et al. (2018) were effective to improve forest disturbance maps produced with automated algorithms, e.g. LandTrendr (Landsat-based Detection of Trends in Disturbance and Recovery; Kennedy et al., 2018, 2010) and CCDC (Continuous Change Detection and Classification; Zhu et al., 2019). In particular, these studies combined results obtained using multiple spectral bands/indices and/or algorithms through a secondary classification based on a supervised classifier, e.g. random forest. Advantages offered by ensemble approaches depend on the complementary information provided either by different wavelengths, e.g. SWIR and NIR, or by different algorithms.

Aside from passive optical imagery, Synthetic Aperture Radar (SAR) data acquired by spaceborne radar sensors are effective for detecting forest disturbances such as windthrows (Rüetschi et al., 2019) and logging (Ruiz-Ramos et al., 2020; Ygorra et al., 2021). SAR data are particularly useful in geographic areas characterised by persistent cloud cover, e.g. the tropics, as they are not affected by the presence of clouds, thus enabling timely detection of changes to the forest cover. Nowadays, freely available SAR data, such as those acquired by the Sentinel-1 mission, prompted the development of automated algorithms for forest cover mapping and disturbance detection. Many studies based on SAR data employed bi-temporal change detection for mapping forest disturbances, e.g. Rüetschi et al., (2019). Recently, the detection of changepoints in time series of SAR data based on statistical methods like the Cumulative Sum (CUSUM),

emerged to be a powerful approach (Ruiz-Ramos et al., 2020; Ygorra et al., 2021).

In recent years, statistical methods for detecting changepoints in multivariate time series have gained interest because of their ability to analyse multivariate data arising in many disciplines (Cho and Kirch, 2020; Truong et al., 2020). The aggregation of a test statistic is a widely used method for dealing with the complexity associated with multidimensionality, e.g. Groen et al. (2013). Changes in multivariate time series can be either dense or sparse, depending whether they occur in the majority of the variates or in a subset, respectively. The type of change determines the best aggregation method, which is typically the maximum in the case of a sparse change or the average in the case of a dense change (Groen et al., 2013; Jirak, 2015). Currently, approaches aimed at finding the optimal aggregation method based on the type of change is an active research topic, e.g. Enikeeva and Harchaoui (2019) and Tickle et al. (2021).

1.4 Thesis objectives and outline

This thesis aims to deepen the understanding of forest disturbance dynamics at the landscape scale through the integration of optical satellite remote sensing and field data. In my PhD research project, I explored the potential of multispectral data acquired by Landsat and Sentinel-2 missions for tracking post-fire forest recovery, mapping burn severity and automating disturbance detection. The structure of the thesis is based on the following objectives:

(i) to evaluate the ability of Landsat-derived spectral indices to track post-fire forest recovery in the short- to medium-term;
(ii) to enhance effectiveness and operational usage of NBR-based bi-temporal indices for mapping burn severity;
(iii) to automate disturbance detection based on Landsat time series over a wide range of severities.

The thesis consists of five chapters: introduction (Chapter 1), research chapters (Chapters 2 to 4) and conclusions (Chapter 5). Research chapters are organised

as standalone research papers. Chapter 2 and 3 have been published, while Chapter 4 has been submitted for publication. Chapter 2 “Forest spectral recovery and regeneration dynamics in stand-replacing wildfires of central Apennines derived from Landsat time series” focuses on tracking post-fire forest recovery in four burnt areas in the central Apennines using Landsat-derived spectral vegetation indices. Chapter 3 “Mapping burn severity in the western Italian Alps through phenologically coherent reflectance composites derived from Sentinel-2 imagery” focuses on burn severity mapping in 10 burnt areas in the Western Italian Alps using NBR-based bi-temporal indices and a novel image compositing approach that embeds spatial patterns of land surface phenology. Chapter 4 “Change detection by multispectral trends: a Landsat time series-based algorithm for forest disturbance mapping and beyond” focuses on the development of an automated algorithm for mapping disturbances and their severity by analysing multivariate time series.

References

Allen, C.D., Breshears, D.D., McDowell, N.G., 2015. On underestimation of global vulnerability to tree mortality and forest die-off from hotter drought in the Anthropocene. Ecosphere 6, 1–55. https://doi.org/10.1890/ES15-00203.1

Allen, C.D., Macalady, A.K., Chenchouni, H., Bachelet, D., McDowell, N., Vennetier, M., Kitzberger, T., Rigling, A., Breshears, D.D., Hogg, E.H. (Ted., Gonzalez, P., Fensham, R., Zhang, Z., Castro, J., Demidova, N., Lim, J.H., Allard, G., Running, S.W., Semerci, A., Cobb, N., 2010. A global overview of drought and heat-induced tree mortality reveals emerging climate change risks for forests. For. Ecol. Manage. 259, 660–684. https://doi.org/10.1016/j.foreco.2009.09.001

Banskota, A., Kayastha, N., Falkowski, M.J., Wulder, M.A., Froese, R.E., White, J.C., 2014. Forest Monitoring Using Landsat Time Series Data: A Review. Can. J. Remote Sens. 40, 362–384.

https://doi.org/10.1080/07038992.2014.987376

Bartels, S.F., Chen, H.Y.H., Wulder, M.A., White, J.C., 2016. Trends in post-disturbance recovery rates of Canada's forests following wildfire and harvest. For. Ecol. Manage. 361, 194–207. https://doi.org/10.1016/j.foreco.2015.11.015

Bolton, D.K., Coops, N.C., Wulder, M.A., 2015. Characterizing residual structure and forest recovery following high-severity fire in the western boreal of Canada using Landsat time-series and airborne lidar data. Remote Sens. Environ. 163, 48–60. https://doi.org/10.1016/j.rse.2015.03.004

Cansler, C.A., McKenzie, D., 2012. How robust are burn severity indices when applied in a new region? Evaluation of alternate field-based and remote-sensing methods. Remote Sens. 4, 456–483. https://doi.org/10.3390/rs4020456

Cho, H., Kirch, C., 2020. Data segmentation algorithms: Univariate mean change and beyond. Econom. Stat. https://doi.org/10.1016/j.ecosta.2021.10.008

Cohen, W.B., Healey, S.P., Yang, Z., Stehman, S. V., Brewer, C.K., Brooks, E.B., Gorelick, N., Huang, C., Hughes, M.J., Kennedy, R.E., Loveland, T.R., Moisen, G.G., Schroeder, T.A., Vogelmann, J.E., Woodcock, C.E., Yang, L., Zhu, Z., 2017. How Similar Are Forest Disturbance Maps Derived from Different Landsat Time Series Algorithms? Forests 8, 1–19. https://doi.org/10.3390/f8040098

Cohen, W.B., Healey, S.P., Yang, Z., Zhu, Z., Gorelick, N., 2020. Diversity of algorithm and spectral band inputs improves landsat monitoring of forest disturbance. Remote Sens. 12, 1–15. https://doi.org/10.3390/rs12101673

Cohen, W.B., Yang, Z., Healey, S.P., Kennedy, R.E., Gorelick, N., 2018. A LandTrendr multispectral ensemble for forest disturbance detection. Remote Sens. Environ. 205, 131–140. https://doi.org/10.1016/j.rse.2017.11.015

Cohen, W.B., Yang, Z., Stehman, S. V., Schroeder, T.A., Bell, D.M., Masek, J.G., Huang, C., Meigs, G.W., 2016. Forest disturbance across the conterminous United States from 1985-2012: The emerging dominance of

forest decline. For. Ecol. Manage. 360, 242–252. https://doi.org/10.1016/j.foreco.2015.10.042

Coops, N.C., Shang, C., Wulder, M.A., White, J.C., Hermosilla, T., 2020. Change in forest condition: Characterizing non-stand replacing disturbances using time series satellite imagery. For. Ecol. Manage. 474, 118370. https://doi.org/10.1016/j.foreco.2020.118370

Doblas-Miranda, E., Alonso, R., Arnan, X., Bermejo, V., Brotons, L., de las Heras, J., Estiarte, M., Hódar, J.A., Llorens, P., Lloret, F., López-Serrano, F.R., Martínez-Vilalta, J., Moya, D., Peñuelas, J., Pino, J., Rodrigo, A., Roura-Pascual, N., Valladares, F., Vilà, M., Zamora, R., Retana, J., 2017. A review of the combination among global change factors in forests, shrublands and pastures of the Mediterranean Region: Beyond drought effects. Glob. Planet. Change 148, 42–54. https://doi.org/10.1016/j.gloplacha.2016.11.012

Donato, D.C., Campbell, J.L., Franklin, J.F., 2012. Multiple successional pathways and precocity in forest development: can some forests be born complex? J. Veg. Sci. 23, 576–584. https://doi.org/10.1111/j.1654-1103.2011.01362.x

Eidenshink, J., Schwind, B., Brewer, K., Zhu, Z., Quayle, B., Howard, S., 2007. A Project for Monitoring Trends in Burn Severity. Fire Ecol. 3, 3–21. https://doi.org/10.4996/fireecology.0301003

Enikeeva, F., Harchaoui, Z., 2019. High-dimensional change-point detection under sparse alternatives. Ann. Stat. 47, 2051–2079. https://doi.org/10.1214/18-AOS1740

Flood, N., 2013. Seasonal composite Landsat TM/ETM+ Images using the medoid (a multi-dimensional median). Remote Sens. 5, 6481–6500. https://doi.org/10.3390/rs5126481

Frantz, D., Röder, A., Stellmes, M., Hill, J., 2017. Phenology-adaptive pixel-based compositing using optical earth observation imagery. Remote Sens. Environ. 190, 331–347. https://doi.org/10.1016/j.rse.2017.01.002

Frolking, S., Palace, M.W., Clark, D.B., Chambers, J.Q., Shugart, H.H., Hurtt,

G.C., 2009. Forest disturbance and recovery: A general review in the context of spaceborne remote sensing of impacts on aboveground biomass and canopy structure. J. Geophys. Res. Biogeosciences 114. https://doi.org/10.1029/2008JG000911

García, M.J.L., Caselles, V., 1991. Mapping burns and natural reforestation using thematic Mapper data. Geocarto Int. 6, 31–37. https://doi.org/10.1080/10106049109354290

Groen, J.J.J., Kapetanios, G., Price, S., 2013. Multivariate methods for monitoring structural change. J. Appl. Econom. 28, 250–274. https://doi.org/10.1002/jae.1272

Healey, S.P., Cohen, W.B., Yang, Z., Kenneth Brewer, C., Brooks, E.B., Gorelick, N., Hernandez, A.J., Huang, C., Joseph Hughes, M., Kennedy, R.E., Loveland, T.R., Moisen, G.G., Schroeder, T.A., Stehman, S. V., Vogelmann, J.E., Woodcock, C.E., Yang, L., Zhu, Z., 2018. Mapping forest change using stacked generalization: An ensemble approach. Remote Sens. Environ. 204, 717–728. https://doi.org/10.1016/j.rse.2017.09.029

Hermosilla, T., Wulder, M.A., White, J.C., Coops, N.C., Hobart, G.W., 2015. An integrated Landsat time series protocol for change detection and generation of annual gap-free surface reflectance composites. Remote Sens. Environ. 158, 220–234. https://doi.org/10.1016/j.rse.2014.11.005

Jirak, M., 2015. Uniform change point tests in high dimension. Ann. Stat. 43, 2451–2483. https://doi.org/10.1214/15-AOS1347

Johnstone, J.F., Allen, C.D., Franklin, J.F., Frelich, L.E., Harvey, B.J., Higuera, P.E., Mack, M.C., Meentemeyer, R.K., Metz, M.R., Perry, G.L.W., Schoennagel, T., Turner, M.G., 2016. Changing disturbance regimes, ecological memory, and forest resilience. Front. Ecol. Environ. 14, 369–378. https://doi.org/10.1002/fee.1311

Keeley, J.E., 2009. Fire intensity, fire severity and burn severity: A brief review and suggested usage. Int. J. Wildl. Fire 18, 116–126. https://doi.org/10.1071/WF07049

Kennedy, R.E., Andréfouet, S., Cohen, W.B., Gomez, C., Griffiths, P., Hais, M.,

Healey, S.P., Helmer, E.H., Hostert, P., Lyons, M.B., Meigs, G.W., Pflugmacher, D., Phinn, S.R., Powell, S.L., Scarth, P., Sen, S., Schroeder, T.A., Schneider, A., Sonnenschein, R., Vogelmann, J.E., Wulder, M.A., Zhu, Z., 2014. Bringing an ecological view of change to landsat-based remote sensing. Front. Ecol. Environ. 12, 339–346. https://doi.org/10.1890/130066

Kennedy, R.E., Yang, Z., Cohen, W.B., 2010. Detecting trends in forest disturbance and recovery using yearly Landsat time series: 1. LandTrendr - Temporal segmentation algorithms. Remote Sens. Environ. 114, 2897–2910. https://doi.org/10.1016/j.rse.2010.07.008

Kennedy, R.E., Yang, Z., Cohen, W.B., Pfaff, E., Braaten, J., Nelson, P., 2012. Spatial and temporal patterns of forest disturbance and regrowth within the area of the Northwest Forest Plan. Remote Sens. Environ. 122, 117–133. https://doi.org/10.1016/j.rse.2011.09.024

Kennedy, R.E., Yang, Z., Gorelick, N., Braaten, J., Cavalcante, L., Cohen, W.B., Healey, S., 2018. Implementation of the LandTrendr algorithm on Google Earth Engine. Remote Sens. 10, 1–10. https://doi.org/10.3390/rs10050691

Key, C.H., 2006. Ecological and Sampling Constraints on Defining Landscape Fire Severity. Fire Ecol. 2, 34–59. https://doi.org/10.4996/fireecology.0202034

Key, C.H., Benson, N.C., 2006. Landscape assessment: Sampling and analysis methods, in: Lutes, D.C. (Ed.), FIREMON: Fire Effects Monitoring and Inventory System. U.S. Department of Agriculture, Forest Service, Rocky Mountain Research Station, Fort Collins, p. 55.

Kolden, C.A., Smith, A.M.S., Abatzoglou, J.T., 2015. Limitations and utilisation of Monitoring Trends in Burn Severity products for assessing wildfire severity in the USA. Int. J. Wildl. Fire 24, 1023–1028. https://doi.org/10.1071/WF15082

Kulakowski, D., Seidl, R., Holeksa, J., Kuuluvainen, T., Nagel, T.A., Panayotov, M., Svoboda, M., Thorn, S., Vacchiano, G., Whitlock, C., Wohlgemuth, T., Bebi, P., 2016. A walk on the wild side: Disturbance dynamics and the

conservation and management of European mountain forest ecosystems. For. Ecol. Manage. 388, 2–7. https://doi.org/10.1016/j.foreco.2016.07.037

Lentile, L.B., Holden, Z. a., Smith, A.M.S., Falkowski, M.J., Hudak, A.T., Morgan, P., Benson, N.C.N.C., Lewis, S.A., Gessler, P.E., Benson, N.C.N.C., 2006. Remote sensing techniques to assess active fire characteristics and post-fire effects. Int. J. Wildl. Fire 15, 319–345. https://doi.org/10.1071/WF05097

Leverkus, A.B., Rey Benayas, J.M., Castro, J., Boucher, D., Brewer, S., Collins, B.M., Donato, D., Fraver, S., Kishchuk, B.E., Lee, E.-J., Lindenmayer, D.B., Lingua, E., Macdonald, E., Marzano, R., Rhoades, C.C., Royo, A., Thorn, S., Wagenbrenner, J.W., Waldron, K., Wohlgemuth, T., Gustafsson, L., 2018. Salvage logging effects on regulating and supporting ecosystem services — a systematic map. Can. J. For. Res. 48, 983–1000. https://doi.org/10.1139/cjfr-2018-0114

Leverkus, A.B., Thorn, S., Gustafsson, L., Noss, R., Müller, J., Pausas, J.G., Lindenmayer, D.B., 2021. Environmental policies to cope with novel disturbance regimes–steps to address a world scientists' warning to humanity. Environ. Res. Lett. 16. https://doi.org/10.1088/1748-9326/abdc5a

Mantero, G., Morresi, D., Marzano, R., Motta, R., Mladenoff, D.J., Garbarino, M., 2020. The influence of land abandonment on forest disturbance regimes: a global review. Landsc. Ecol. 35, 2723–2744. https://doi.org/10.1007/s10980-020-01147-w

McDowell, N.G., Allen, C.D., Anderson-Teixeira, K., Aukema, B.H., Bond-Lamberty, B., Chini, L., Clark, J.S., Dietze, M., Grossiord, C., Hanbury-Brown, A., Hurtt, G.C., Jackson, R.B., Johnson, D.J., Kueppers, L., Lichstein, J.W., Ogle, K., Poulter, B., Pugh, T.A.M., Seidl, R., Turner, M.G., Uriarte, M., Walker, A.P., Xu, C., 2020. Pervasive shifts in forest dynamics in a changing world. Science (80-.). 368. https://doi.org/10.1126/science.aaz9463

Meddens, A.J.H., Kolden, C.A., Lutz, J.A., 2016. Detecting unburned areas

within wildfire perimeters using Landsat and ancillary data across the northwestern United States. Remote Sens. Environ. 186, 275–285. https://doi.org/10.1016/j.rse.2016.08.023

Miller, J.D., Knapp, E.E., Key, C.H., Skinner, C.N., Isbell, C.J., Creasy, R.M., Sherlock, J.W., 2009. Calibration and validation of the relative differenced Normalized Burn Ratio (RdNBR) to three measures of fire severity in the Sierra Nevada and Klamath Mountains, California, USA. Remote Sens. Environ. 113, 645–656. https://doi.org/10.1016/j.rse.2008.11.009

Miller, J.D., Thode, A.E., 2007. Quantifying burn severity in a heterogeneous landscape with a relative version of the delta Normalized Burn Ratio (dNBR). Remote Sens. Environ. 109, 66–80. https://doi.org/10.1016/j.rse.2006.12.006

Parks, S.A., Dillon, G.K., Miller, C., 2014. A new metric for quantifying burn severity: The relativized burn ratio. Remote Sens. 6, 1827–1844. https://doi.org/10.3390/rs6031827

Parks, S.A., Holsinger, L.M., Voss, M.A., Loehman, R.A., Robinson, N.P., 2018. Mean composite fire severity metrics computed with google earth engine offer improved accuracy and expanded mapping potential. Remote Sens. 10, 1–15. https://doi.org/10.3390/rs10060879

Pflugmacher, D., Cohen, W.B., Kennedy, R.E., 2012. Using Landsat-derived disturbance history (1972-2010) to predict current forest structure. Remote Sens. Environ. 122, 146–165. https://doi.org/10.1016/j.rse.2011.09.025

Pickell, P.D., Hermosilla, T., J. Frazier, R., Coops, N.C., Wulder, M.A., 2016. Forest recovery trends derived from Landsat time series for North American boreal forests. Int. J. Remote Sens. 37, 138–149. https://doi.org/10.1080/2150704X.2015.1126375

Picotte, J.J., Bhattarai, K., Howard, D., Lecker, J., Epting, J., Quayle, B., Benson, N., Nelson, K., 2020. Changes to the Monitoring Trends in Burn Severity program mapping production procedures and data products. Fire Ecol. 16. https://doi.org/10.1186/s42408-020-00076-y

Roberts, D., Mueller, N., McIntyre, A., 2017. High-Dimensional Pixel

Composites From Earth Observation Time Series. IEEE Trans. Geosci. Remote Sens. 55, 6254–6264. https://doi.org/10.1109/TGRS.2017.2723896

Röder, A., Hill, J., Duguy, B., Alloza, J.A., Vallejo, R., 2008. Using long time series of Landsat data to monitor fire events and post-fire dynamics and identify driving factors. A case study in the Ayora region (eastern Spain). Remote Sens. Environ. 112, 259–273. https://doi.org/10.1016/j.rse.2007.05.001

Rodman, K.C., Andrus, R.A., Veblen, T.T., Hart, S.J., 2021. Disturbance Detection in Landsat Time Series is Influenced By Tree Mortality Agent and Severity, Not By Prior Disturbance. Remote Sens. Environ. 254, 112244. https://doi.org/10.1016/j.rse.2020.112244

Rodman, K.C., Veblen, T.T., Battaglia, M.A., Chambers, M.E., Fornwalt, P.J., Holden, Z.A., Kolb, T.E., Ouzts, J.R., Rother, M.T., 2020. A changing climate is snuffing out post-fire recovery in montane forests. Glob. Ecol. Biogeogr. 29, 2039–2051. https://doi.org/10.1111/geb.13174

Rüetschi, M., Small, D., Waser, L.T., Rüetschi, M., Small, D., Waser, L.T., 2019. Rapid Detection of Windthrows Using Sentinel-1 C-Band SAR Data. Remote Sens. 2019, Vol. 11, Page 115 11, 115. https://doi.org/10.3390/RS11020115

Ruiz-Ramos, J., Marino, A., Boardman, C., Suarez, J., 2020. Continuous forest monitoring using cumulative sums of sentinel-1 timeseries. Remote Sens. 12. https://doi.org/10.3390/RS12183061

Sagar, S., Roberts, D., Bala, B., Lymburner, L., 2017. Extracting the intertidal extent and topography of the Australian coastline from a 28 year time series of Landsat observations. Remote Sens. Environ. 195, 153–169. https://doi.org/10.1016/j.rse.2017.04.009

Schroeder, T.A., Cohen, W.B., Yang, Z., 2007. Patterns of forest regrowth following clearcutting in western Oregon as determined from a Landsat time-series. For. Ecol. Manage. 243, 259–273. https://doi.org/10.1016/j.foreco.2007.03.019

Seidl, R., 2014. The shape of ecosystem management to come: Anticipating risks

and fostering resilience. Bioscience 64, 1159–1169. https://doi.org/10.1093/biosci/biu172

Seidl, R., Spies, T.A., Peterson, D.L., Stephens, S.L., Hicke, J.A., 2016. Searching for resilience: Addressing the impacts of changing disturbance regimes on forest ecosystem services. J. Appl. Ecol. 53, 120–129. https://doi.org/10.1111/1365-2664.12511

Seidl, R., Thom, D., Kautz, M., Martin-Benito, D., Peltoniemi, M., Vacchiano, G., Wild, J., Ascoli, D., Petr, M., Honkaniemi, J., Lexer, M.J., Trotsiuk, V., Mairota, P., Svoboda, M., Fabrika, M., Nagel, T.A., Reyer, C.P.O., 2017. Forest disturbances under climate change. Nat. Clim. Chang. 7, 395–402. https://doi.org/10.1038/nclimate3303

Senf, C., Müller, J., Seidl, R., 2019. Post-disturbance recovery of forest cover and tree height differ with management in Central Europe. Landsc. Ecol. 34, 2837–2850. https://doi.org/10.1007/s10980-019-00921-9

Soverel, N.O., Coops, N.C., Perrakis, D.D.B., Daniels, L.D., Gergel, S.E., 2011. The transferability of a dNBR-derived model to predict burn severity across 10 wildland fires in western Canada. Int. J. Wildl. Fire 20, 518–531. https://doi.org/10.1071/WF10081

Stevens-Rumann, C.S., Kemp, K.B., Higuera, P.E., Harvey, B.J., Rother, M.T., Donato, D.C., Morgan, P., Veblen, T.T., 2018. Evidence for declining forest resilience to wildfires under climate change. Ecol. Lett. 21, 243–252. https://doi.org/10.1111/ele.12889

Swanson, M.E., Franklin, J.F., Beschta, R.L., Crisafulli, C.M., Dellasala, D.A., Hutto, R.L., Lindenmayer, D.B., Swanson, F.J., 2011. The forgotten stage of forest succession: early-successional ecosystems on forest sites. Front. Ecol. Environ. 9, 117–125. https://doi.org/10.1890/090157

Tanase, M., de la Riva, J., Pérez-Cabello, F., 2011. Estimating burn severity at the regional level using optically based indices. Can. J. For. Res. 41, 863–872. https://doi.org/10.1139/x11-011

Tickle, S.O., Eckley, I.A., Fearnhead, P., 2021. A computationally efficient, high-dimensional multiple changepoint procedure with application to global

terrorism incidence. J. R. Stat. Soc. Ser. A Stat. Soc. 184, 1303–1325. https://doi.org/10.1111/rssa.12695

Truong, C., Oudre, L., Vayatis, N., 2020. Selective review of offline change point detection methods. Signal Processing 167, 107299. https://doi.org/10.1016/j.sigpro.2019.107299

Turner, M.G., 2010. Disturbance and landscape dynamics in a changing world. Ecology 91, 2833–2849. https://doi.org/10.1890/10-0097.1

Veraverbeke, S., Gitas, I., Katagis, T., Polychronaki, A., Somers, B., Goossens, R., 2012. Assessing post-fire vegetation recovery using red-near infrared vegetation indices: Accounting for background and vegetation variability. ISPRS J. Photogramm. Remote Sens. 68, 28–39. https://doi.org/10.1016/j.isprsjprs.2011.12.007

Veraverbeke, S., Lhermitte, S., Verstraeten, W.W., Goossens, R., 2010a. The temporal dimension of differenced Normalized Burn Ratio (dNBR) fire/burn severity studies: The case of the large 2007 Peloponnese wildfires in Greece. Remote Sens. Environ. 114, 2548–2563. https://doi.org/10.1016/j.rse.2010.05.029

Veraverbeke, S., Verstraeten, W.W., Lhermitte, S., Goossens, R., 2010b. Illumination effects on the differenced Normalized Burn Ratio's optimality for assessing fire severity 12, 60–70. https://doi.org/10.1016/j.jag.2009.10.004

Viedma, O., Meliá, J., Segarra, D., García-Haro, J., 1997. Modeling rates of ecosystem recovery after fires by using landsat TM data. Remote Sens. Environ. 61, 383–398. https://doi.org/10.1016/S0034-4257(97)00048-5

Vogeler, J.C., Yang, Z., Cohen, W.B., 2016. Mapping post-fire habitat characteristics through the fusion of remote sensing tools. Remote Sens. Environ. 173, 294–303. https://doi.org/10.1016/j.rse.2015.08.011

White, J.C., Wulder, M.A., Hermosilla, T., Coops, N.C., Hobart, G.W., 2017. A nationwide annual characterization of 25 years of forest disturbance and recovery for Canada using Landsat time series. Remote Sens. Environ. 194, 303–321. https://doi.org/10.1016/j.rse.2017.03.035

White, J.C., Wulder, M.A., Hobart, G.W., Luther, J.E., Hermosilla, T., Griffiths, P., Coops, N.C., Hall, R.J., Hostert, P., Dyk, A., Guindon, L., 2014. Pixel-based image compositing for large-area dense time series applications and science. Can. J. Remote Sens. 40, 192–212. https://doi.org/10.1080/07038992.2014.945827

Whitman, E., Parisien, M.A., Holsinger, L.M., Park, J., Parks, S.A., 2020. A method for creating a burn severity atlas: An example from Alberta, Canada. Int. J. Wildl. Fire 29, 995–1008. https://doi.org/10.1071/WF19177

Wulder, M.A., Loveland, T.R., Roy, D.P., Crawford, C.J., Masek, J.G., Woodcock, C.E., Allen, R.G., Anderson, M.C., Belward, A.S., Cohen, W.B., Dwyer, J., Erb, A., Gao, F., Griffiths, P., Helder, D., Hermosilla, T., Hipple, J.D., Hostert, P., Hughes, M.J., Huntington, J., Johnson, D.M., Kennedy, R., Kilic, A., Li, Z., Lymburner, L., McCorkel, J., Pahlevan, N., Scambos, T.A., Schaaf, C., Schott, J.R., Sheng, Y., Storey, J., Vermote, E., Vogelmann, J., White, J.C., Wynne, R.H., Zhu, Z., 2019. Current status of Landsat program, science, and applications. Remote Sens. Environ. 225, 127–147. https://doi.org/10.1016/j.rse.2019.02.015

Wulder, M.A., Masek, J.G., Cohen, W.B., Loveland, T.R., Woodcock, C.E., 2012. Opening the archive: How free data has enabled the science and monitoring promise of Landsat. Remote Sens. Environ. 122, 2–10. https://doi.org/10.1016/j.rse.2012.01.010

Ygorra, B., Frappart, F., Wigneron, J.P., Moisy, C., Catry, T., Baup, F., Hamunyela, E., Riazanoff, S., 2021. Monitoring loss of tropical forest cover from Sentinel-1 time-series: A CuSum-based approach. Int. J. Appl. Earth Obs. Geoinf. 103, 102532. https://doi.org/10.1016/j.jag.2021.102532

Zhao, F.A.R., Meng, R., Huang, C., Zhao, M., Zhao, F.A.R., Gong, P., Yu, L., Zhu, Z., 2016. Long-term post-disturbance forest recovery in the greater yellowstone ecosystem analyzed using Landsat time series stack. Remote Sens. 8, 2–3. https://doi.org/10.3390/rs8110898

Zhu, Z., 2017. Change detection using landsat time series: A review of frequencies, preprocessing, algorithms, and applications. ISPRS J.

Photogramm. Remote Sens. 130, 370–384. https://doi.org/10.1016/j.isprsjprs.2017.06.013

Zhu, Z., Zhang, J., Yang, Z., Aljaddani, A.H., Cohen, W.B., Qiu, S., Zhou, C., 2019. Continuous monitoring of land disturbance based on Landsat time series. Remote Sens. Environ. 238, 111116. https://doi.org/10.1016/j.rse.2019.03.009

Chapter 2

Forest spectral recovery and regeneration dynamics in stand-replacing wildfires of central Apennines derived from Landsat time series

Donato Morresi, Alessandro Vitali, Carlo Urbinati and Matteo Garbarino

This chapter has been published open access in the Remote Sensing journal: Morresi, D., Vitali, A., Urbinati, C., Garbarino, M., 2019. Forest Spectral Recovery and Regeneration Dynamics in Stand-Replacing Wildfires of Central Apennines Derived from Landsat Time Series. Remote Sens. 11, 308. https://doi.org/10.3390/rs11030308

Abstract

Understanding post-fire regeneration dynamics is an important task for assessing the resilience of forests and to adequately guide post-disturbance management. The main goal of this research was to compare the ability of different Landsat-derived spectral vegetation indices (SVIs) to track post-fire recovery occurring in burned forests of the central Apennines (Italy) at different development stages. Normalized Difference Vegetation Index (NDVI), Normalized Difference Moisture Index (NDMI), Normalized Burn Ratio (NBR), Normalized Burn Ratio 2 (NBR2) and a novel index called Forest Recovery Index 2 (FRI2) were used to compute post-fire recovery metrics throughout 11 years (2008–2018). FRI2 achieved the highest significant correlation (Pearson's $r = 0.72$) with tree canopy cover estimated by field sampling (year 2017). The Theil–Sen slope estimator of linear regression was employed to assess the rate of change and the direction of SVIs recovery metrics over time (2010–2018) and the Mann–Kendall test was used to evaluate the significance of the spectral trends. NDVI displayed the highest amount of recovered pixels (38%) after 11 years since fire occurrence, whereas the mean value of NDMI, NBR, NBR2, and FRI2 was about 27%. NDVI

was more suitable for tracking early stages of the secondary succession, suggesting greater sensitivity toward non-arboreal vegetation development. Predicted spectral recovery timespans based on pixels with a statistically significant monotonic trend did not highlight noticeable differences among normalized SVIs, suggesting similar suitability for monitoring early to mid-stages of post-fire forest succession. FRI2 achieved reliable results in mid- to long-term forest recovery as it produced up to 50% longer periods of spectral recovery compared to normalized SVIs. Further research is needed to understand this modeling approach at advanced stages of post-fire forest recovery.

2.1 Introduction

The interaction between climate and land-use changes is raising the frequency, surface area, and severity of wildfires in the Mediterranean Basin (Hernandez et al., 2015; Pausas and Fernández-Muñoz, 2012; San-Miguel-Ayanz et al., 2017, 2013). Among climate change effects, long periods of dry weather are expected to increase fire danger in southern European mountains both under short- and long-term climatic scenarios (de Rigo et al., 2017). The development of appropriate management strategies is essential to prevent fire occurrence and to enhance forest recovery (Moreira et al., 2012; Spasojevic et al., 2016). The latter is a critical ecological process after a stand-replacing disturbance, referring to the re-establishment or re-development of forest biomass and canopy structure (Bartels et al., 2016; Frolking et al., 2009; Scheller and Swanson, 2015). This process affects regional and global carbon cycles (Goetz et al., 2012; Pan et al., 2011) and promotes numerous ecosystem services (Frolking et al., 2009). Furthermore, forest degradation in the xeric Mediterranean mountains induced by a fire frequency increase can occur even in stands dominated by fire-adapted tree taxa (Moreira et al., 2012). Forest recovery at a landscape scale is often modeled as a fast and homogeneous process. However, depending on the fire severity level, it might be a very diversified one (Scheller and Swanson, 2015), with great changes in forest structure and species composition (Keeley, 2009).

Since past decades, satellite optical remote sensing was widely adopted for the analysis of post-fire forest recovery (Gitas et al., 2012). Imagery collected by the United States (US) Landsat program is currently considered as the most valuable source of time-series data at a landscape scale (Frolking et al., 2009; Vogelmann et al., 2016). This is primarily due to the long-term availability of systematically acquired images, spanning over 40 years. The unique combination of 30-m spatial resolution and 16 days of revisiting time enables assembling conspicuous Landsat time series (LTS) (Banskota et al., 2014). Monitoring forest regeneration development through gradual changes in the optical spectral domain is challenging, given the confounding effects from a variety of factors such as phenology and sun angles (Song and Woodcock, 2003; Vogelmann et al., 2016). To reduce these types of noise, selecting near-anniversary acquisition dates (Song and Woodcock, 2003) or using unburned neighboring pixels as control areas (Diaz-Delgado et al., 2001; Lhermitte et al., 2010) were proposed. However, limitations such as data gaps in the time series (Vogelmann et al., 2016) can negatively affect outcomes. Recent development in dense Landsat time-series collection by including all the clear yearly observations (Zhu et al., 2012) proved to be useful in characterizing both intra-annual variations and long-term temporal trajectories (Vogelmann et al., 2016).

Spectral vegetation indices (SVIs) (Diaz-Delgado et al., 1998; Pickell et al., 2016; Schroeder et al., 2011; Viedma et al., 1997) and spectral mixture analysis (SMA) (Röder et al., 2008; Solans Vila and Barbosa, 2010; Veraverbeke et al., 2012) are common remote-sensing techniques to track post-fire vegetation recovery using LTS, and were adopted in different vegetation communities and ecosystems (Chu and Guo, 2013; Gitas et al., 2012). SVIs from LTS are widely used since they can maximize the sensitivity to plant biophysical factors and reduce the noise from atmosphere, landforms, and soil variability (Jensen, 2014; Song et al., 2015). Specifically, Normalized Difference Vegetation Index (NDVI) was widely employed to assess post-fire vegetation recovery using a multi-temporal approach in several burned sites of the Mediterranean Basin, primarily because of the high correlation achieved with field measurements such as fractional vegetation cover

(Clemente et al., 2009; Solans Vila and Barbosa, 2010). Other studies in North American boreal forests focused on indices contrasting the near-infrared (NIR) and shortwave-infrared (SWIR) bands of Landsat TM/ETM+/OLI sensors to track post-fire recovery (Cohen et al., 2010; Pickell et al., 2016; Schroeder et al., 2011). Since the shortwave-infrared region of the spectral domain is sensitive to variations in the forest structure (Cohen and Goward, 2004; Cuevas-González et al., 2009; Song and Woodcock, 2003), Normalized Difference Moisture Index (NDMI) (Hardisky et al., 1983) and Normalized Burn Ratio (NBR) (Key et al., 1999) or the SWIR1 band alone (Kennedy et al., 2007; Pickell et al., 2016) are of great interest to monitor post-disturbance forest recovery. Additionally, Normalized Burn Ratio 2 (NBR2) takes advantage of the contrast between the two Landsat sensor SWIR bands, with promising results in the assessment of post-fire vegetation recovery in the shrublands of California (Storey et al., 2016) and sclerophyll forests of Australia (Hislop et al., 2018).

The Integrated Forest *z*-score (IFZ) is a threshold-based index that was initially developed as a part of the Vegetation Change Tracker algorithm (Huang et al., 2010) in order to target abrupt forest cover changes at the pixel level. Specifically, IFZ is an inverse measure of the likelihood of a pixel to be forested, which is obtained by computing its spectral distance from defined forest pixels. Some authors proposed using the reciprocal of IFZ, termed Forest Recovery Index (FRI), to allow for the comparison with other spectral indices growing in direct proportion with the amount of vegetation cover such as NDVI (Chu et al., 2016). To date, few studies employed either IFZ or FRI in post-fire forest recovery tracking (Chen et al., 2011; Chu et al., 2016; Zhao et al., 2016), but its potential toward the detection of long-term forest recovery dynamics was highlighted within ponderosa pine forests (Chen et al., 2011), boreal larch forests (Chu et al., 2016), and a mosaic of mixed conifer forests in the Greater Yellowstone Ecosystem (Zhao et al., 2016).

Post-fire recovery rates were assessed through trend analysis on LTS which involved fitting linear, non-linear (Röder et al., 2008), and segmented (Kennedy et al., 2010) pixel-wise models to near-anniversary date images to characterize

the spatial variability of this gradual process. This approach proved to be effective, but trend analysis based on single curve fitting can be biased by outliers (Banskota et al., 2014), making the adoption of robust regression models preferable. Another challenging factor to be considered is the land-cover heterogeneity due to the anthropogenic disturbances. This is particularly evident in human-shaped landscapes featuring a complex patch mosaic of crops, forests, pastures, and human infrastructures.

The present study aimed to compare the efficiency of different spectral vegetation indices to assess the early forest recolonization patterns in four burned landscape mosaics of the central Apennines (Italy). Wildfires in this mountain ecoregion are one of the most common natural disturbances (Vacchiano et al., 2016; van Gils et al., 2010), but forest recovery dynamics is scarcely studied with a remote-sensing approach. Our general hypotheses to be tested were as follows: (a) Landsat-derived spectral vegetation indices employing the SWIR bands have enhanced sensitivity toward post-fire forest recovery dynamics; (b) forest regeneration processes under different burn severity degrees and forest types can be inferred from recovery patterns of spectral vegetation indices; (c) the ability of Landsat-derived spectral vegetation indices to track diachronic post-fire forest recovery dynamics can be assessed through spatially explicit robust regression models.

2.2 Materials and methods

2.2.1 Study areas

The study was held in the central Apennines and it included areas of the Marche and Abruzzo administrative regions. Four large stand-replacing wildfires were located using MODIS Collection 6 Level 3 monthly burned area products (MCD64A1) (Giglio et al., 2018). The correspondent study areas were named with the nearest municipality: Roccafluvione (RF), L'Aquila (LA), Navelli (NA), and Roccamorice (RM) (Figure 2.1). This dataset also provided the starting date of each wildfire and the overall burned surface area (Table 2.1). The extent of

forest areas affected by wildfires was initially estimated by intersecting the Corine Land Cover 2006 (CLC) forest cover map (codes 311, 312, 313) with the MODIS burned area products in a GIS environment (Table 2.1).

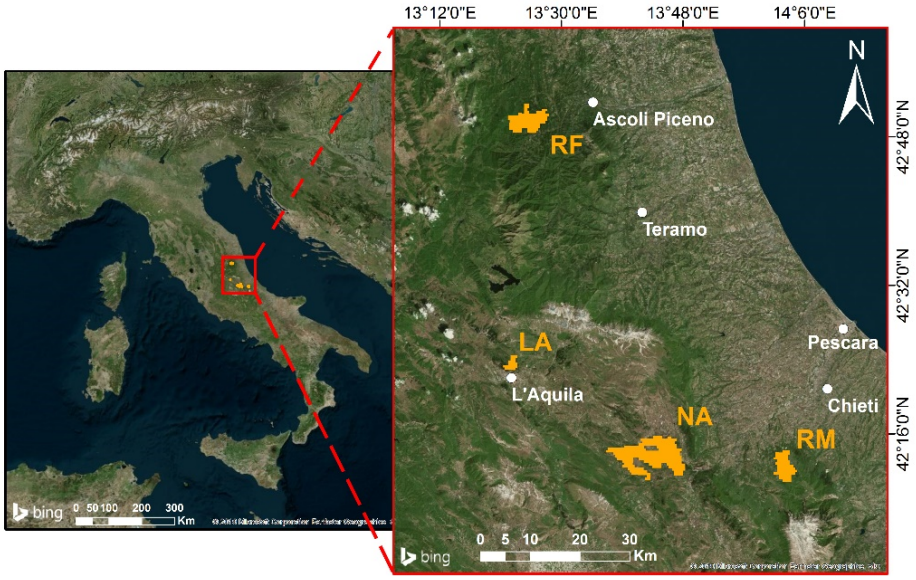

Figure 2.1. Location and wildfire surface (orange polygons) from MODIS burned area (MCD64A1) of the four study areas: Roccafluvione (RF), L'Aquila (LA), Navelli (NA), and Roccamorice (RM).

The large wildfires which occurred in central and southern Italy during the summer of 2007 were driven by severe climate conditions, similar to those arising in Greece during the same year (Camia and Amatulli, 2009; Joint Research Centre, 2008). The occurrence of previous prolonged drought periods, the high summer temperatures, and strong winds enhanced the spread of large wildfires (Joint Research Centre, 2008). Other environmental and social factors contributed to raising the fire risk in the study areas, such as the abandonment of agricultural lands and the lack of regular fire prevention forest management (Joint Research Centre, 2008). Moreover, the suppression of these wildfires was made difficult due to their almost synchronic occurrence (same days of July and

August) (Joint Research Centre, 2008). The impacted stands were mainly conifer plantations pure or mixed with indigenous broadleaved woodlands classified into three different forest types of the regional forest inventories. Hardwood stands were dominated by pubescent oak (*Quercus pubescens*) (Po) or by mixed manna ash (*Fraxinus ornus*) and European hop-hornbeam (*Ostrya carpinifolia*) (Ma). European black pine (*Pinus nigra*) (Pp) dominated conifer plantations.

Table 2.1. Wildfire information, and climate and landform properties of the four study areas: Roccafluvione (RF), L'Aquila (LA), Navelli (NA), and Roccamorice (RM).

	RF	**LA**	**NA**	**RM**
Fire start date	21 July 2007	9 August 2007	14 July 2007	23 July 2007
Overall burned area (hectares)	2753	530	6939	1823
Forest burned area (hectares)	1860	391	1896	427
Annual mean temperature (°C)	12.4	11	11.8	10.9
Annual mean precipitation (mm)	820.9	856.7	827.1	743.9
Mean altitude (m) ± SD	628 ± 146	977 ± 104	787 ± 206	933 ± 206
Mean slope (°) ± SD	28 ± 9	21 ± 8	17 ± 9	17 ± 9
Mean roughness index	23	12	9	10
Heat Load Index ± SD	0.76 ± 0.09	0.79 ± 0.05	0.74 ±0.06	0.76 ± 0.07

Climate and landform similarities between the study areas (Table 2.1) were highlighted to support the comparison of post-fire recovery dynamics between these sites. Climatic data were extracted from WorldClim Version 2 grids with a spatial resolution of ~1 km^2 (Fick and Hijmans, 2017), whereas

geomorphological features were derived from the 10-m resolution TINITALY DEM (Tarquini and Nannipieri, 2017).

2.2.2 Dataset and preprocessing

Forest regeneration dynamics were explored using a series of Landsat annual image composites at one-year intervals between 2001 and 2018, resulting in a total period of 18 years (seven pre-fire and 11 post-fire) for each study area. Annual composites were produced with priority to images acquired closest to the day of peak (DOP) of the same growing season and with the highest percentage of valid pixels (i.e., not contaminated by clouds/cloud shadows or with missing values). The selected DOP corresponds to 12 July in non-leap years (day-of-year 197) and was derived from the EVI2 Long-Term Average Phenology (from 1980 to 2010) available at the Vegetation Index and Phenology Lab Data Explorer (Vegetation Index and Phenology Lab, 2011), which contains historical annual phenology parameters obtained from AVHRR and MODIS sensors for homogeneous vegetation clusters (Didan, 2010). The least cloud-contaminated acquisitions available for the study areas in the growing season (1 June–31 August) were selected to produce annual composites. The dataset includes Landsat TM, ETM+, and OLI images acquired in the WRS-2 Path/Row 190/30, 190/31, and 191/30 (details are provided in Table S2.1). The majority of Landsat data was provided by the USGS Earth Resources Observation and Science (EROS) Center Science Processing Architecture (ESPA) On-Demand Interface ("USGS Earth Resources Observation and Science (EROS) Center Science Processing Architecture (ESPA) On Demand Interface," 2018) processed in surface reflectance (Level-2 Science Products). Surface reflectance products of Landsat 5 TM and Landsat 7 ETM+ were generated using the Landsat Ecosystem Disturbance Adaptive Processing System (LEDAPS) (Masek et al., 2006). Instead, Landsat 8 OLI processing was based on the Landsat Surface Reflectance Code (LaSRC) (Vermote et al., 2016). Two Landsat 5 TM scenes acquired in 2008 (WRS-2 Path/Row 190/31) were available only in the ESA Landsat archive

("ESA Online Dissemination," 2018) at Level-1T (radiometrically calibrated and orthorectified using ground control points and DEM). They were co-registered with USGS scenes using the tool AROSICS (Scheffler et al., 2017) and further converted to surface reflectance using the 6S radiative transfer model (Vermote et al., 1997) employed by LEDAPS and implemented in GRASS GIS 7.2 (GRASS Development Team, 2017; Neteler et al., 2012). Clouds and cloud shadows were masked with the function of mask method (Zhu et al., 2015; Zhu and Woodcock, 2012). As Landsat 8 OLI images were about one-third of all images used in this study, they were calibrated to those acquired by Landsat 7 ETM+ through gain and offset coefficients (Roy et al., 2016).

2.2.3 Fire perimeter and burn severity assessment

Fire perimeter and the spatial distribution of burn severity patterns within each study area were assessed using the Relative difference Normalized Burn Ratio (RdNBR) (Miller and Thode, 2007). Single Landsat TM summer images of 2006 and 2008 were employed to compute RdNBR as described by Equations (1), (2), and (3). Table S2.2 (Supplementary Materials) provides detailed information on these images.

$$NBR = \frac{(NIR - SWIR2)}{(NIR + SWIR2)} \quad (1)$$

$$dNBR = \left(\left(NBR_{prefire} - NBR_{postfire}\right) * 1000\right) - dNBR_{offset} \quad (2)$$

$$RdNBR = \frac{dNBR}{\sqrt{\left|NBR_{prefire}\right|}} \quad (3)$$

The evaluation of spectral changes caused by the fire on forest ecosystems during the following vegetative season is defined as an extended assessment of remotely sensed burn severity and included first- and second-order effects caused by fire (Key, 2006; Key and Benson, 2006; Veraverbeke et al., 2010). Because burn severity assessment was not performed through field surveys, the thresholds

defined by Miller and Thode (Miller and Thode, 2007) were used to define burn severity classes (low, moderate, and high) of the RdNBR. The dNBR offset was computed by averaging dNBR values within undisturbed forest pixels which were delineated for each study area (Section 2.2.5) to minimize changes in reflectance not caused by fire (Key, 2006; Miller and Thode, 2007; Parks et al., 2014). Fire perimeters of each study area were corrected through on-screen digitization of burned pixels in post-fire Landsat TM images (2008) using false-color composites (RGB = SWIR2, NIR, Red), as misclassification between unchanged and low-severity pixels occurred frequently.

2.2.4 Area of interest within fire perimeters

Regeneration dynamics were investigated in those groups of burned pixels containing at least 10% of tree canopy fractional cover before fires and that were larger than 0.5 ha. These parameters were drawn from the definition of forest provided by the Food and Agriculture Organization (FAO) of the United Nations (FAO, 1998). Pre-fire tree canopy fractional cover within each fire perimeter was computed using pre-fire forest/non-forest land-cover maps obtained from the classification of high-resolution (0.5 m) RGB aerial orthophotos provided by the Italian Agency for payments in agriculture (AGEA) (Table 2.2) through an object-oriented classification approach using Trimble eCognition Developer software. Firstly, a multi-resolution bottom-up segmentation (Baatz and Schäpe, 2000; Benz et al., 2004) was applied in order to aggregate groups of tree canopies by repeatedly increasing the scale factor toward the stand scale. Secondly, the support vector machine (SVM) classifier (Huang et al., 2002; Tzotsos and Argialas, 2008) was applied to the coarser-scale objects using the radial basis function (RBF) kernel with tuning parameters “cost” (C) and gamma proposed by Qian et al. (Qian et al., 2015). On-screen validation of 200 randomly distributed points per forest/non-forest class (400 points for each study area) was performed using orthophotos as ground truth reference (Table 2.2).

Table 2.2. Italian Agency for payments in agriculture (AGEA) orthophoto acquisition dates, accuracy assessment metrics of forest/non-forest cover maps, and percentage of forest cover within fire perimeters. Accuracy metrics: producer's accuracy (PA), user's accuracy (UA), overall accuracy, and K statistic values for each study area (Roccafluvione—RF, L'Aquila—LA, Navelli—NA, Roccamorice—RM).

	RF	**LA**	**NA**	**RM**
Acquisition dates	18 June 2007	14 May 2007 9 September 2007	14 May2007 18 June 2007	21 June 2007 9 July 2007
PA forest cover (%)	95.68	99.45	97.08	94.44
PA non-forest cover (%)	89.3	91.71	93.46	93.56
UA forest cover (%)	88.5	91	93.2	93.5
UA non-forest cover (%)	96	99.5	97.2	94.5
Overall accuracy (%)	92.25	95.25%	95.2%	94%
Kappa coefficient	0.845	0.905	0.904	0.88
Classified forest cover (%)	85.75	73.38	39.11	32.68

2.2.5 Spectral vegetation indices

Post-fire temporal trajectories of burned forests were assessed using five spectral vegetation indices (SVI): NDVI (Normalized Difference Vegetation Index) (Tucker, 1979), NDMI (Normalized Difference Moisture Index) (Hardisky et al., 1983), NBR (Normalized Burn Ratio) (Key et al., 1999), NBR2 (Normalized Burn Ratio 2) (Hislop et al., 2018; Storey et al., 2016; Stroppiana et al., 2012), and FRI2 (Forest Recovery Index 2), which is a revised version of FRI (Forest Recovery Index) (Chu et al., 2016). They were used with Landsat imagery both

for the detection of forest disturbances including fires and to monitor post-disturbance forest dynamics. NDVI and NDMI, and NBR and NBR2 were computed as shown in Equations (4) and (5), and Equation (1) and (6), respectively.

$$NDVI = \frac{(NIR - Red)}{(NIR + Red)} \tag{4}$$

$$NDMI = \frac{(NIR - SWIR1)}{(NIR + SWIR1)} \tag{5}$$

$$NBR2 = \frac{(SWIR1 - SWIR2)}{(SWIR1 + SWIR2)} \tag{6}$$

Like FRI, FRI2 (Equation (7)) is the reciprocal of IFZ (Huang et al., 2008) (Equation (8)). Adding 1 to IFZ at the denominator avoided obtaining wild values when IFZ was close to 0 and constrained FRI2 to the range between 0 and 1.

$$FRI2 = \frac{1}{(IFZ + 1)} \tag{7}$$

$$IFZ = \sqrt{\frac{1}{NB} \sum_{i=1}^{N} \left(\frac{b_i - \bar{b}_i}{SD_i} \right)^2} \tag{8}$$

In Equation (8), b_i is the spectral value of the pixel in band *i*, $\bar{b}_i$ and SD_i are the mean and standard deviation obtained from forest samples in band *i*, and NB is the number of spectral bands. The Red, SWIR1, and SWIR2 Landsat bands were employed due to their sensitivity to forest cover changes (Huang et al., 2010). Yearly means and standard deviations of forest cover were extracted from a forest mask with boundaries outlined by increasing fire perimeter extents of 4 km (Euclidean distance). Specifically, this mask was built selecting those Landsat pixels with a tree canopy fractional cover higher than 90% exhibiting a stable behavior over time. Because pre-fire tree canopy fractional cover was available only within the fire perimeters (Section 2.2.4), it was estimated outside them using a Random Forest model at the Landsat pixel scale. Pre-fire tree canopy cover maps within the fire perimeters were employed to train the model and the

Landsat data (six spectral bands acquired during pre-fire dates in 2007 and its derived SVIs) were used as predictor variables. At last, stable forest pixels were outlined by selecting those with an NBR maximum range lower than 0.15 for the entire analysis interval (2001–2018).

2.2.6 Field data and SVI correlation

Tree canopy fractional cover including both dominant and overtopped trees was visually assessed in the field (study area RF) during the summer of 2017 (June and July) using 38 circular plots with 30-m diameter. Centroids of the plots were located close to the center of each Landsat image pixel using a Trimble Juno 3B handheld GPS and a Trimble Pro 6T GNSS receiver having sub-metric horizontal accuracy. SVIs values were extracted using a bilinear interpolation method to limit mismatches between Landsat pixels centroids location and field plots as suggested by Parks et al. (Parks et al., 2014). Tree canopy fractional cover was correlated with the SVIs obtained from the image composite of 2017 using Pearson's correlation test.

2.2.7 Post-fire recovery metrics and temporal trajectories

A Relative Difference SVI (RDSVI) index was computed for each post-fire SVI as shown in Equation (9), using an algorithm similar to the ones proposed for the burn severity detection (Miller and Thode, 2007; Parks et al., 2014). Forest spectral recovery causes a decrease in RDSVI values through time since the difference between pre-fire and post-fire decreases as well. The relativization of SVIs allowed for the comparison between recovery dynamics occurring under different ecological conditions such as pre-fire canopy cover density and different forest types. The median pixel value from 2001 to 2007 for each SVI was taken as reference for the pre-fire condition. The averaged difference between pre-fire median and annual post-fire SVIs was extracted from undisturbed forest cover (Section 2.2.4) to account for inter-annual changes of SVIs. These changes can be attributed to external factors such as phenology and sun angle, similarly to the

offset employed for burn severity assessment (Section 2.2.3). This offset was applied to normalized SVIs (NDVI, NDMI, NBR, and NBR2) as FRI2 is already obtained using yearly spectral values of undisturbed forest cover.

$$RDSVI = \frac{\left(\left(SVI_{prefire\ median} - SVI_{nth\ postfire\ year}\right) - SVI_{offset}\right)}{SVI_{prefire\ median}} \quad (9)$$

Post-fire forest spectral trajectories were assessed by averaging RDSVI values extracted from a set of sampling points located in different burn severity classes and forest types within the area of interest. These points were randomly distributed at a minimum distance of 200 meters in order to reduce the influence of spatial autocorrelation. Global Moran's I test was performed using incremental distances to determine this lowest one. The number of sampling points varied among study areas from 491 to 77, according to the extent of each wildfire.

2.2.8 Statistical analysis of recovery trends

The non-parametric Theil–Sen (TS) slope estimator of linear regression (Sen, 1968; Theil, 1992) was employed to assess pixel-wise changes of RDSVI occurring within the area of interest from 2010 to 2018. The time frame for the analyses started on the third year since fire occurrence. The early post-fire succession in Mediterranean ecosystems usually features a prompt colonization of annual herbs and perennial woody shrubs (Capitanio and Carcaillet, 2008). This could yield large increases of SVIs (Diaz-Delgado et al., 2001; Röder et al., 2008; Viedma et al., 1997), biasing the trend of forest spectral recovery. The TS slope estimator was chosen as it is insensitive to up to 29% of outliers (Neeti and Eastman, 2011; Nitze and Grosse, 2016) and it proved to be effective in detecting SVI trends of forest ecosystems (Czerwinski et al., 2014; Nitze and Grosse, 2016; Olthof et al., 2014). This method involves computing the median of all the slopes between observation values at all pairwise time steps for a total of n(n − 1)/2 slopes. Equation (10) displays how it is computed for observations Y_j and Y_i taken at time t_j and t_i.

$$TS\ slope = median\left(\frac{Y_j - Y_i}{t_j - t_i}\right);\ i < j, t_i \neq t_j \quad (10)$$

The intercept of the linear trend was computed with the Conover equation (11) (Conover, 1980),

$$intercept = median(Y) - TS\ slope \times median(t) \quad (11)$$

where median(Y) and median(t) are the medians of observations (Y) and of the time-series length (t). The significance of the TS slope is commonly tested using the rank-based Mann–Kendall (MK) test (Kendall, 1975; Mann, 1945; Neeti and Eastman, 2011; Yue et al., 2002) through which the existence of a monotonic trend is evaluated, without any assumption regarding its shape. The direction and the power of a monotonic trend is expressed by Kendall's rank correlation coefficient (tau) (Equation (12)) (Mann, 1945; Yue et al., 2002),

$$\tau = \frac{2S}{n(n-1)} \quad (12)$$

where $-1 \leq \tau \leq 1$. The test statistic S proposed by Mann (Mann, 1945) depends on a series of n repeated observations taken over equal time intervals (Equation (13)).

$$S = \sum_{i=1}^{n-1} \sum_{j=i+1}^{n} \begin{cases} -1, & if\ Y_j - Y_i < 0 \\ 0, & if\ Y_j - Y_i = 0 \\ 1, & if\ Y_j - Y_i > 0 \end{cases} \quad (13)$$

The MK test assumes the observations to be a set of statistically independent variables (Neeti and Eastman, 2011; von Storch, 1995) and the presence of serial correlation in SVI time series can lead to overestimating the portion of significant trends (Detsch et al., 2016; Neeti and Eastman, 2011). Because it appeared to be likely that changes in SVIs observed in Landsat time series are influenced by the underlying post-fire forest recovery process, it is worth considering the existence of a lag-one positive serial correlation (e.g., high observations may tend to follow high observations). Lag-one serial correlation was, thus, removed prior to applying the MK test using the trend-free pre-whitening procedure described in

Yue et al. (Yue et al., 2002) and implemented in the R (R Core Team 2018) package "zyp" (Bronaugh and Werner, 2018). Regression coefficients were used to predict the time required by each SVI to return to its pre-fire spectral values by setting the value of RDSVI equal to zero. Only those pixels displaying jointly a significant negative monotonic trend (α-level <0.01) in all of the SVIs in the MK test were considered reliable to assess recovery times.

2.3 Results

2.3.1 Relationship between field data and Landsat-derived SVIs

The Pearson's correlation test, employed to explore the linear relationship between tree canopy fractional cover available from field surveys and Landsat SVIs, produced slightly different values depending on the SVI (Figure 2.2). NDVI and FRI2 attained the lowest (0.66) and the highest (0.72) values of Pearson's *r*, respectively, whereas NDMI, NBR, and NBR2 showed identical results.

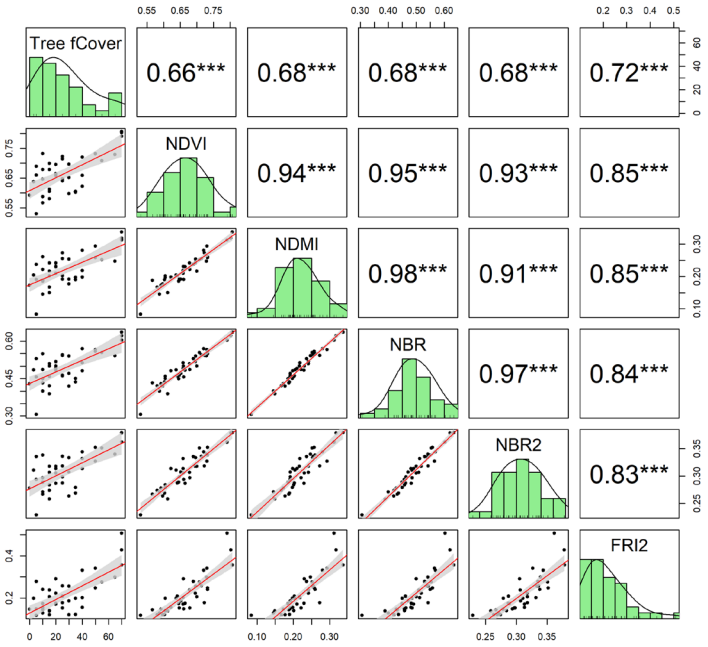

Figure 2.2. Correlation matrix of Pearson's test between tree fractional canopy cover (Tree fCover) obtained from field data and Landsat spectral vegetation indices (SVIs). Asterisks indicate that all tests were significant ($p < 0.001$).

2.3.2 Temporal trajectories of post-fire RDSVIs

Post-fire temporal trajectories of RDSVIs displayed that forest spectral recovery occurred as the difference of each SVI with its pre-fire value was reduced through the years (Figure 2.3). Different recovery patterns occurred between SVIs (rows in Figure 2.3) and between study areas, burn severity classes, and forest types (columns in Figure 2.3). SVIs exhibited noticeable differences concerning the variation range, the short-term post-fire behavior (three years), and inter-annual fluctuations. A wider range of values was observed in NDMI, NBR, and FRI2 compared to NBR2 and NDVI. The short-term post-fire behavior of normalized SVIs (NDVI, NDMI, NBR, and NBR2) displayed a sharp recovery, whereas FRI2 highlighted a more constant recovery rate through time. Inter-annual fluctuations of NDVI, NBR2, and FRI2 were less pronounced compared to those of NDMI and NBR. Recovery patterns of study areas RF and RM were similar through the entire time series as observed between study areas NA and LA (Figure 2.3a). Patterns of temporal trajectories at different burn severity classes highlighted that forest spectral recovery in the low and moderate class was generally at an advanced stage at the end of the time series (Figure 2.3b). Temporal trajectories at different forest types highlighted that broadleaved-dominated stands achieved slightly higher spectral recovery than those dominated by conifers (Figure 2.3c).

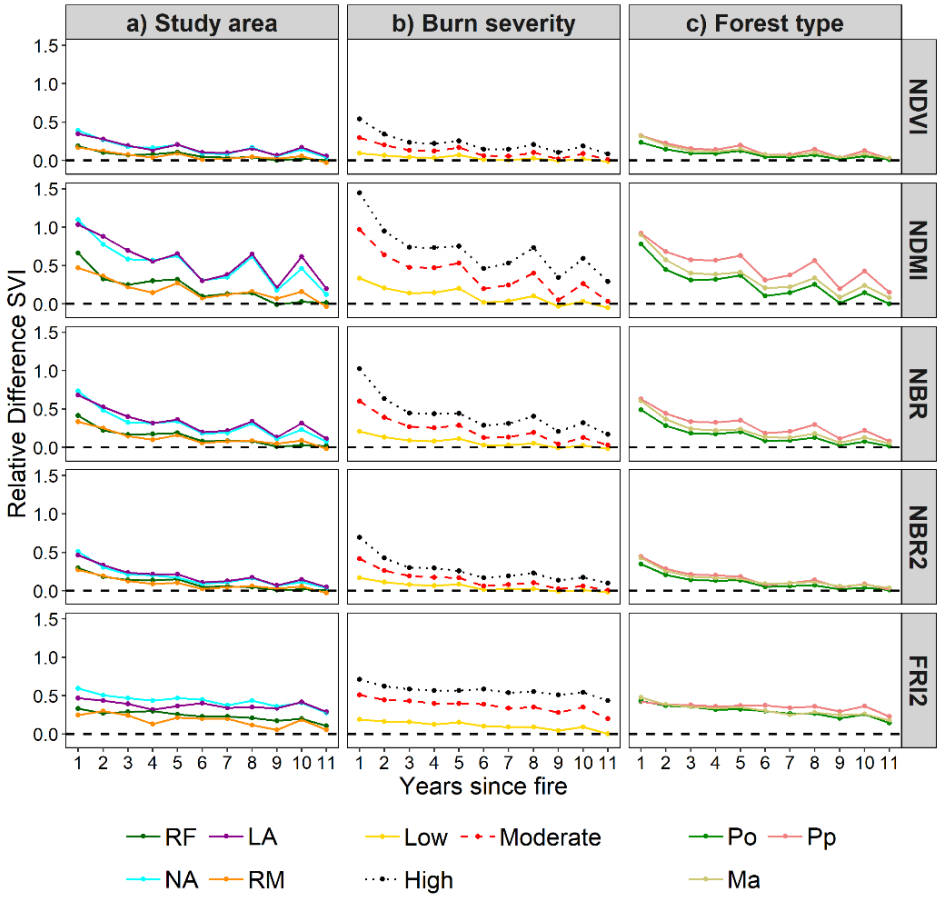

Figure 2.3. Post-fire temporal trajectories of Relative Difference SVIs (RDSVIs) (*y*-axis) at one-year intervals (*x*-axis) divided by study area (**a**), burn severity (**b**), and forest type (**c**). Years are expressed relative to fire occurrence. Study areas: Roccafluvione (RF), L'Aquila (LA), Navelli (NA), and Roccamorice (RM). Forest types: Po (pubescent oak), Pp (pine plantations), and Ma (manna ash and European hop-hornbeam).

2.3.3 Percentage of SVI recovered pixels

The percentage of recovered pixels for each SVI was computed considering pixels that completely recovered their pre-fire values by the 11th year after fire occurrence. They were aggregated by study area, burn severity class (Figure 2.4a), and forest type (Figure 2.4b). On average, NDVI displayed the highest

percentage (38.26%) compared to NDMI (28.83%), NBR (27.54%), NBR2 (26.23%), and FRI2 (24.92%). Differences between NDVI and the other SVIs increased for burn severity classes. In the high-burn-severity class, NDVI recovered 12.34% of pixels, whereas the average over NDMI, NBR, NBR2, and FRI2 was 5.5% (Figure 2.4a). Moreover, FRI2 displayed a larger separation between the recovered pixel percentage in the low class compared to the moderate and the high classes. Notably, the percentage of NDVI recovered pixels in Pp forests was higher (35.35%) compared to the mean value of the other SVIs (19.96%). The comparison between burn severity classes highlighted relevant differences of recovered pixel percentages, since the SVI averages were 50.36%, 29.42%, and 6.87% in the low, moderate, and high class, respectively. Within forest types, averaged recovery percentage of Po (32.03%) was higher than the averages of Pp (23.04%) and Ma (18.67%) (Figure 4b).

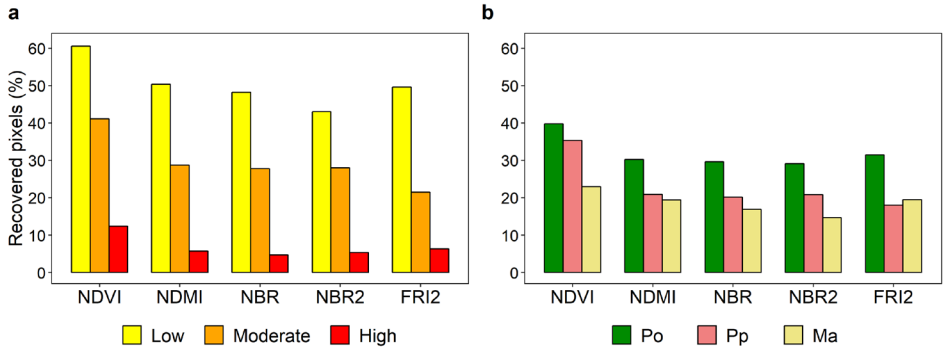

Figure 2.4. Percentage of recovered pixels aggregated by burn severity class (**a**) and forest type (**b**). Po: pubescent oak; Pp: pine plantations; Ma: mixed manna ash and European hop-hornbeam.

2.3.4 Long-term trends of RDSVIs

Long-term forest spectral recovery was evaluated through the median value of time required to attain pre-fire spectral conditions (Table 2.3) and by assessing the proportion of negative ($\tau < 0$) or positive ($\tau > 0$) significant trends ($p < 0.01$)

to the total amount of detected trends at the pixel level (Table 2.4). The number of pixels displaying a significant negative simultaneous trend of all the SVIs was 2385 (214.65 ha). Among normalized SVIs, differences of the predicted recovery time length within each burn severity class and each forest type were very limited considering that the largest one was in pine plantations, and spanned over 1.27 years. The recovery time instead varied among different fire severity classes and ranged from 8.56 years of NDMI in the low-burn-severity class to 12.20 years of NBR2 in the high-severity class. As for forest types, years ranged between 9.74 for NDVI and 12.36 for NBR2 in Po and Ma, respectively. FRI2 instead required a longer time to attain spectral recovery compared to normalized SVIs. The difference in recovery time between FRI2 and the average of the normalized SVIs, expressed as the absolute value of years and as the relative difference, ranged from 1.3 years (14.7%) in the low-burn-severity class to 6.2 years (51.8%) in the high-burn-severity class. Among forest types, these differences varied from two years (19.5%) in Po to 4.9 years (45.9%) in Pp. The spatial distribution of Kendall's tau provided for each study area (Figure 2.5) depicts where recovering (green) or declining trends (red) were strictly monotonic and, thus, statistically significant for the MK test, depending upon each RDSVI. Considering those pixels exhibiting a recovery trend (negative tau), the percentage of significant ones was noticeably different both for SVIs and study areas (Table 2.4). Over the four study areas, FRI2 attained the lowest mean percentage of significant recovery trends (9.04%) compared to normalized SVIs (22.31%). In particular, study areas RM and LA exhibited the lowest percentage of significant recovering trends with FRI2, while this difference was less evident considering normalized SVIs. Moreover, FRI2 displayed a noticeable amount of pixels with a significant declining trend in the study area LA (5.6%) which was higher than those with a recovery trend (3.67%) (Figure 2.5).

Table 2.3. Median values and interquartile ranges (IQRs) of years required to complete forest spectral recovery within burn severity classes and forest types by pixels with a significant recovery trend of each Relative Difference spectral

vegetation index (RDSVI) ($p < 0.01$). Po: pubescent oak; Pp: pine plantations; Ma: mixed manna ash and European hop-hornbeam.

		NDVI (IQR)	NDMI (IQR)	NBR (IQR)	NBR2 (IQR)	FRI2 (IQR)
Burn severity	Low	8.99 (3.82)	8.56 (3.68)	8.85 (3.67)	8.93 (4.19)	10.13 (6.85)
	Moderate	9.88 (3.27)	9.70 (3.23)	10.03 (3.02)	9.93 (3.75)	13.38 (10)
	High	12.02 (2.53)	11.68 (3.19)	11.93 (2.39)	12.20 (2.84)	18.15 (14.13)
Forest type	Po	9.74 (3.49)	11.01 (4.42)	10.59 (3.49)	9.98 (3.99)	12.35 (11.54)
	Pp	11.1 (3.25)	10.08 (2.89)	10.73 (2.80)	11.12 (3.33)	15.69 (11.39)
	Ma	12.18 (3)	11.53 (3.56)	11.85 (2.73)	12.36 (3.44)	15.58 (13.32)

Table 2.4. Percentage of pixels with a significant negative trend ($p < 0.01$) of RDSVIs with respect to the number of pixels within the area of interest of the study areas. Study areas are Roccafluvione (RF), L'Aquila (LA), Navelli (NA), and Roccamorice (RM).

	Study area	NDVI	NDMI	NBR	NBR2	FRI2
Percentage with a negative trend ($\tau < 0$)	RF	26.86	36.48	39.88	38.42	18.24
	LA	19.49	16.04	21.97	27.92	3.67
	NA	14.87	18.9	26.99	19.06	10.9
	RM	7.56	10.65	17.07	14.87	3.35

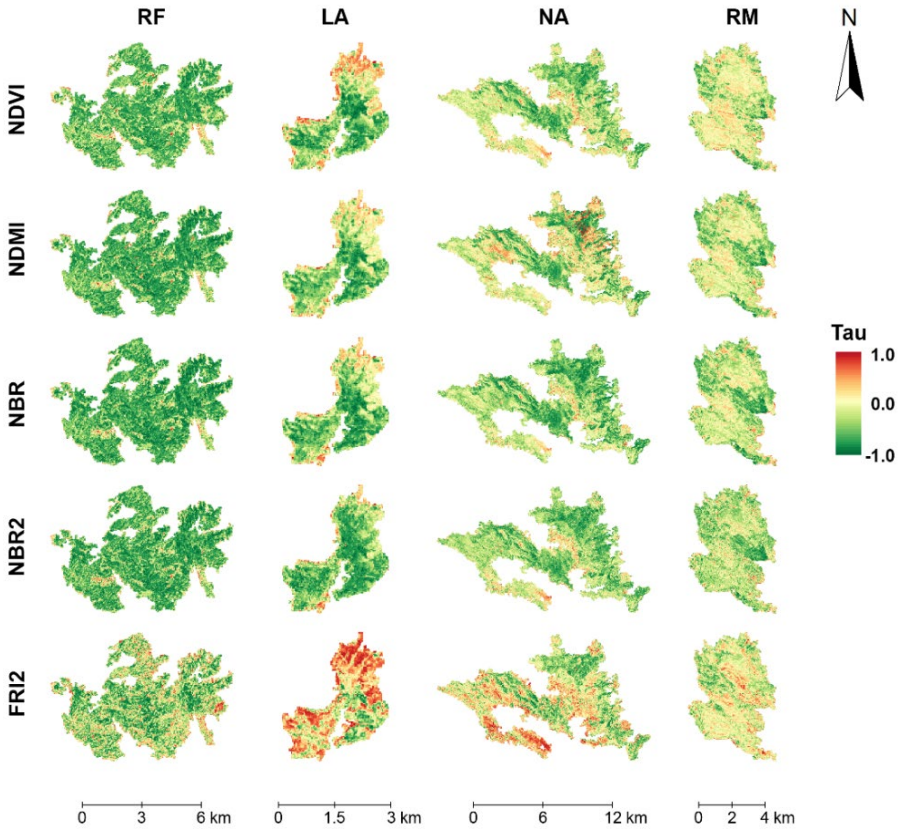

Figure 2.5. Maps of Kendall's tau rank correlation coefficient relative to RDSVI trends obtained with the Mann–Kendall test. Kendall's tau values range from 1 to −1. Positive values of tau are related to declining trends, whereas negative trends highlight spectral recovery. Study areas are Roccafluvione (RF), Navelli (NA), Roccamorice (RM), and L'Aquila (LA).

2.4 Discussion

2.4.1 Main differences between SVIs when tracking forest spectral recovery dynamics

Post-fire forest spectral recovery observed in four landscapes of the central Apennines is an ongoing heterogeneous process described by the decreasing patterns of the recovery metric (RDSVI) computed with all the SVIs.

Nevertheless, substantial differences between the temporal patterns of the SVIs were observed. The different variation range between normalized SVIs is related to the sensitivity of each Landsat band to early post-fire changes (Key and Benson, 2006; White et al., 1996) in terms of magnitude and direction. In this sense, post-fire variations were found to be higher in those SVIs contrasting one of the two SWIR bands and the NIR band (NDMI, NBR) compared to those using the Red and NIR bands (NDVI) or both the SWIR bands (NBR2) (Figure 2.3). The ability of normalized SVIs to track the rapid spectral recovery occurring soon after the fire seems related to their sensitivity toward non-arboreal vegetation dynamics rather than to tree canopy cover development, as observed in comparisons with IFZ (Chen et al., 2011) and FRI (Chu et al., 2016). The inter-annual variability of NDVI, NDMI, and NBR was higher respect to that of NBR2 and FRI2. Since sun angle effects should be minimized by the compositing algorithm, which prioritized images acquired closer to a reference Julian day, inter-annual fluctuations seem more influenced by phenological and precipitation effects. As observed by Song et al. (Song and Woodcock, 2003), phenology variations in young stands affect the red, the near-infrared, and the shortwave-infrared bands, which are the ones employed by NDVI, NDMI, and NBR. On the contrary, NBR2 seems less sensitive to variations due to precipitation effects (Storey et al., 2016) and FRI2 also minimized inter-annual fluctuations through yearly spectral statistics of dense forest cover, displaying a linear behavior through time. The higher percentage of recovered pixels achieved by NDVI at the 11th post-fire year compared to the other SVIs (Figure 2.4) confirmed its broad sensitivity to the amount of photosynthetically active vegetation (herbs, forbs, shrubs, and tree regeneration) (Buma, 2012; Schroeder et al., 2011). On the contrary, SVIs based on the SWIR bands were characterized by a low percentage of recovered pixels, indicating their higher sensitivity both to fire damages on forest cover and to the following forest structure recovery as observed in several studies on post-fire forest recovery monitoring using optical remote sensing (Cuevas-González et al., 2009; Pickell et al., 2016; Schroeder et al., 2011).

Results from field-based measurements indicated FRI2 as the most correlated with tree canopy fractional cover.

2.4.2 Forest spectral recovery of different burn severity classes and forest types

Although thresholds employed for burn severity classes were not meant to be used in these study areas, post-fire spectral recovery differences were clearly recognizable at increasing burn severity degrees. This distinction was observed both in the temporal trajectories of RDSVIs (Figure 2.3b) and in the pixel recovery percentages at the 11th post-fire year (Figure 2.4a). Also, these results highlighted that there was slightly more similarity between the recovery achieved at the moderate- and high-burn-severity classes by FRI2 compared to that attained with normalized SVIs. Among the latter, it was also observed that SWIR-based SVIs (NDMI, NBR, and NBR2) achieved considerably lower recovery compared to that of NDVI (Figure 2.4a). Since serious damages likely occurred to the over-story layers at the moderate- and high-burn-severity classes, this seemed to greatly influence the recovery of FRI2 and SWIR-based normalized SVIs. This result suggests that primarily FRI2 and secondly SWIR-based normalized SVIs are sensitive to the gradual development of tree canopy cover. Similar results were already observed through the correlation between field measurements of burn severity and several differenced (post-fire minus pre-fire) SVIs at multiple time intervals (Chen et al., 2011). Differences observed in the recovery of SVIs between forest types 11 years after fire occurrence seemed to be mainly driven by the magnitude of spectral changes detected soon after the fires (Figure 2.3c).

2.4.3 Forest spectral recovery time derived from monotonic trends

Modeling trends of the SVI recovery metrics in a spatially explicit manner by coupling Mann–Kendall and Theil–Sen methods allowed for the investigation of the rate of change at those pixels with a monotonically decreasing trend over time. Spectral trends at those locations can be confidently attributed to the development

of a post-fire secondary succession (Czerwinski et al., 2014; Frazier et al., 2018; Olthof et al., 2014). In this study, normalized SVIs exhibited spectral recovery periods of 12 years or less. However, the periods required by FRI2 to recover were up to 50% longer than normalized SVIs, particularly in the high-burn-severity class. This suggested that FRI2 is more suitable for tracking long-term forest recovery which results in slow rates of spectral changes due to the re-establishment of pre-fire tree canopy cover (*sensu* Frolking et al., 2009). The sensitivity of IFZ and FRI to the advanced stages of the forest succession was observed in other studies addressing post-fire forest recovery assessment through different SVIs (Chen et al., 2011; Chu et al., 2016) and using IFZ alone (Zhao et al., 2016). The results obtained from the prediction of spectral recovery time were partly in disagreement with those of recovery percentages (Figure 2.4) as, in this latter analysis, few differences between normalized SVIs were observed. This can be explained because the number of pixels used to predict spectral recovery time was 2385, equal to 3.4% of the number of pixels involved in the analysis (69,444). These pixels were selected applying two major constraints to the trends of the recovery metric of SVIs. It was required that the RDSVI trends were significant in the MK test ($p < 0.01$) and that this was concurrently true at the same location. Despite the limited number of pixels, this approach allowed for the comparison between the recovery time of SVIs integrating spatial information. The resulting number of pixels was likely influenced by the lower percentage of significant trends of FRI2 compared to that of normalized SVIs (Table 2.4). Several factors could have limited the percentage of FRI2 pixels having a significant recovery trend in the MK test. Among these factors, FRI showed sensitivity to the delay of post-fire mortality of damaged tree crowns (Chu et al., 2016). Thus, a subtle decline in tree canopies throughout the analyzed period could produce significant declining trends of the FRI2 recovery metrics. This was particularly relevant in the LA study area (Figure 2.5), where the percentage of significant declining trends was 5.6% of all the forest burned pixels, which was slightly higher than the percentage of recovery trends (3.67%). Also, it is arguable that delayed mortality of tree crowns occurring during the analysis period produced a shift in

the direction of the spectral changes, resulting in statistically non-significant trends of the FRI2 recovery metrics. These factors highlighted that temporal trajectories of FRI2 at early stages of post-fire forest succession are generally non-monotonic compared to that of normalized SVIs. Hence, it is advisable that the assessment of significant trends with the MK test at the pixel level be performed considering the advanced stages of forest recovery. Moreover, benefits could come from the use of a contextual approach, exploiting the information of neighboring trends to assess their monotonicity with the MK test (Neeti and Eastman, 2011).

2.5 Conclusions

Assessing post-fire forest regeneration dynamics by means of multi-temporal change detection analysis with Landsat imagery and SVIs allowed exploring different temporal scales of this process. In order to better estimate the future trajectories of forest recovery, it is crucial to understand which SVI can serve better to achieve this scope. Modeling changes of SVIs over a sufficient period with a robust regression approach can effectively address this matter. This study highlighted that the enhanced FRI2 ability to track long-term forest regeneration dynamics could be associated with ecologically meaningful results regarding the length of the forest recovery process and referring to the re-establishment of a continuous canopy cover over the burned areas. Therefore, the choice of the most suitable SVI for post-fire vegetation recovery assessment should be based upon the existing type of vegetation cover and the appropriate timescale. Early to medium stages of the post-fire forest secondary succession can be monitored using a normalized index employing the SWIR bands. However, at a time scale wider than 10–12 years, FRI2 provided reliable results through linear modeling extrapolation. Further research is needed to test its suitability at advanced stages of post-fire forest recovery.

Acknowledgments

The authors wish to thank Francesco Malandra for his contribution to field data collection.

References

Baatz, M., Schäpe, A., 2000. Multiresolution segmentation: An optimization approach for high quality multi-scale image segmentation. Angew. Geogr. informationsverarbeitung XI beiträge zum Agit. Salzbg.

Banskota, A., Kayastha, N., Falkowski, M.J., Wulder, M.A., Froese, R.E., White, J.C., 2014. Forest Monitoring Using Landsat Time Series Data: A Review. Can. J. Remote Sens. 40, 362–384. https://doi.org/10.1080/07038992.2014.987376

Bartels, S.F., Chen, H.Y.H., Wulder, M.A., White, J.C., 2016. Trends in post-disturbance recovery rates of Canada's forests following wildfire and harvest. For. Ecol. Manage. 361, 194–207. https://doi.org/10.1016/j.foreco.2015.11.015

Benz, U.C., Hofmann, P., Willhauck, G., Lingenfelder, I., Heynen, M., 2004. Multi-resolution, object-oriented fuzzy analysis of remote sensing data for GIS-ready information. ISPRS J. Photogramm. Remote Sens. 58, 239–258. https://doi.org/10.1016/j.isprsjprs.2003.10.002

Bronaugh, D., Werner, A., 2018. Package "zyp" Zhang + Yue-Pilon trends [WWW Document]. URL https://cran.r-project.org/web/packages/zyp/index.html (accessed 11.1.18).

Buma, B., 2012. Evaluating the utility and seasonality of NDVI values for assessing post-disturbance recovery in a subalpine forest. Environ. Monit. Assess. 184, 3849–3860. https://doi.org/10.1007/s10661-011-2228-y

Camia, A., Amatulli, G., 2009. Weather Factors and Fire Danger in the Mediterranean, in: Earth Observation of Wildland Fires in Mediterranean Ecosystems. Springer-Verlag, Berlin Heidelberg, pp. 71–82. https://doi.org/10.1007/978-3-642-01754-4_6

Capitanio, R., Carcaillet, C., 2008. Post-fire Mediterranean vegetation dynamics and diversity: A discussion of succession models. For. Ecol. Manage. 255, 431–439. https://doi.org/10.1016/j.foreco.2007.09.010

Chen, X., Vogelmann, J.E., Rollins, M., Ohlen, D., Key, C.H., Yang, L., Huang, C., Shi, H., 2011. Detecting post-fire burn severity and vegetation recovery using multitemporal remote sensing spectral indices and field-collected composite burn index data in a ponderosa pine forest. Int. J. Remote Sens. 32, 7905–7927. https://doi.org/10.1080/01431161.2010.524678

Chu, T., Guo, X., 2013. Remote sensing techniques in monitoring post-fire effects and patterns of forest recovery in boreal forest regions: A review. Remote Sens. 6, 470–520. https://doi.org/10.3390/rs6010470

Chu, T., Guo, X., Takeda, K., 2016. Remote sensing approach to detect post-fire vegetation regrowth in Siberian boreal larch forest. Ecol. Indic. 62, 32–46. https://doi.org/10.1016/j.ecolind.2015.11.026

Clemente, R.H., Navarro Cerrillo, R.M., Gitas, I.Z., 2009. Monitoring post-fire regeneration in Mediterranean ecosystems by employing multitemporal satellite imagery. Int. J. Wildl. Fire 18, 648–658. https://doi.org/10.1071/WF07076

Cohen, W.B., Goward, S.N., 2004. Landsat's Role in Ecological Applications of Remote Sensing. Bioscience 54, 535. https://doi.org/10.1641/0006-3568(2004)054[0535:LRIEAO]2.0.CO;2

Cohen, W.B., Yang, Z., Kennedy, R., 2010. Detecting trends in forest disturbance and recovery using yearly Landsat time series: 2. TimeSync - Tools for calibration and validation. Remote Sens. Environ. 114, 2911–2924. https://doi.org/10.1016/j.rse.2010.07.010

Conover, W.L., 1980. Practical nonparametric statistics, 2nd ed. New York.

Cuevas-González, M., Gerard, F., Balzter, H., Riaño, D., 2009. Analysing forest recovery after wildfire disturbance in boreal Siberia using remotely sensed vegetation indices. Glob. Chang. Biol. 15, 561–577. https://doi.org/10.1111/j.1365-2486.2008.01784.x

Czerwinski, C.J., King, D.J., Mitchell, S.W., 2014. Mapping forest growth and

decline in a temperate mixed forest using temporal trend analysis of Landsat imagery, 1987-2010. Remote Sens. Environ. 141, 188–200. https://doi.org/10.1016/j.rse.2013.11.006

de Rigo, D., Libertà, G., Houston Durrant, T., Artés Vivancos, T., San-Miguel-Ayanz, J., 2017. Forest fire danger extremes in Europe under climate change: variability and uncertainty. Publications Office of the European Union, Luxembourg. https://doi.org/10.2760/13180

Detsch, F., Otte, I., Appelhans, T., Nauss, T., 2016. A comparative study of cross-product NDVI dynamics in the Kilimanjaro region-a matter of sensor, degradation calibration, and significance. Remote Sens. 8. https://doi.org/10.3390/rs8020159

Diaz-Delgado, R., Pons, X., Díaz-Delgado, R., Pons, X., 2001. Spatial patterns of forest fires in Catalonia (NE of Spain) along the period 1975-1995 analysis of vegetation recovery after fire. For. Ecol. Manage. 147, 67–74. https://doi.org/10.1016/S0378-1127(00)00434-5

Diaz-Delgado, R., Salvador, R., Pons, X., 1998. Monitoring of plant community regeneration after fire by remote sensing, in: Trabaud, L. (Ed.), Fire Management and Landscape Ecology. International Association of Wildland Fire, pp. 315–324.

Didan, K., 2010. Multi-Satellite earth science data record for studying global vegetation trends and changes. Proc. 2010 Int. Geosci. Remote Sens. Symp. 2530.

ESA Online Dissemination [WWW Document], 2018. URL https://landsat-ds.eo.esa.int/ (accessed 12.20.18).

FAO, 1998. FRA 2000 Terms and Definitions. FAO Forestry Department, Rome.

Fick, S.E., Hijmans, R.J., 2017. WorldClim 2: new 1-km spatial resolution climate surfaces for global land areas. Int. J. Climatol. 37, 4302–4315. https://doi.org/10.1002/joc.5086

Frazier, R.J., Coops, N.C., Wulder, M.A., Hermosilla, T., White, J.C., 2018. Analyzing spatial and temporal variability in short-term rates of post-fire vegetation return from Landsat time series. Remote Sens. Environ. 205, 32–

45. https://doi.org/10.1016/j.rse.2017.11.007

Frolking, S., Palace, M.W., Clark, D.B., Chambers, J.Q., Shugart, H.H., Hurtt, G.C., 2009. Forest disturbance and recovery: A general review in the context of spaceborne remote sensing of impacts on aboveground biomass and canopy structure. J. Geophys. Res. Biogeosciences 114. https://doi.org/10.1029/2008JG000911

Giglio, L., Boschetti, L., Roy, D.P., Humber, M.L., Justice, C.O., 2018. The Collection 6 MODIS burned area mapping algorithm and product. Remote Sens. Environ. 217, 72–85. https://doi.org/10.1016/j.rse.2018.08.005

Gitas, I., Mitri, G., Veraverbeke, S., Polychronaki, A., 2012. Advances in remote sensing of post-fire vegetation recovery monitoring–a review. Remote Sens. Biomass–Principles Appl. 322.

Goetz, S.J., Bond-Lamberty, B., Law, B.E., Hicke, J.A., Huang, C., Houghton, R.A., McNulty, S., O'Halloran, T., Harmon, M., Meddens, A.J.H., Pfeifer, E.M., Mildrexler, D., Kasischke, E.S., 2012. Observations and assessment of forest carbon dynamics following disturbance in North America. J. Geophys. Res. Biogeosciences 117, 1–17. https://doi.org/10.1029/2011JG001733

GRASS Development Team, 2017. Geographic Resources Analysis Support System (GRASS) Software. Open Source Geospatial Found.

Hardisky, M.A., Klemas, V., Smart, R.M., 1983. The influence of Soil Salinity, Growth Form, and Leaf Moisture on the Spectral Radiance of Spartina alterniflora Canopies. Photogramm. Eng. Remote Sensing 49, 77–83.

Hernandez, C., Drobinski, P., Turquety, S., Dupuy, J.L., 2015. Size of wildfires in the Euro-Mediterranean region: Observations and theoretical analysis. Nat. Hazards Earth Syst. Sci. 15, 1331–1341. https://doi.org/10.5194/nhess-15-1331-2015

Hislop, S., Jones, S., Soto-Berelov, M., Skidmore, A., Haywood, A., Nguyen, T., 2018. Using Landsat Spectral Indices in Time-Series to Assess Wildfire Disturbance and Recovery. Remote Sens. 10, 460. https://doi.org/10.3390/rs10030460

Huang, C., Davis, L.S., Townshend, J.R.G., 2002. An assessment of support vector machines for land cover classification. Int. J. Remote Sens. 23, 725–749. https://doi.org/10.1080/01431160110040323

Huang, C., Goward, S.N., Masek, J.G., Thomas, N., Zhu, Z., Vogelmann, J.E., 2010. An automated approach for reconstructing recent forest disturbance history using dense Landsat time series stacks. Remote Sens. Environ. 114, 183–198. https://doi.org/10.1016/j.rse.2009.08.017

Huang, C., Song, K., Kim, S., Townshend, J.R.G., Davis, P., Masek, J.G., Goward, S.N., 2008. Use of a dark object concept and support vector machines to automate forest cover change analysis. Remote Sens. Environ. 112, 970–985. https://doi.org/10.1016/j.rse.2007.07.023

Jensen, J.R., 2014. Remote sensing of the environment: an earth resource perspective, 2nd ed, Prentice Hall, Upper Saddle River, NJ. Pearson Education Limited, Harlow.

Joint Research Centre, 2008. Forest Fires in Europe 2007. European Commission, Luxembourg. https://doi.org/1018-5593

Keeley, J.E., 2009. Fire intensity, fire severity and burn severity: A brief review and suggested usage. Int. J. Wildl. Fire 18, 116–126. https://doi.org/10.1071/WF07049

Kendall, M.G., 1975. Rank Correlation Methods, 4th editio. ed. Charles Griffin, London. https://doi.org/10.2307/1907752

Kennedy, R.E., Cohen, W.B., Schroeder, T.A., 2007. Trajectory-based change detection for automated characterization of forest disturbance dynamics. Remote Sens. Environ. 110, 370–386. https://doi.org/10.1016/j.rse.2007.03.010

Kennedy, R.E., Yang, Z., Cohen, W.B., 2010. Detecting trends in forest disturbance and recovery using yearly Landsat time series: 1. LandTrendr - Temporal segmentation algorithms. Remote Sens. Environ. 114, 2897–2910. https://doi.org/10.1016/j.rse.2010.07.008

Key, C.H., 2006. Ecological and Sampling Constraints on Defining Landscape Fire Severity. Fire Ecol. 2, 34–59.

https://doi.org/10.4996/fireecology.0202034

Key, C.H., Benson, N., Key, C.H., Benson, N., 1999. Measuring and remote sensing of burn severity: the CBI and NBR., in: Proceedings Joint Fire Science Conference and Workshop. University of Idaho and International Association of Wildland Fire, Boise, pp. 1999–2000.

Key, C.H., Benson, N.C., 2006. Landscape assessment: Sampling and analysis methods, in: Lutes, D.C. (Ed.), FIREMON: Fire Effects Monitoring and Inventory System. U.S. Department of Agriculture, Forest Service, Rocky Mountain Research Station, Fort Collins, p. 55.

Lhermitte, S., Verbesselt, J., Verstraeten, W.W., Coppin, P., 2010. A Pixel Based Regeneration Index using Time Series Similarity and Spatial Context. Photogramm. Eng. Remote Sens. 76, 673–682. https://doi.org/10.14358/PERS.76.6.673

Mann, H.B., 1945. Nonparametric Tests Against Trend. Econometrica 13, 245–259.

Masek, J.G., Vermote, E.F., Saleous, N.E., Wolfe, R., Hall, F.G., Huemmrich, K.F., Gao, F., Kutler, J., Lim, T., 2006. A Landsat Surface Reflectance Dataset. IEEE Geosci. Remote Sens. Lett. 3, 68–72. https://doi.org/10.1109/LGRS.2005.857030

Miller, J.D., Thode, A.E., 2007. Quantifying burn severity in a heterogeneous landscape with a relative version of the delta Normalized Burn Ratio (dNBR). Remote Sens. Environ. 109, 66–80. https://doi.org/10.1016/j.rse.2006.12.006

Moreira, F., Cardillo, E., Pausas, J.G., 2012. Post-Fire Management and Restoration of Southern European Forests, Post-Fire Management and Restoration of Southern European Forests. Springer Netherlands, Dordrecht. https://doi.org/10.1007/978-94-007-2208-8

Neeti, N., Eastman, J.R., 2011. A Contextual Mann-Kendall Approach for the Assessment of Trend Significance in Image Time Series. Trans. GIS 15, 599–611. https://doi.org/10.1111/j.1467-9671.2011.01280.x

Neteler, M., Bowman, M.H., Landa, M., Metz, M., 2012. GRASS GIS: A multi-

purpose open source GIS. Environ. Model. Softw. 31, 124–130. https://doi.org/10.1016/j.envsoft.2011.11.014

Nitze, I., Grosse, G., 2016. Detection of landscape dynamics in the Arctic Lena Delta with temporally dense Landsat time-series stacks. Remote Sens. Environ. 181, 27–41. https://doi.org/10.1016/j.rse.2016.03.038

Olthof, I., Fraser, R.H., Olthof, I., Kokelj, S. V., Lantz, T.C., Lacelle, D., Brooker, A., Wolfe, S., Schwarz, S., 2014. Detecting landscape changes in high latitude environments using landsat trend analysis: 2. classification. Remote Sens. 6, 11558–11578. https://doi.org/10.3390/rs61111533

Pan, Y., Birdsey, R.A., Fang, J., Houghton, R., Kauppi, P.E., Kurz, W.A., Phillips, O.L., Shvidenko, A., Lewis, S.L., Canadell, J.G., Ciais, P., Jackson, R.B., Pacala, S.W., McGuire, A.D., Piao, S., Rautiainen, A., Sitch, S., Hayes, D., Richard, A., Pekka, E., Werner, A., Oliver, L., Simon, L., Josep, G., Robert, B., Stephen, W., David, A., 2011. A large and persistent carbon sink in the world's forests. Science (80-.). 333, 988–993.

Parks, S.A., Dillon, G.K., Miller, C., 2014. A new metric for quantifying burn severity: The relativized burn ratio. Remote Sens. 6, 1827–1844. https://doi.org/10.3390/rs6031827

Pausas, J.G., Fernández-Muñoz, S., 2012. Fire regime changes in the Western Mediterranean Basin: From fuel-limited to drought-driven fire regime. Clim. Change 110, 215–226. https://doi.org/10.1007/s10584-011-0060-6

Pickell, P.D., Hermosilla, T., J. Frazier, R., Coops, N.C., Wulder, M.A., 2016. Forest recovery trends derived from Landsat time series for North American boreal forests. Int. J. Remote Sens. 37, 138–149. https://doi.org/10.1080/2150704X.2015.1126375

Qian, Y., Zhou, W., Yan, J., Li, W., Han, L., 2015. Comparing machine learning classifiers for object-based land cover classification using very high resolution imagery. Remote Sens. 7, 153–168. https://doi.org/10.3390/rs70100153

Röder, A., Hill, J., Duguy, B., Alloza, J.A., Vallejo, R., 2008. Using long time series of Landsat data to monitor fire events and post-fire dynamics and

identify driving factors. A case study in the Ayora region (eastern Spain). Remote Sens. Environ. 112, 259–273. https://doi.org/10.1016/j.rse.2007.05.001

Roy, D.P., Kovalskyy, V., Zhang, H.K., Vermote, E.F., Yan, L., Kumar, S.S., Egorov, A., 2016. Characterization of Landsat-7 to Landsat-8 reflective wavelength and normalized difference vegetation index continuity. Remote Sens. Environ. 185, 57–70. https://doi.org/10.1016/j.rse.2015.12.024

San-Miguel-Ayanz, J., Durrant, T., Boca, R., Libertà, G., Branco, A., de Rigo, D., Ferrari, D., Maianti, P., Vivancos, T.A., Costa, H., Lana, F., 2017. Forest Fires in Europe, Middle East and North Africa 2017. Joint Research Centre, Ispra. https://doi.org/10.2760/663443

San-Miguel-Ayanz, J., Moreno, J.M., Camia, A., 2013. Analysis of large fires in European Mediterranean landscapes: Lessons learned and perspectives. For. Ecol. Manage. 294, 11–22. https://doi.org/10.1016/j.foreco.2012.10.050

Scheffler, D., Hollstein, A., Diedrich, H., Segl, K., Hostert, P., 2017. AROSICS: An automated and robust open-source image co-registration software for multi-sensor satellite data. Remote Sens. 9. https://doi.org/10.3390/rs9070676

Scheller, R.M., Swanson, M.E., 2015. Simulating forest recovery following disturbances: Vegetation dynamics and biogeochemistry, in: Perera, A.H., Sturtevant, B.R., Buse, L.J. (Eds.), Simulation Modeling of Forest Landscape Disturbances. Springer International Publishing, Cham, pp. 263–285. https://doi.org/10.1007/978-3-319-19809-5_10

Schroeder, T.A., Wulder, M.A., Healey, S.P., Moisen, G.G., 2011. Mapping wildfire and clearcut harvest disturbances in boreal forests with Landsat time series data. Remote Sens. Environ. 115, 1421–1433. https://doi.org/10.1016/j.rse.2011.01.022

Sen, P.K., 1968. Estimates of the Regression Coefficient Based on Kendall's Tau. J. Am. Stat. Assoc. 63, 1379–1389. https://doi.org/10.1080/01621459.1968.10480934

Solans Vila, J.P., Barbosa, P., 2010. Post-fire vegetation regrowth detection in

the Deiva Marina region (Liguria-Italy) using Landsat TM and ETM+ data. Ecol. Modell. 221, 75–84. https://doi.org/10.1016/j.ecolmodel.2009.03.011

Song, C., Chen, J.M., Hwang, T., Gonsamo, A., Croft, H., Zhang, Q., Dannenberg, M., Zhang, Y., Hakkenberg, C., Li, J., 2015. Ecological characterization of vegetation using multisensor remote sensing in the solar reflective spectrum. L. Resour. Monit. Model. Mapp. with Remote Sens. 533–575. https://doi.org/doi:10.1201/b19322-28

Song, C., Woodcock, C.E., 2003. Monitoring Forest Succession with Multitemporal Landsat Images: Factors of Uncertainty. IEEE Trans. Geosci. Remote Sens. 41, 2557–2567. https://doi.org/10.1109/TGRS.2003.818367

Spasojevic, M.J., Bahlai, C.A., Bradley, B.A., Butterfield, B.J., Tuanmu, M.N., Sistla, S., Wiederholt, R., Suding, K.N., 2016. Scaling up the diversity-resilience relationship with trait databases and remote sensing data: The recovery of productivity after wildfire. Glob. Chang. Biol. 22, 1421–1432. https://doi.org/10.1111/gcb.13174

Storey, E.A., Stow, D.A., O'Leary, J.F., 2016. Assessing postfire recovery of chamise chaparral using multi-temporal spectral vegetation index trajectories derived from Landsat imagery. Remote Sens. Environ. 183, 53–64. https://doi.org/10.1016/j.rse.2016.05.018

Stroppiana, D., Bordogna, G., Carrara, P., Boschetti, M., Boschetti, L., Brivio, P.A., 2012. A method for extracting burned areas from Landsat TM/ETM+ images by soft aggregation of multiple Spectral Indices and a region growing algorithm. ISPRS J. Photogramm. Remote Sens. 69, 88–102. https://doi.org/10.1016/j.isprsjprs.2012.03.001

Tarquini, S., Nannipieri, L., 2017. The 10m-resolution TINITALY DEM as a trans-disciplinary basis for the analysis of the Italian territory: Current trends and new perspectives. Geomorphology 281, 108–115.

Theil, H., 1992. A Rank-Invariant Method of Linear and Polynomial Regression Analysis, in: Raj, B., Koerts, J. (Eds.), Henri Theil's Contributions to Economics and Econometrics. Advanced Studies in Theoretical and

Applied Econometrics. Springer, Dordrecht, pp. 345–381. https://doi.org/10.1007/978-94-011-2546-8_20

Tucker, C.., 1979. Red and photographic infarecd linear combinations for monitoring vegetation. Remote Sens. Enviroment, 8 150, 127–150. https://doi.org/Doi 10.1016/0034-4257(79)90013-0

Tzotsos, A., Argialas, D., 2008. Support Vector Machine Classification for Object-Based Image Analysis, in: Blaschke, T., Lang, S., Hay, G. (Eds.), Object-Based Image Analysis. Springer-Verlag Berlin Heidelberg, pp. 663–677. https://doi.org/10.1007/978-3-540-77058-9_36

USGS Earth Resources Observation and Science (EROS) Center Science Processing Architecture (ESPA) On Demand Interface [WWW Document], 2018. URL http://espa.cr.usgs.gov (accessed 12.20.18).

Vacchiano, G., Garbarino, M., Lingua, E., Motta, R., 2016. Forest dynamics and disturbance regimes in the Italian Apennines. For. Ecol. Manage. 388, 57–66. https://doi.org/10.1016/j.foreco.2016.10.033

van Gils, H., Odoi, J.O., Andrisano, T., 2010. From monospecific to mixed forest after fire?. An early forecast for the montane belt of Majella, Italy. For. Ecol. Manage. 259, 433–439. https://doi.org/10.1016/j.foreco.2009.10.040

Vegetation Index and Phenology Lab, T.U. of A., 2011. VIP Data Explorer V 4.1 [WWW Document]. URL https://vip.arizona.edu/viplab_data_explorer.php (accessed 12.20.18).

Veraverbeke, S., Lhermitte, S., Verstraeten, W.W., Goossens, R., 2010. The temporal dimension of differenced Normalized Burn Ratio (dNBR) fire/burn severity studies: The case of the large 2007 Peloponnese wildfires in Greece. Remote Sens. Environ. 114, 2548–2563. https://doi.org/10.1016/j.rse.2010.05.029

Veraverbeke, S., Somers, B., Gitas, I., Katagis, T., Polychronaki, A., Goossens, R., 2012. Spectral mixture analysis to assess post-fire vegetation regeneration using Landsat Thematic Mapper imagery: Accounting for soil brightness variation. Int. J. Appl. Earth Obs. Geoinf. 14, 1–11. https://doi.org/10.1016/j.jag.2011.08.004

Vermote, E., Justice, C., Claverie, M., Franch, B., 2016. Preliminary analysis of the performance of the Landsat 8/OLI land surface reflectance product. Remote Sens. Environ. 185, 46–56. https://doi.org/10.1016/j.rse.2016.04.008

Vermote, E.F., Tanré, D., Deuzé, J.L., Herman, M., Morcrette, J.-J., 1997. Second Simulation of the Satellite Signal in the Solar Spectrum, 6S: an overview. IEEE Trans. Geosci. Remote Sens. 35, 675–686. https://doi.org/10.1109/36.581987

Viedma, O., Meliá, J., Segarra, D., García-Haro, J., 1997. Modeling rates of ecosystem recovery after fires by using landsat TM data. Remote Sens. Environ. 61, 383–398. https://doi.org/10.1016/S0034-4257(97)00048-5

Vogelmann, J.E., Gallant, A.L., Shi, H., Zhu, Z., 2016. Perspectives on monitoring gradual change across the continuity of Landsat sensors using time-series data. Remote Sens. Environ. 185, 258–270. https://doi.org/10.1016/j.rse.2016.02.060

von Storch, H., 1995. Misuses of Statistical Analysis in Climate Research, in: Analysis of Climate Variability: Applications of Statistical Techniques. Springer, Berlin, Heidelberg, pp. 11–26. https://doi.org/https://doi.org/10.1007/978-3-662-03167-4_2

White, J.D., Ryan, K.C., Key, C.C., Running, S.W., 1996. Remote Sensing of Forest Fire Severity and Vegetation Recovery. Int. J. Wildl. Fire 6, 125–136. https://doi.org/10.1071/WF9960125

Yue, S., Pilon, P., Phinney, B., Cavadias, G., 2002. The influence of autocorrelation on the ability to detect trend in hydrological series. Hydrol. Process. 16, 1807–1829. https://doi.org/10.1002/hyp.1095

Zhao, F.A.R., Meng, R., Huang, C., Zhao, M., Zhao, F.A.R., Gong, P., Yu, L., Zhu, Z., 2016. Long-term post-disturbance forest recovery in the greater yellowstone ecosystem analyzed using Landsat time series stack. Remote Sens. 8, 2–3. https://doi.org/10.3390/rs8110898

Zhu, Z., Wang, S., Woodcock, C.E., 2015. Improvement and expansion of the Fmask algorithm: Cloud, cloud shadow, and snow detection for Landsats 4-

7, 8, and Sentinel 2 images. Remote Sens. Environ. 159, 269–277. https://doi.org/10.1016/j.rse.2014.12.014

Zhu, Z., Woodcock, C.E., 2012. Object-based cloud and cloud shadow detection in Landsat imagery. Remote Sens. Environ. 118, 83–94. https://doi.org/10.1016/j.rse.2011.10.028

Zhu, Z., Woodcock, C.E., Olofsson, P., 2012. Continuous monitoring of forest disturbance using all available Landsat imagery. Remote Sens. Environ. 122, 75–91. https://doi.org/10.1016/j.rse.2011.10.030

Supplementary material

Table S2.1. Detailed list of the Landsat data used in this study. Study areas are Roccafluvione (RF), L'Aquila (LA), Navelli (NA), and Roccamorice (RM).

Landsat sensor	WRS-2 Path/Row	Acquisition date (dd/mm/yyyy)	Landsat archive	Study area
TM	190/30	17/06/2001	USGS	RF
TM	190/30	03/07/2001	USGS	RF
TM	190/30	04/08/2001	USGS	RF
TM	190/30	20/06/2002	USGS	RF
TM	190/30	23/06/2003	USGS	RF
TM	190/30	09/06/2004	USGS	RF
TM	190/30	30/07/2005	USGS	RF
TM	190/30	15/06/2006	USGS	RF
TM	190/30	18/06/2007	USGS	RF
TM	190/30	20/07/2007	USGS	RF
TM	190/30	20/06/2008	USGS	RF
TM	190/30	07/08/2008	USGS	RF
TM	190/30	25/07/2009	USGS	RF
TM	190/30	12/07/2010	USGS	RF
TM	190/30	29/06/2011	USGS	RF
TM	190/30	16/08/2011	USGS	RF
ETM+	190/30	23/06/2012	USGS	RF

ETM+	191/30	30/06/2012	USGS	RF
OLI	190/30	05/08/2013	USGS	RF
OLI	190/30	08/08/2014	USGS	RF
OLI	191/30	01/07/2015	USGS	RF
OLI	190/30	10/07/2015	USGS	RF
OLI	190/30	26/06/2016	USGS	RF
OLI	190/30	13/06/2017	USGS	RF
OLI	190/30	02/07/2018	USGS	RF
OLI	190/30	18/07/2018	USGS	RF
TM	190/31	03/07/2001	USGS	LA; NA; RM
TM	190/31	19/07/2001	USGS	LA; NA; RM
ETM+	190/31	12/06/2002	USGS	LA; NA; RM
TM	190/31	20/06/2002	USGS	LA; NA; RM
TM	190/31	23/06/2003	USGS	LA; NA; RM
TM	190/31	09/06/2004	USGS	LA; NA; RM
TM	190/31	28/06/2005	USGS	LA; NA; RM
TM	190/31	14/07/2005	USGS	LA; NA; RM
TM	190/31	17/07/2006	USGS	LA; NA; RM
TM	190/31	18/06/2007	USGS	LA; NA; RM
TM	190/31	20/07/2007	USGS	LA; NA; RM
TM	190/31	06/07/2008	ESA	LA; NA; RM

TM	190/31	23/08/2008	ESA	LA; NA; RM
TM	190/31	25/07/2009	USGS	LA; NA; RM
TM	190/31	10/06/2010	USGS	LA; NA; RM
TM	190/31	26/06/2010	USGS	LA; NA; RM
ETM+	190/31	04/07/2010	USGS	LA; NA; RM
TM	190/31	12/07/2010	USGS	LA; NA; RM
TM	190/31	29/06/2011	USGS	LA; NA; RM
ETM+	190/31	07/07/2011	USGS	LA; NA; RM
TM	190/31	16/08/2011	USGS	LA; NA; RM
ETM+	190/31	23/06/2012	USGS	LA; NA; RM
ETM+	190/31	09/07/2012	USGS	LA; NA; RM
OLI	190/31	05/08/2013	USGS	LA; NA; RM
OLI	190/31	21/06/2014	USGS	LA; NA; RM
OLI	190/31	08/08/2014	USGS	LA; NA; RM
ETM+	190/31	02/07/2015	USGS	LA; NA; RM
OLI	190/31	10/07/2015	USGS	LA; NA; RM

ETM+	190/31	18/07/2015	USGS	LA; NA; RM
OLI	190/31	26/07/2015	USGS	LA; NA; RM
OLI	190/31	26/06/2016	USGS	LA; NA; RM
OLI	190/31	12/07/2016	USGS	LA; NA; RM
OLI	190/31	13/06/2017	USGS	LA; NA; RM
ETM+	190/31	23/07/2017	USGS	LA; NA; RM
OLI	190/31	31/07/2017	USGS	LA; NA; RM
OLI	190/31	02/07/2018	USGS	LA; NA; RM
OLI	190/31	18/07/2018	USGS	LA; NA; RM

Table S2.2. Landsat images used to map burn severity in the four study areas: Roccafluvione (RF), L'Aquila (LA), Navelli (NA), and Roccamorice (RM).

Study Area	**Acquisition timing**	**RF**	**LA**	**NA**	**RM**
Acquisition dates (dd-mm-yyyy)	Pre	15-06-2006	17-07-2006	17-07-2006	17-07-2006
	Post	07-08-2008	06-07-2008	06-07-2008	23-08-2008
WRS2 Path/Row	Pre	190/30	190/31	190/31	190/31
	Post	190/30	190/31	190/31	190/31
Landsat archive	Pre	USGS	USGS	USGS	USGS
	Post	USGS	ESA	ESA	ESA

Chapter 3

Mapping burn severity in the western Italian Alps through phenologically coherent reflectance composites derived from Sentinel-2 imagery

Donato Morresi, Raffaella Marzano, Emanuele Lingua, Renzo Motta and Matteo Garbarino

This chapter has been published open access in the Remote Sensing of Environment journal: Morresi, D., Marzano, R., Lingua, E., Motta, R., Garbarino, M., 2022. Mapping burn severity in the western Italian Alps through phenologically coherent reflectance composites derived from Sentinel-2 imagery. Remote Sens. Environ. 269. https://doi.org/10.1016/j.rse.2021.112800

Abstract

Deriving burn severity from multispectral satellite data is a widely adopted approach to infer the degree of environmental change caused by fire. Burn severity maps obtained by thresholding bi-temporal indices based on pre- and post-fire Normalized Burn Ratio (NBR) can vary substantially depending on temporal constraints such as matched acquisition and optimal seasonal timing. Satisfying temporal requirements is crucial to effectively disentangle fire and non-fire induced spectral changes and can be particularly challenging when only a few cloud-free images are available. Our study focuses on 10 wildfires that occurred in mountainous areas of the Piedmont Region (Italy) during autumn 2017 following a severe and prolonged drought period. Our objectives were to: (i) generate reflectance composites using Sentinel-2 imagery that were optimised for seasonal timing by embedding spatial patterns of long-term land surface phenology (LSP); (ii) produce and validate burn severity maps based on the modelled relationship between bi-temporal indices and field data; (iii) compare burn severity maps obtained using either a pair of cloud-free Sentinel-2 images,

i.e. paired images, or reflectance composites. We proposed a pixel-based compositing algorithm coupling the weighted geometric median and thematic spatial information, e.g. long-term LSP metrics derived from the MODIS Collection 6 Land Cover Dynamics Product, to rank all the clear observations available in the growing season. Composite Burn Index data and bi-temporal indices exhibited a strong nonlinear relationship (R^2 >0.85) using paired images or reflectance composites. Burn severity maps attained overall classification accuracy ranging from 76.9% to 83.7% (Kappa between 0.61 and 0.72) and the Relative differenced NBR (RdNBR) achieved the best results compared to other bi-temporal indices (differenced NBR and Relativized Burn Ratio). Improvements in overall classification accuracy offered by the calibration of bi-temporal indices with the dNBR offset were limited to burn severity maps derived from paired images. Reflectance composites provided the highest overall classification accuracy and differences with paired images were significant using uncalibrated bi-temporal indices (4.4% to 5.2%) while they decreased (2.8% to 3.2%) when we calibrated bi-temporal indices derived from paired images. The extent of the high severity category increased by ~19% in burn severity maps derived from reflectance composites (uncalibrated RdNBR) compared to those from paired images (calibrated RdNBR). The reduced contrast between healthy and burnt conditions associated with suboptimal seasonal timing caused an underestimation of burnt areas. By embedding spatial patterns of long-term LSP metrics, our approach provided consistent reflectance composites targeted at a specific phenological stage and minimising non-fire induced inter-annual changes. Being independent from the multispectral dataset employed, the proposed pixel-based compositing approach offers new opportunities for operational change detection applications in geographic areas characterised by persistent cloud cover.

3.1 Introduction

Fire is one of the major natural disturbance agents in European Alpine forests (Bebi et al., 2017; Kulakowski et al., 2016). Current fire regimes in the European Alps exhibit significant heterogeneity in terms of fire frequency, spatial extent and seasonality, according to the variability in climatic, environmental and anthropogenic drivers (Bebi et al., 2017; Conedera et al., 2018; Wastl et al., 2013; Zumbrunnen et al., 2011). Recent and projected increases in temperatures and drought conditions associated with climate change (Gobiet et al., 2014; Gobiet and Kotlarski, 2020; Gudmundsson and Seneviratne, 2016) are crucial factors for future shifts of fire regimes in the European Alps (Bedia et al., 2014; Cane et al., 2013; Schumacher and Bugmann, 2006), substantially increasing the probability of large wildfires occurrence (Barbero et al., 2019). Recently, the severe and prolonged drought conditions associated with heat waves that occurred during the summer of 2017 in several parts of south-central Europe (Rita et al., 2020) led to an anomalous fire season in many regions of France, Italy, Portugal and Spain (Turco et al., 2018).

Severity is one of the main factors influencing ecosystem responses, so its assessment is crucial to effectively guide post-fire management strategies aimed at promoting forest regeneration and the recovery of ecosystem services (Leverkus et al., 2018). From an ecological perspective, severity is defined as the magnitude of environmental change caused by fire (Key and Benson, 2006; Lentile et al., 2006). The term burn severity is commonly used in remote sensing applications (Keeley, 2009), and its differences with fire severity are related to the assessment period (Cansler and McKenzie, 2012; Lentile et al., 2006; Veraverbeke et al., 2010a). Fire severity commonly refers to an initial assessment of those effects directly related to combustion, such as fuel consumption and tree mortality measured immediately after the fire. On the contrary, burn severity refers to an extended assessment of severity, usually performed during the first growing season following the fire. This implicates that burn severity combines

fire effects and the initial ecosystem response, including delayed mortality and survivorship (Key, 2006).

Mapping burn severity with medium-resolution satellite imagery, e.g. Landsat data, acquired in the pre- and post-fire growing seasons, is typically performed through bi-temporal indices based on the Normalized Burn Ratio (NBR) (García and Caselles, 1991), such as the differenced Normalized Burn Ratio (dNBR, Key and Benson, 2006), the Relative dNBR (RdNBR, Miller and Thode, 2007) and the Relativized Burn Ratio (RBR, Parks et al., 2014). Ecologically meaningful burn severity maps can be produced by classifying bi-temporal indices using thresholds derived from parametric models incorporating field measures of burn severity (Key and Benson, 2006; Kolden et al., 2015). Commonly adopted field data comprehend the Composite Burn Index (CBI) (Cansler and McKenzie, 2012; Key and Benson, 2006) and its modifications, i.e. GeoCBI (De Santis and Chuvieco, 2009) and weighted CBI (Soverel et al., 2010), percentage change in tree canopy cover and tree basal area (Miller et al., 2009).

Given the influence of image selection on bi-temporal indices (Chen et al., 2020; Veraverbeke et al., 2010a), pre- and post-fire image pairs employed for computing bi-temporal indices should meet temporal requirements relative to matched acquisition and optimal seasonal timing (Key, 2006; Veraverbeke et al., 2010a). Image pairs with similar acquisition timing throughout the year enhance spectral matching between pre- and post-fire conditions, enabling to disentangle between spectral changes induced by fire and external factors (Eidenshink et al., 2007; Key, 2006; Miller and Thode, 2007; Veraverbeke et al., 2010b). Plant phenology, solar elevation angle, illumination variations due to topography, and moisture content of both soil and vegetation are among the most important external factors causing inter- and intra-annual changes in the spectral response of the land surface (Key, 2006; Key and Benson, 2006; Veraverbeke et al., 2010b; Verbyla et al., 2008). Several approaches are useful to limit the influence of such non-fire induced changes. For example, specific topographic correction techniques can effectively reduce pre- and post-fire differences in reflectance values arising from illumination effects associated with rugged terrains

(Veraverbeke et al., 2010b). Inter-annual variations in plant phenology and moisture content can be mitigated by performing a calibration based on dNBR values retrieved from the unburnt area surrounding the fire perimeter (Key, 2006; Meddens et al., 2016; Miller and Thode, 2007; Parks et al., 2014) and in the same forest type (Furniss et al., 2020; Picotte et al., 2020). The dNBR offset, usually computed as the average from the unburnt area and subtracted from the entire scene, should ideally be close to zero in the case of image pairs with matched spectral conditions (Key, 2006). This approach proved to be effective in improving the relationship between bi-temporal indices and CBI (Meddens et al., 2016; Parks et al., 2018). Nevertheless, extracting the dNBR offset can be a subjective process (Picotte et al., 2020) and depends on the spatial configuration of the landscape mosaic (Parks et al., 2018). In particular, the selection of an appropriate set of pixels requires the presence of similar forest types near the burnt area, and a single value could be suboptimal to calibrate inter-annual differences in multiple forest types or within burnt areas with a broad altitudinal gradient.

Optimal seasonal timing refers to the timing of image acquisition that maximises the contrast between healthy and burnt vegetation (Chen et al., 2020; Eidenshink et al., 2007; Key and Benson, 2006; Veraverbeke et al., 2010a). In temperate ecosystems, the optimal seasonal timing typically spans from early-to-middle growing season dates as the vegetation reaches its maximal photosynthetic activity (Eidenshink et al., 2007; Key, 2006; Key and Benson, 2006; Picotte et al., 2020). In burnt areas spanning a wide elevation range, the optimal seasonal timing can vary considerably, thus requiring multiple images to be processed (Key, 2006). Moreover, complex landscape mosaics such as those of the Mediterranean Basin exhibit a high degree of local variations in phenology associated with different land covers (Veraverbeke et al., 2010a).

The selection of appropriate image pairs poses challenges for the operational assessment of burn severity with bi-temporal indices, e.g. when large areas or a high number of fires are considered (Parks et al., 2018; Whitman et al., 2020). Specifically, the amount of time required by expert operators (Parks et al., 2018),

the lack of standardised procedures (Chen et al., 2020), and the availability of cloud-free images (French et al., 2008), especially during the first post-fire growing season (Key and Benson, 2006), constrain the usage of bi-temporal indices. Recent approaches to overcome the limitations above have been developed (Parks et al., 2018; Whitman et al., 2020). They rely on pixel-based mean compositing algorithms that exploit all the Landsat images available in the pre- and post-fire growing season. While producing spatially consistent results, the mean compositing method requires an effective removal of invalid pixels, i.e. those contaminated by clouds, cloud shadows or snow (Vancutsem et al., 2007). As accurately identifying cloud and cloud shadows in Landsat and Sentinel-2 imagery is an active research topic (Tarrio et al., 2020; Wei et al., 2020), compositing methods that minimise the importance of odd values would be preferable. Compositing algorithms based on multidimensional medians such as the medoid (Flood, 2013) and the geometric median (Roberts et al., 2017) can produce consistent pixel-based reflectance composites when the proportion of invalid values is less than half of the observations. The medoid approach belongs to the best pixel selection strategy group (*sensu* Griffiths et al., 2019), while the geometric median generates synthetic reflectance values, i.e. not actually sensed. The amount of available data considerably influences the quality of reflectance composites produced with the medoid (Roberts et al., 2017; Van Doninck and Tuomisto, 2017). However, the geometric median can produce spatially coherent reflectance values even when clear observations are scarce (Roberts et al., 2017). These methods have been successfully employed to produce image composites of Landsat imagery (Flood, 2013; Kennedy et al., 2018; Roberts et al., 2017; Van Doninck and Tuomisto, 2017).

A widely adopted best pixel selection strategy is parametric scoring, which involves assigning a possibly weighted sum of scores obtained from the evaluation of several parameters to each clear observation available within the compositing period for a given pixel location (Frantz et al., 2017; Griffiths et al., 2013; White et al., 2014). The acquisition Day-Of-Year (DOY) and year, the distance to clouds and cloud shadows, the sensor and the amount of atmospheric

haze are among the most used parameters. While target DOYs are often determined in a static fashion for producing reflectance composites over large areas (Griffiths et al., 2019, 2014; White et al., 2014), spatially explicit land surface phenology (LSP) metrics can serve to dynamically adjust scoring functions relative to the acquisition DOY for attaining phenological coherence (Frantz et al., 2017). Reflectance composites optimised for representing land surface at a specific phenological stage encompass climatic variations induced by both latitudinal and elevation gradients that can otherwise generate spectral inconsistencies when analysing vegetation dynamics over time (Frantz et al., 2017).

In the Western Italian Alps (Piedmont Region), several large wildfires simultaneously occurred in the second half of October 2017, outside of the fire season that typically spans from winter to early spring. They were favoured by exceptional summer drought conditions that lasted into the autumn associated with strong gusts of foehn wind (Arpa Piemonte, 2017; Bo et al., 2020). These events burnt nearly 10000 ha of forests, woodlands, shrublands and pastures and heavily affected the air quality of the surrounding urban areas (Bo et al., 2020). In response to these events, a post-fire management plan has been developed by the regional forest managers in cooperation with other stakeholders (Regione Piemonte, 2019), using burn severity maps produced by the University of Torino. Burn severity maps provided crucial information to identify areas that required prompt post-fire interventions. In fact, fire impaired the protective function of montane forests (e.g. Brang et al., 2006), i.e. protection against soil erosion, rockfall and avalanches, particularly in high severity patches.

Our general hypothesis is that phenologically coherent reflectance composites can increase both effectiveness and operational usage of bi-temporal indices for mapping burn severity. In particular, we expect that targeting surface reflectance in early to intermediate stages of the growing season can enhance the discrimination capability of bi-temporal burn severity indices, e.g. between fire and non-fire induced spectral changes. In this study, we aimed at achieving the following objectives: (i) to generate pre- and post-fire reflectance composites

optimised for burn severity mapping with Sentinel-2 imagery by embedding spatial patterns of long-term LSP metrics; (ii) to produce and validate burn severity maps based on the modelled relationship between bi-temporal indices and CBI data; (iii) to compare burn severity maps obtained by using either Sentinel-2 image pairs or reflectance composites.

3.2 Materials and Methods

3.2.1 Study area

Our study focuses on 10 burnt areas (Figure 3.1, Table 3.1) whose perimeters were mapped by the Carabinieri Command for Forest Protection through field surveys. We retrieved the start and end dates of each fire (Table 3.1) from the Visible Infrared Imaging Radiometer Suite (VIIRS) 375 m standard Active Fire product (Schroeder et al., 2014) distributed by NASA's Fire Information for Resource Management System (FIRMS). The extent of burnt areas ranged from 55 to 3974 ha, resulting in a total area of 9740 ha, of which forests covered 7202 ha, according to the Dominant Leaf Type map produced in 2015 (European Environmental Agency, 2018a). Burnt areas were mostly covered by montane and submontane broadleaved and coniferous forests. In particular, forests dominated by broadleaved species covered 4995 ha, and among tree species, sweet chestnut (*Castanea sativa* Mill.), European beech (*Fagus sylvatica* L.) and downy oak (*Quercus pubescens* Willd.) were the most abundant. The dominant coniferous tree species were European larch (*Larix decidua* Mill.), and Scots pine (*Pinus sylvestris* L.), covering 2207 ha of the total burnt area.

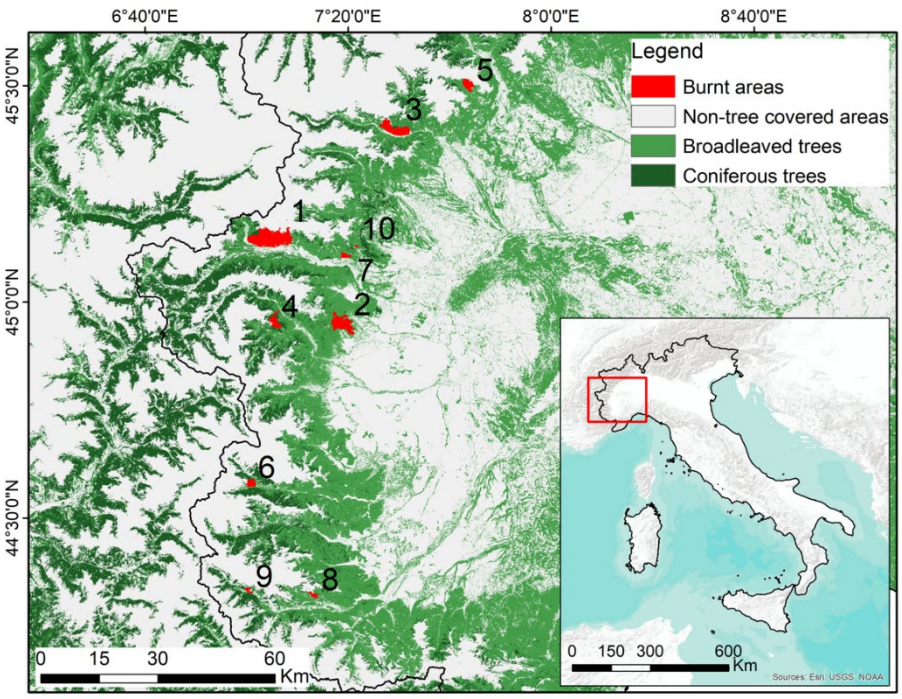

Figure 3.1. Geographic distribution of the burnt areas, sorted using their extent in decreasing order, from the largest to the smallest. Forest cover in the background corresponds to the Dominant Leaf Type map (reference year 2015, 20 m spatial resolution, European Environmental Agency, 2018a).

Table 3.1. Information regarding fire, landform, climate and forest cover properties of the burnt areas. For spatial data we report the average ± standard deviation. Column abbreviations are as follows: Ba = Burnt area; Ex = Extent; Sd = Start date; Ed = End date; El = Elevation; Te = Mean annual temperature; Pr = Mean annual precipitation; Br = Broadleaved tree cover; Co = Coniferous tree cover; Nf = Non-forest cover; Dt = Dominant tree species. Tree species abbreviations are: Eb = European beech; Sc = Sweet chestnut; Do = Downy oak; Mb = Mixed broadleaves; El = European larch; Sp = Scots pine.

Ba	Ex (ha)	Sd (yyyy-mm-dd)	Ed (yyyy-mm-dd)	El (m a.s.l.)	Te (°C)	Pr (mm)	Br (%)	Co (%)	Nf (%)	Dt
1	3974	2017-10-22	2017-10-30	1422 ±488	6.1 ±2.9	731 ±104	37.1	26.7	36.2	Eb; Sp
2	1818	2017-10-18	2017-10-31	853 ±242	9.7 ±1.4	786 ±65	94.1	5.1	0.8	Sc; Eb
3	1570	2017-10-23	2017-10-30	1190 ±340	7.4 ±1.9	729 ±63	61.8	21.3	16.9	Sc; Mb
4	666	2017-10-23	2017-10-30	1716 ±246	4.6 ±1.4	796 ±68	15.1	58.6	26.3	El; Mb
5	624	2017-10-25	2017-10-28	1487 ±325	5.5 ±1.9	868 ±99	32.7	2.2	65	Mb; Sc
6	378	2017-10-24	2017-10-29	1790 ±212	4.6 ±1.2	667 ±31	22.3	42.8	34.9	El; Mb
7	271	2017-10-23	2017-10-26	691 ±142	10.4 ±1	689 ±39	79.9	16.3	3.8	Sc; Mb
8	220	2017-10-28	2017-10-30	1423 ±197	6.8 ±1.2	803 ±45	72.3	3	24.7	Do; Eb
9	164	2017-10-22	2017-10-25	1489 ±173	6 ±1.3	730 ±31	15.5	60.6	23.9	Sp; El
10	55	2017-10-23	2017-10-25	911 ±67	9.2 ±0.5	705 ±19	92.6	3.2	4.2	Sc; Eb

3.2.2 General overview

We performed the analyses in two steps: fire severity (Section 3.2.5) and burn severity mapping (Section 3.2.6), as highlighted in Figure 3.2. Fire severity maps allowed us to develop the sampling design to collect CBI data in the burnt areas (Section 3.2.4). We employed LSP metrics during the selection of pre- and post-fire images, hereafter referred to as paired images, and to produce reflectance composites (Figure 3.2).

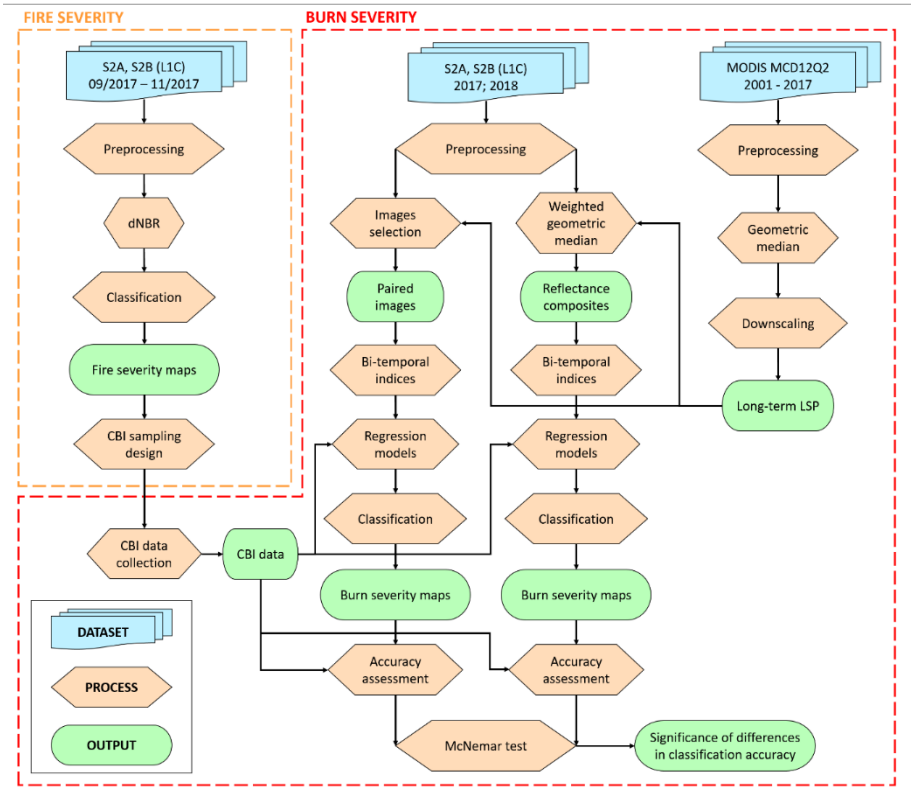

Figure 3.2. Flowchart of the analyses performed in the current study, grouped into fire severity and burn severity mapping steps.

3.2.3 Satellite data and preprocessing

We conducted the analyses using data acquired by the MultiSpectral Instrument (MSI) onboard Sentinel-2A (S2A) and Sentinel-2B (S2B) satellites. Specifically, we downloaded Sentinel-2 images containing Top-Of-Atmosphere (TOA) reflectance values processed according to Level-1C for the UTM-based Military Grid Reference System (MGRS) tiles 32TLQ and 32TLR. We preprocessed Sentinel-2 images employed for mapping fire severity (Section 3.2.5) and burn severity (Section 3.2.6) using different tools, depending on their availability when we performed the analyses. We mapped fire severity using Bottom-Of-Atmosphere (BOA) reflectance products obtained with the Sen2Cor 2.4.0 processor (Louis et al., 2016). We then removed pixels contaminated by clouds,

cloud shadows and snow by applying masks generated using the Function of mask (Fmask) version 4.0 software (Qiu et al., 2019). We mapped burn severity using BOA reflectance products derived with the Framework for Operational Radiometric Correction for Environmental monitoring (FORCE) software (version 3.6.5, available at https://github.com/davidfrantz/force) (Frantz, 2019). In particular, the FORCE Level 2 Processing System performed the following operations: (i) detection of clouds, cloud shadows and snow using a modified version of the Function of mask (Fmask) algorithm (Frantz et al., 2018); (ii) sub-pixel co-registration (Rufin et al., 2020); (iii) atmospheric correction (Frantz et al., 2016); (iv) topographic correction (Kobayashi and Sanga-Ngoie, 2008); (v) computation of Nadir BRDF (Bidirectional Reflectance Distribution Function)-Adjusted Reflectance (NBAR) (Roy et al., 2017a, 2017b). Sub-pixel co-registration, topographic correction and NBAR values were fundamental requirements for temporal and spatial consistency in a multi-temporal analysis setting (Frantz et al., 2016; Roy et al., 2017a; Rufin et al., 2020). As Sentinel-2 bands at 20 m spatial resolution, i.e. band 5 (B5), band 6 (B6), band 7 (B7), band 8A (B8A), band 11 (B11) and band 12 (B12), were processed by FORCE at 10 m by dividing each pixel into four sub-pixels, we resampled BOA reflectance values to the original 20 m grid using the cubic convolution method. For the Quality Assurance Information (QAI) masks resampling, we applied a conservative approach based on the "presence" rule proposed by Claverie et al. (2018): for each bit, in the case one of the four 10 m pixels within each original 20 m was equal to one, all four pixels were set to one. Additional processing operations included spatial subsetting based on buffers around wildfire perimeters and invalid pixels masking, i.e. those covered by clouds, cloud shadows, snow and saturated pixels using the relevant bits in the QAI mask. We processed raster data using the R (R Core Team, 2021) package "raster" (Hijmans, 2020).

3.2.4 Field data

We employed the Composite Burn Index (CBI) protocol (Key and Benson, 2006) to classify and validate bi-temporal indices derived for burn severity mapping (Section 3.2.6). CBI scores rely on ocular estimations of different factors grouped into five vertical strata: three in the understory and two in the overstory vegetation (Key and Benson, 2006). The final CBI score assigned to each plot assumed values in the interval [0 – 3], where zero corresponded to an unaltered condition and three to the maximum degree of fire induced changes. The CBI sampling design was based on fire severity maps (Section 3.2.5) and forest types. In particular, a stratified random scheme for plot selection allowed us to collect CBI data covering the whole range of its values within the dominant tree species. We located 20 m circular CBI plots at a minimum distance of 60 m from each other and at the centre of 3x3 windows of 20 m pixels characterised by a low variability in dNBR (Key and Benson, 2006). We placed centroids of CBI plots close to those of Sentinel-2 pixels using a survey-grade Trimble R2 GNSS antenna with sub-meter geolocation accuracy and performed differential correction of these locations. We assigned CBI scores with the supervision of the same person in order to minimise the variability introduced by different evaluators (Miller et al., 2009). We surveyed a total of 251 CBI plots from June to September 2018, distributed among the burnt areas as reported in Table S3.3. We classified CBI values into three severity categories: unchanged to low (CBI $\leq$ 1.25), moderate (CBI > 1.25 and $\leq$ 2.25) and high (CBI > 2.25) as proposed in other studies (Miller et al., 2009; Soverel et al., 2010). The distribution of CBI plots among severity categories was as follows: 51% in the unchanged to low, 33.5% in the moderate, and 15.5% in the high. In some areas, we were able to survey only a limited number of plots, i.e. less than 10, due to steep slopes and the lack of hiking trails for safely reaching the burned patches.

3.2.5 Fire severity

We mapped fire severity patterns using Sentinel-2 data acquired between September and November 2017 (Table S3.1). We computed pre- and post-fire NBR (Equation 1) using the near infrared (NIR) narrow band (MSI B8A) and the second shortwave infrared (SWIR) band (MSI B12) to derive dNBR (Table 3.2). We calibrated dNBR by subtracting the dNBR offset, which was the average dNBR of unburnt pixels close to each fire perimeter, located within a 200 m outer buffer. We employed a relatively narrow buffer to minimise differences between burnt and unburnt vegetation characteristics, as suggested by Parks et al. (2018). Furthermore, inside this region, we selected only pixels mainly covered by tree canopies, e.g. more than two-thirds, to limit the influence of phenological mismatches caused by other vegetation types. In particular, we performed the selection according to the Tree Cover Density map produced by the Copernicus Land Monitoring Service in 2015 at 20 m spatial resolution (European Environmental Agency, 2018b). We finally classified dNBR using thresholds proposed by Key and Benson (2006).

$$NBR = \frac{(NIR-SWIR)}{(NIR+SWIR)} \quad (1)$$

Table 3.2. Bi-temporal indices employed for mapping fire severity (dNBR) and burn severity (dNBR, RdNBR, RBR).

Index	Formula	Reference
dNBR	$\left(NBR_{pre-fire} - NBR_{post-fire}\right) \times 1000$	Key and Benson, 2006
RdNBR	$\frac{dNBR}{\sqrt{\lvert NBR_{pre-fire} \rvert}}$	Miller and Thode, 2007
RBR	$\frac{dNBR}{NBR_{pre-fire} + 1001}$	Parks et al., 2014

3.2.6 Burn severity

We mapped burn severity using bi-temporal indices based on NBR (dNBR, RdNBR, RBR) (Table 3.2) and performed the calibration through the dNBR offset. We employed either paired images acquired during the growing seasons of 2017 and 2018 or reflectance composites generated using all the clear observations available in these periods. Specifically, we defined a compositing period spanning from 20 May to 10 September as this date range falls within the growing season in the burnt areas. The phenology-based weight used in the compositing algorithm (Section 3.2.8) generally assumed minimum values, e.g. 0.01, at the start and end dates of this period.

For each burnt area, we obtained paired images by selecting pre- and post-fire images that were cloud-free, i.e. a percentage of valid pixels ≥95 and with matched acquisition dates, i.e. closest DOY as possible. If multiple paired images were available, we chose those closer to the long-term peak of the growing season, computed as described in Section 3.2.8.

3.2.7 Sentinel-2 reflectance composites

We produced reflectance composites using all the MSI bands acquired at 20 m spatial resolution and the weighted geometric median, also known as the Fermat-Weber location problem (Brimberg, 1995; Cohen et al., 2016; Vardi and Zhang, 2000). The weighted geometric median is an estimator of centrality for multivariate data based on the weighted sum of Euclidean distances to all the observations rather than on their sum, as in the case of the geometric median (Chaudhuri, 1996). It is effective for the generation of noise-reduced, cloud-free reflectance composites (Roberts et al., 2019).

At the pixel level, we considered a n x p matrix containing n repeated observations in rows and reflectance values relative to p spectral bands in columns. We assigned a weight to each observation based on a specific weighting system. This procedure, iterated over all the pixels forming the image, can be formally expressed as follows. Given n observations $y_i \in \mathbb{R}^p$ with associated

weights $w_i \in \mathbb{R}_{>0}$, $i = 1,\ldots,n$, the weighted geometric median is the vector $m_n \in \mathbb{R}^p$ that minimises the weighted sum of Euclidean distances from the n observations:

$$m_n = \operatorname{argmin}_{y \in \mathbb{R}^p} \sum_{i=1}^{n} w_i \|y_i - y\| \quad (2)$$

where $\|\cdot\|$ denotes the Euclidean norm. If all the weights are equal, i.e. $w_i = 1/n$, m_n becomes the geometric median (Chaouch and Goga, 2012; Chaudhuri, 1996; Small, 1990). When observations are not collinear, e.g. they lie in two or more dimensions, the (weighted) geometric median always exists and is unique (Milasevic and Ducharme, 1987). The robustness properties of the weighted geometric median differ from those of the geometric median (Nevalainen et al., 2007), which is unaffected by outlying values if their proportion remains under the breakdown point corresponding to half of the observations (Lopuhaa and Rousseeuw, 1991; Oja, 2013). In particular, the robustness of the estimator is influenced mostly by the weights assigned to invalid observations, e.g. contaminated by clouds, as it depends on the smallest set of observations whose weights sum up to at least half of all weights (Nevalainen et al., 2007). If only two clear observations are available, the weighted geometric median corresponds to the observation with the highest weight, providing no resistance to potential invalid values. As mountainous areas are characterised by frequent cloud and snow cover, the number of clear observations during certain growing seasons can be equal to two, so an adaptive time window for selecting more clear observations can mitigate data scarcity. During the compositing process, the width of the time window iteratively widened up to 20 days for each side until the number of clear observations for a given pixel location reached a minimum of three. We computed the weighted geometric median using Weiszfeld's iterative algorithm (Vardi and Zhang, 2000; Weiszfeld, 1937) implemented in the R (R Core Team, 2021) package "Gmedian" (Cardot, 2020), which uses efficient linear algebra libraries based on C++ language at its core functions.

3.2.8 Weighting system

Our pixel-based weighting system prioritised clear observations acquired during the greenup phase of the growing season and close to the date of peak while it penalised those lying nearby clouds or cloud shadows. Hence, the total weight w_i of the i-th observation was the sum of a phenology-based weight (w_p) with a distance-based weight (w_d), and each of them assumed values in the interval [0, 1]. We computed w_p through long-term land surface phenology (LSP) metrics representing the DOY at which transitions between phenological phases typically occur at a given location. Long-term LSP metrics allowed us to overcome two major limitations related to annual data. First, post-fire LSP metrics likely deviated from pre-fire ones due to changes in vegetation cover. Second, persistent snow and cloud cover occurring in mountainous areas during certain years prevent the computation of w_p on a yearly basis. We derived long-term LSP metrics from the Moderate Resolution Imaging Spectroradiometer (MODIS) Collection 6 Land Cover Dynamics Product (MCD12Q2) (Friedl et al., 2019). The MCD12Q2 product is available at 500 m spatial resolution from 2001 until 2017 and it is based on the 2-band Enhanced Vegetation Index (EVI2). Specifically, we computed the pixel-wise geometric median throughout the 17-year time series of Maturity (p_1), Peak (p_2) and Senescence (p_3) metrics. These correspond to the dates when EVI2 first crosses 90% of its amplitude, reaches its amplitude and last crosses 90% of its amplitude, respectively. The robustness of the geometric median limited the influence of ephemeral changes for the considered time interval induced by land-use/land-cover or annual climate anomalies. We discarded pixels flagged as poor quality retrievals in the "QA_Detailed" layer of the MCD12Q2 product to limit the proportion of contaminated data. To cope with the different spatial resolutions of the MCD12Q2 product and Sentinel-2 data, we first resampled LSP metrics to 20 m using the nearest neighbour method, i.e. we divided MODIS pixels into sub-pixels matching the grid and resolution of Sentinel-2 data. We then applied a Gaussian filter with a kernel having sigma equal to 250 m and a width

corresponding to one kilometre to eliminate the edges of the 500 m pixels while retaining the effects of local climate variability associated with topography on LSP metrics. Following Frantz et al. (2017), we derived w_p for a given pixel location by adapting an asymmetrical Gaussian curve to each triplet of LSP metrics (p_1, p_2 and p_3) (Figure 3.3). This procedure involved first computing the parameters σ_l and σ_r that determine the width of the curve at each tail:

$$\sigma_l = \frac{(p_2 - p_1)}{2}, \quad \sigma_r = \frac{(p_3 - p_2)}{2}. \tag{3}$$

We then computed w_p by evaluating the Gaussian function at the DOY corresponding to the acquisition date of the i-th observation (parameter D_i in equation 4):

$$w_p = \begin{cases} \exp\left(-c\left(\frac{(D_i - p_2)}{\sigma_l}\right)^2\right), D_i < p_2, \\ \exp\left(-c\left(\frac{(D_i - p_2)}{\sigma_r}\right)^2\right), D_i \geq p_2. \end{cases} \tag{4}$$

The parameter c in equation 4 further controlled the width of the Gaussian curve and we set it to 0.2 such that w_p is equal to 0.45 at p_1 and p_3 (Figure 3.3).

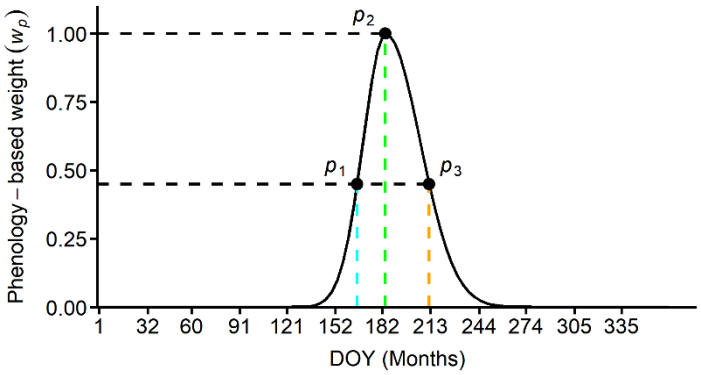

Figure 3.3. Example of the asymmetrical Gaussian curve used to compute the phenology-based weight (w_p). Long-term LSP metrics p_1, p_2 and p_3 correspond to Day-Of-Year (DOY) 166, 184 and 212, respectively. DOYs in the x-axis correspond to the beginning of each month in a non-leap year.

The distance-based weight, w_d, was aimed at reducing the influence of potential invalid reflectance values lying close to detected clouds or cloud shadows. Moreover, it limited patchiness in reflectance composites caused by the edges resulting from the removal of invalid pixels in Sentinel-2 images. This was particularly relevant when a low number of clear observations was available for a given pixel location. We computed w_d through a sigmoid function previously employed as a scoring function for evaluating the distance to clouds in several best pixel selection algorithms (Frantz et al., 2017; Griffiths et al., 2019, 2013):

$$w_d = \frac{1}{\left(1+\exp\left(-\frac{10}{ED_{max}}\cdot\left(ED_i-\frac{ED_{max}}{2}\right)\right)\right)}, \quad (5)$$

where ED_{max} is the maximum Euclidean distance to invalid pixels at which w_d can assume values lower than one and ED_i is the Euclidean distance of the i-th observation (Figure 3.4). Our experiments showed that a distance of 200 m, equivalent to 10 Sentinel-2 pixels, was adequate to effectively reduce patchiness.

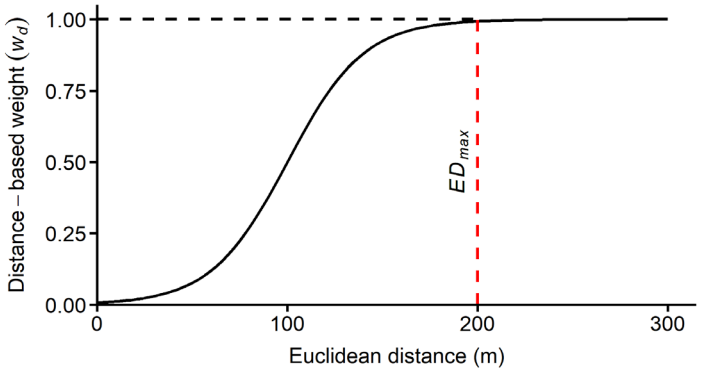

Figure 3.4. The sigmoid curve used to compute the distance-based weight (w_d). The red dashed line indicates the optimal Euclidean distance (ED) to clouds and cloud shadows used in this study.

Finally, we normalised the weights, $w_1,\ldots, w_n$, computed for all the observations available at each pixel location using the softmax function, previously employed with the weighted geometric median by Roberts et al. (2019), and defined as:

$$w_i = \frac{\exp(w_i)}{\sum_{j=1}^{n}\exp(w_j)}, i = 1, \ldots, n. \quad (6)$$

The softmax transformation converts each component of a vector of real numbers into values comprised in the interval [0, 1] that sum to one (Bishop, 2006). Therefore, all the transformed weights can be interpreted as probabilities proportional to the exponentials of the unnormalised weights. This transformation increased the contrast in importance between the best and worst observation.

3.2.9 Evaluation of long-term LSP metrics and radiometric consistency of reflectance composites

Elevation emerged as a critical driver in mountainous areas controlling long-term LSP metrics derived either from MODIS (Hwang et al., 2011; Xie et al., 2017) or Landsat (Elmore et al., 2012) data. Hence, we evaluated spatial patterns of our long-term LSP metrics within the burnt areas through a correlation analysis with elevation using the Pearson correlation coefficient. We obtained elevation data at 20 m spatial resolution by averaging values of the digital terrain model available for the Piedmont Region at 5 m spatial resolution.

We assessed radiometric consistency in time of reflectance composites by evaluating the symmetrical linear relationship between pre- and post-fire values at each MSI 20 m band and the derived NBR values using the reduced major axis (RMA) regression method (Roy et al., 2016; Smith, 2009). The RMA regression is adopted when both dependent and independent variables contain measurement errors, as in the case of surface reflectance values from satellite imagery. The similarity between the symmetrical linear relationship obtained with NBR values computed either with paired images or reflectance composites allowed us to assess whether the weighted geometric median preserved the spectral relationships between the MSI bands B8A and B12. We performed these evaluations on a set of one million pixels randomly selected outside the fire perimeters within a maximum distance of three kilometres. We quantified differences between pre- and post-fire reflectance and NBR values using the root mean square error (RMSE). We assessed the significance of the linear relationships through the *p*-value associated with the F-test performed with

ordinary least squares (OLS) fits, using pre-fire values as the independent variable and post-fire values as the dependent variable.

3.2.10 Classification and validation of burn severity maps

Following the nonlinear regression models proposed by different authors (Miller et al., 2009; Miller and Thode, 2007; Parks et al., 2014), we predicted thresholds of each bi-temporal index that discriminated between field severity categories (unchanged to low, moderate and high) through the inversion of the following equation:

$$y = a + b \cdot \exp(CBI \cdot c) \quad (7)$$

where *y* corresponds to values of either dNBR, RdNBR or RBR.

CBI plots for some burnt areas were either limited in the total amount or the range of values, so we used all the plots (n = 251) to build a combined regression model for each bi-temporal index. We note that vegetation characteristics varied among plots due to the presence of stands dominated by either conifers or broadleaves. We assessed the predictive performance of the regression models by averaging values of the coefficient of determination (R^2) and RMSE obtained from 5-fold cross-validation repeated 1000 times. We sampled values of the three bi-temporal indices at each CBI plot location without employing any data interpolation method, e.g. bilinear interpolation (Cansler and McKenzie, 2012; Parks et al., 2014), as this approach did not improve the predictive performance of the regression models.

Using CBI values as reference, we built an error matrix by pooling reference and classification data of all the burnt areas. We then computed classification accuracy (producer's, user's and overall accuracy) and Cohen's Kappa statistic. Lastly, we performed the exact McNemar test implemented in the R package "exact2x2" (Fay, 2010) to evaluate whether differences in overall classification accuracy between burn severity maps produced using paired images or reflectance composites were statistically significant.

3.3 Results

3.3.1 Reflectance composites

The number of pre- and post-fire clear observations available at the pixel level within the compositing period (20 May – 10 September) varied considerably inside each burnt area, between burnt areas and according to the acquisition year (Figure 3.5). Clear observations available at the majority of pixel locations were more than three in the pre- and post-fire compositing period while cloud-free images were fewer than three for some burnt areas (Figure S3.1). Sentinel-2 data was generally more abundant in 2018 than 2017. The overlapping zone between tiles 32TLR and 32TLQ greatly increased the number of clear observations at burnt area 7.

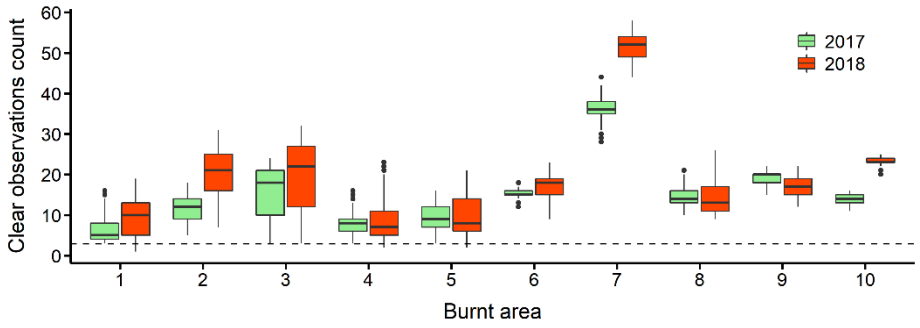

Figure 3.5. Boxplots of Sentinel-2 clear observations available at each pixel location in the pre- and post-fire compositing period of 2017 and 2018, respectively. The dashed line indicates the level corresponding to three observations. Numbers in the x-axis refer to each burnt area, as indicated in Table 3.1.

Spatial patterns of the long-term Maturity (p_1) and Peak (p_2) were strongly and positively correlated with local variations of elevation, as highlighted by the Pearson correlation coefficient that varied across the burnt areas from 0.79 to 0.97 for p_1 and from 0.66 to 0.95 for p_2 (Table S3.4). Conversely, the association

between long-term senescence (p_3) and elevation was generally lower compared to p_1 and p_2 and varied considerably according to the burnt area (Table S3.4).

Reflectance composites exhibited radiometric consistency in space as values between neighbouring pixels were similar, though they were computed using a different number of observations (Figure 3.6). Radiometric consistency in time was highlighted by similar reflectance values between pre- and post-fire unburnt pixels (Figure 3.6, Figure 3.7). The RMA regression lines between pairs of unburned synthetic reflectance values were close to the 1:1 line for all the MSI bands acquired at 20 m and R^2 values associated with the OLS fit were moderate to high (0.69 – 0.84). RMSE ranged from 0.014 (B5) to 0.045 (B7) and the OLS regression was always highly significant (p <0.001) (Figure 3.7). Synthetic reflectance for MSI bands in the SWIR wavelengths (B11 and B12) was higher in 2017 (x-axis) than in 2018 (y-axis), as highlighted by the slope of the RMA regression line (Figure 3.7e-f).

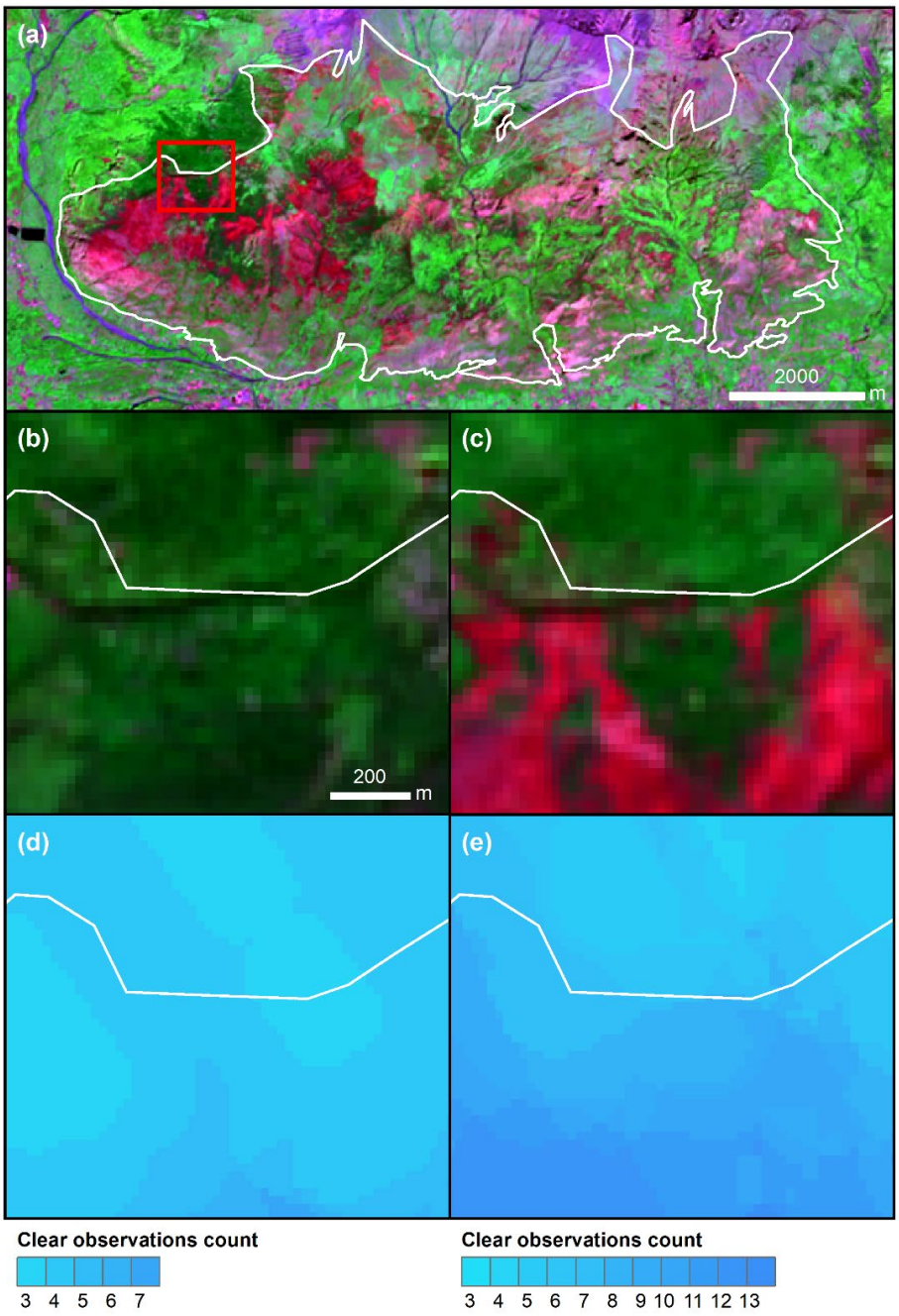

Figure 3.6. False colour RGB image of burnt area 1 from a combination of MSI bands (R = B12, G = B8A, B = B5) obtained using post-fire reflectance composite (**a**). False colour RGB image subsets of pre-fire (**b**) and post-fire (**c**) reflectance

composites are located as indicated by the extent in panel (**a**). Panels (**d**) and (**e**) show the number of clear observations used to produce pre- and post-fire reflectance composites, respectively. The white line represents the official fire perimeter.

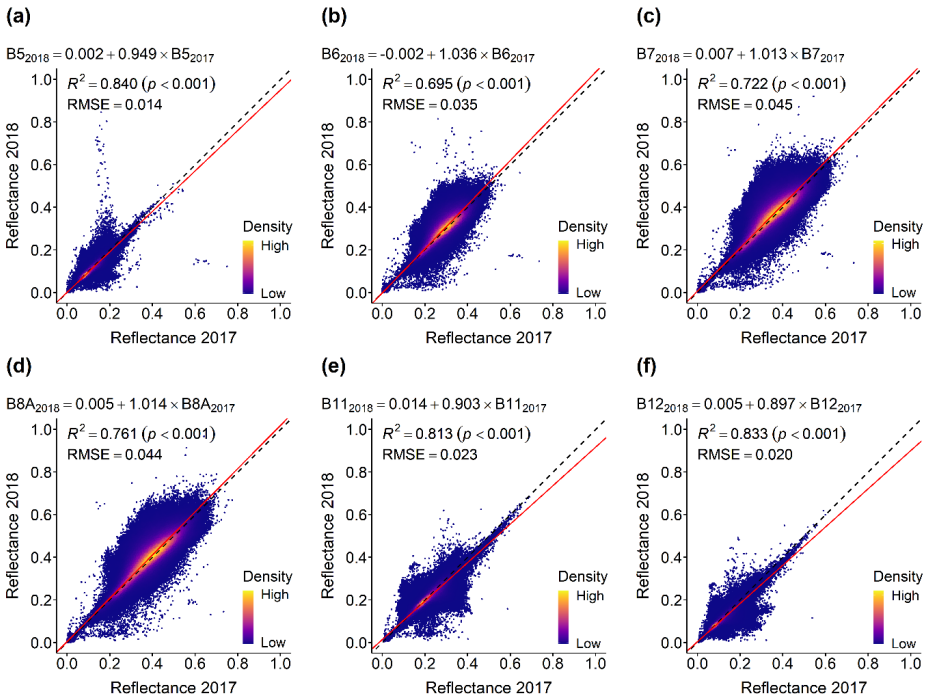

Figure 3.7. Band-wise scatter plots between pre-fire (x-axis) and post-fire (y-axis) reflectance composites. Values were randomly sampled outside fire perimeters (n = 1000000). The black dashed line represents the 1:1 line, and the solid red line corresponds to the RMA regression line. The coefficient of determination (R2) and *p*-value are derived from the OLS regression. Synthetic reflectance values of each MSI band acquired at 20 m are displayed: (**a**) B5, (**b**) B6, (**c**) B7, (**d**) B8A, (**e**) B11, (**f**) B12.

The weighted geometric median preserved the spectral relationships across MSI bands, as displayed by pre- and post-fire NBR values of unburnt pixels (Figure 3.8b) and synthetic reflectance values of burnt pixels (Figure 3.9). In particular, the RMA linear regression between pre- and post-fire NBR derived from

reflectance composites was very similar to that obtained with paired images (Figure 3.8). Pre-fire synthetic reflectance values for MSI bands B6, B7 and B8A were generally higher than most of those assumed by clear observations (Figure 3.9).

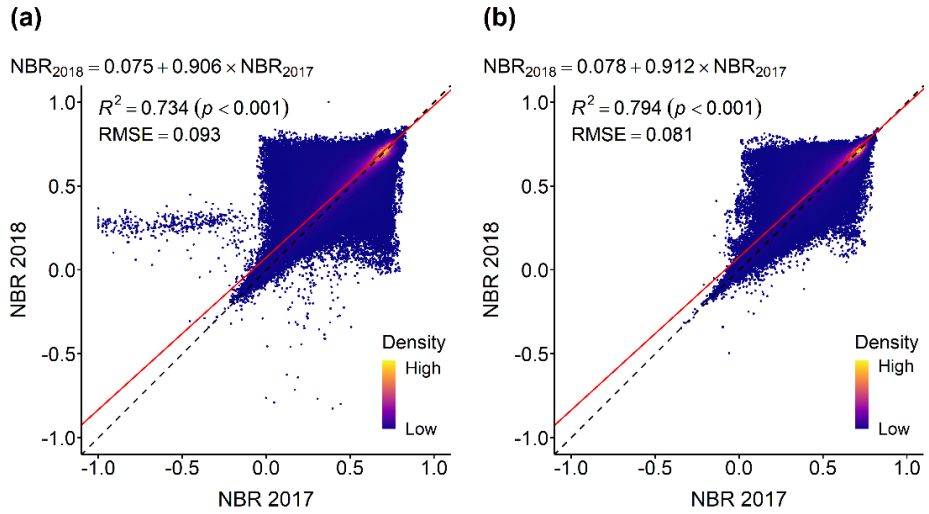

Figure 3.8. Scatter plots of pre-fire (x-axis) and post-fire (y-axis) NBR values randomly sampled outside the fire perimeters (n = 1000000). NBR was computed using either (**a**) paired images or (**b**) reflectance composites. The dashed black line is the 1:1 line, while the solid red line represents the RMA regression line. The coefficient of determination (R^2) and p-value are derived from the OLS regression.

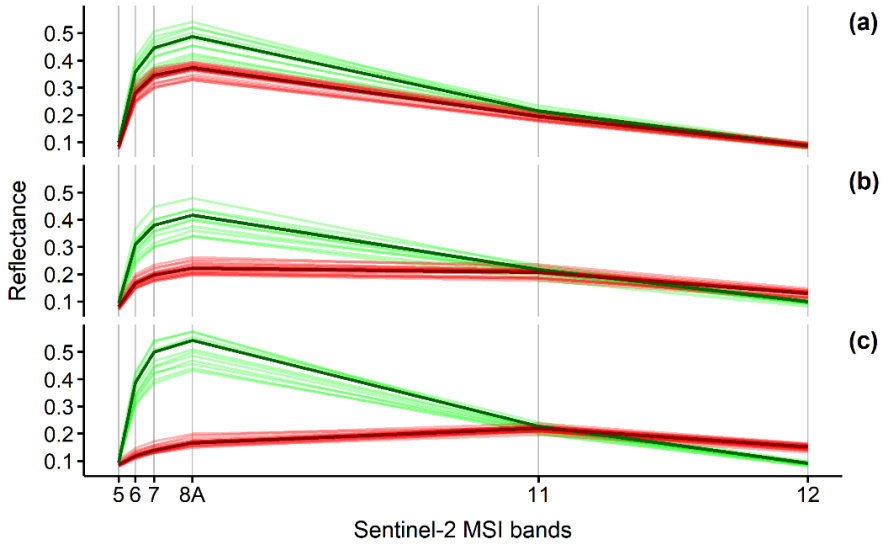

Figure 3.9. Pre-fire (green) and post-fire (red) surface reflectance values of three pixels in the burnt area 2 for each of the MSI bands acquired at 20 m (B5, B6, B7, B8A, B11, B12). Each pixel was located within a different burn severity category: (**a**) unchanged to low, (**b**) moderate, and (**c**) high. Light green and light red lines represent pre- and post-fire reflectance values of Sentinel-2 images acquired from 20 May to 10 September, whereas synthetic reflectance values are displayed in dark colours.

3.3.2 Regression models

The average R^2 from the repeated 5-fold cross-validation procedure highlighted a slightly higher predictive performance of nonlinear regression models built with bi-temporal indices derived from reflectance composites than those computed with paired images (Table 3.3). However, differences in R^2 were limited ($\leq$0.008) for all bi-temporal indices. Considering the same bi-temporal index, the average RMSE was always higher for reflectance composites compared to paired images (Table 3.3). The calibration of bi-temporal indices with the dNBR offset provided a minor increase in the predictive performance of the regression models (Table 3.3). Regression models built using the complete set of CBI plots and uncalibrated bi-temporal indices are displayed in Figure 3.10. Predicted

thresholds of bi-temporal indices discriminating between burn severity categories were higher using reflectance composites than paired images (Table S3.5).

Table 3.3. Average values of the coefficient of determination (R^2) and RMSE obtained from a repeated 5-fold cross-validation. We built regression models between bi-temporal indices (dNBR, RdNBR and RBR) computed using either paired images or reflectance composites and CBI. We either calibrated or not bi-temporal indices through the dNBR offset.

Bi-temporal index	**Measure**	**Paired images**		**Reflectance composites**	
		Uncalibrated	**Calibrated**	**Uncalibrated**	**Calibrated**
dNBR	R^2	0.865	0.869	0.871	0.873
RdNBR		0.874	0.878	0.880	0.882
RBR		0.872	0.877	0.878	0.879
dNBR	**RMSE**	94.8	93.2	99.3	98.7
RdNBR		112.5	110.6	116.8	116.3
RBR		55.3	54.4	57.6	57.3

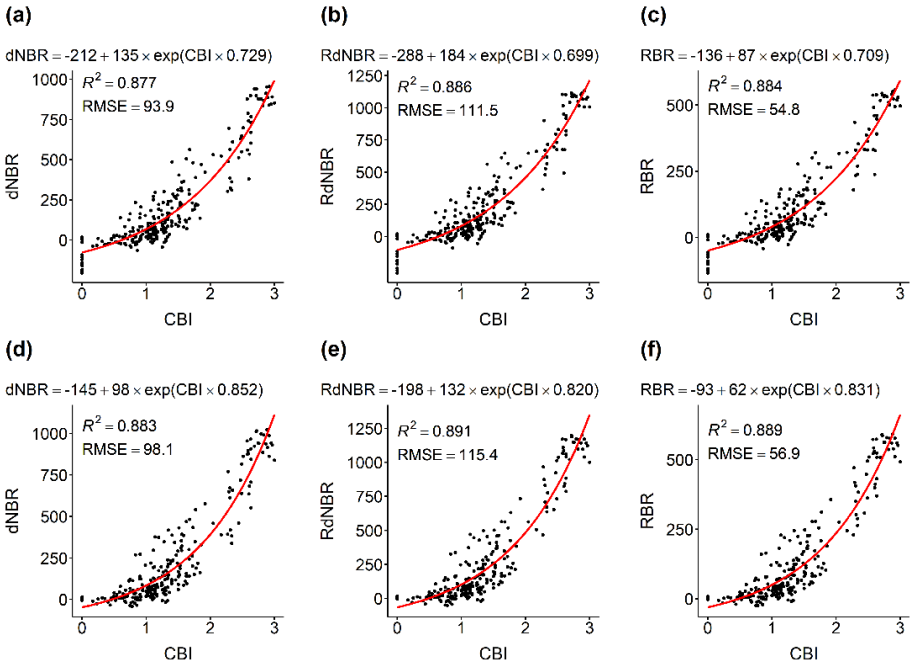

Figure 3.10. Nonlinear regression models built using CBI field-data (x-axis, n = 251) and uncalibrated bi-temporal indices (y-axis) derived either from paired images (**a-c**) or reflectance composites (**d-f**).

3.3.3 Burn severity maps

Burn severity maps achieved overall accuracies ranging from 76.9% to 83.7% (Kappa between 0.61 and 0.72) and these were consistently higher for reflectance composites compared to paired images (Table 3.4). Paired images performed better with calibrated bi-temporal indices and among them, RdNBR provided the highest overall classification accuracy (80.5%, Kappa 0.67). Conversely, reflectance composites attained the highest overall classification accuracy (83.7%, Kappa 0.72) with uncalibrated RdNBR (Table 3.4). Among burn severity categories, the moderate one achieved the lowest user's and producer's accuracy (Table 3.4).

Table 3.4. Accuracy of burn severity maps obtained using different bi-temporal indices (either uncalibrated or calibrated with the dNBR offset) derived from

paired images or reflectance composites. User's Accuracy (UA), Producer's Accuracy (PA) and Overall Accuracy (OA) are expressed as percentages. Cohen's Kappa (K) ranges from -1 to 1.

Bi-temporal index		Burn severity category	Paired images				Reflectance composites			
			UA	PA	OA	K	UA	PA	OA	K
Uncalibrated	dNBR	Unchanged to low	80.1	85.6	76.9	0.61	82.1	90.2	81.7	0.69
		Moderate	64.3	57.7			73.5	64.1		
		High	87.5	85.4			94.7	87.8		
	RdNBR	Unchanged to low	80.9	86.4	78.5	0.64	81.8	91.7	83.7	0.72
		Moderate	67.1	60.3			79.4	64.1		
		High	90	87.8			97.5	95.1		
	RBR	Unchanged to low	80.9	86.4	78.1	0.63	81.8	91.7	82.5	0.7
		Moderate	66.2	60.3			75.8	64.1		
		High	89.7	85.4			97.3	87.8		
Calibrated	dNBR	Unchanged to low	81.1	87.9	78.9	0.64	80.8	89.4	80.5	0.67
		Moderate	68.1	60.3			71.6	61.5		
		High	89.7	85.4			94.7	87.8		
	RdNBR	Unchanged to low	81.9	89.4	80.5	0.67	80.3	89.4	81.7	0.69
		Moderate	71.6	61.5			75	61.5		
		High	90	87.8			97.5	95.1		
	RBR	Unchanged to low	81.8	88.6	79.7	0.65	79.7	89.4	80.5	0.67
		Moderate	69.6	61.5			72.3	60.3		
		High	89.7	85.4			97.4	90.2		

The calibration of bi-temporal indices through the dNBR offset improved the overall accuracy of burn severity maps derived from paired images by 2% (RdNBR and dNBR) and 0.8% (RBR). On the contrary, the calibration of bi-temporal indices derived from reflectance composites reduced the overall

accuracy by 1.2% (dNBR) and 2% (RdNBR and RBR). Notably, changes in producer's and user's accuracy induced by calibration were mostly limited to the unchanged to low and moderate categories.

Burn severity maps obtained from uncalibrated bi-temporal indices highlighted significant differences in overall classification accuracy (p <0.05) between paired images and reflectance composites (Table 3.5), particularly for the RdNBR (p <0.01). Differences in overall classification accuracy of burn severity maps from calibrated bi-temporal indices produced using paired images or reflectance composites were not statistically significant (Table 3.5).

Table 3.5. Results from the exact McNemar test relative to differences in overall classification accuracy of burn severity maps derived from paired images or reflectance composites. *P*-value and 95% confidence interval (CI) refer to the significance and magnitude of difference in overall classification accuracy, respectively.

Bi-temporal index		***p***	**95% CI**
Uncalibrated	**dNBR**	0.023	1.141 – 9.232
	RdNBR	0.007	1.386 – 17.361
	RBR	0.027	1.120 – 11.169
Calibrated	**dNBR**	0.503	0.564 – 4.230
	RdNBR	0.629	0.491 – 4.422
	RBR	0.814	0.444 – 3.645

We compared burn severity maps obtained with calibrated RdNBR from paired images and uncalibrated RdNBR from reflectance composites. Visual inspection of the spatial patterns of burn severity patches revealed good agreement between maps obtained using the two approaches above (Figure 3.11), though differences in the extent of burn severity categories were noticeable (Figure 3.12). To account for missing pixels in burn severity maps derived from paired images (Figure 3.11a), we removed these pixels also in maps obtained with reflectance

composites. In some areas, the extent of the moderate and high burn severity categories was greater in maps derived from paired images compared to those obtained with reflectance composites by a total of 198.6 ha (6.3%) and 47.5 ha (11.4%), respectively. Conversely, where the extent of the moderate and high severity categories was lower in maps obtained with paired images than in those produced with reflectance composites, differences amounted to 290.9 ha (-9.2%) and 125.6 ha (-30.1%). Overall, the extent of the moderate and high severity categories was lower in burn severity maps obtained with paired images compared to those derived with reflectance composites by 93.2 ha (-2.9%) and 78.1 ha (-18.7%), respectively.

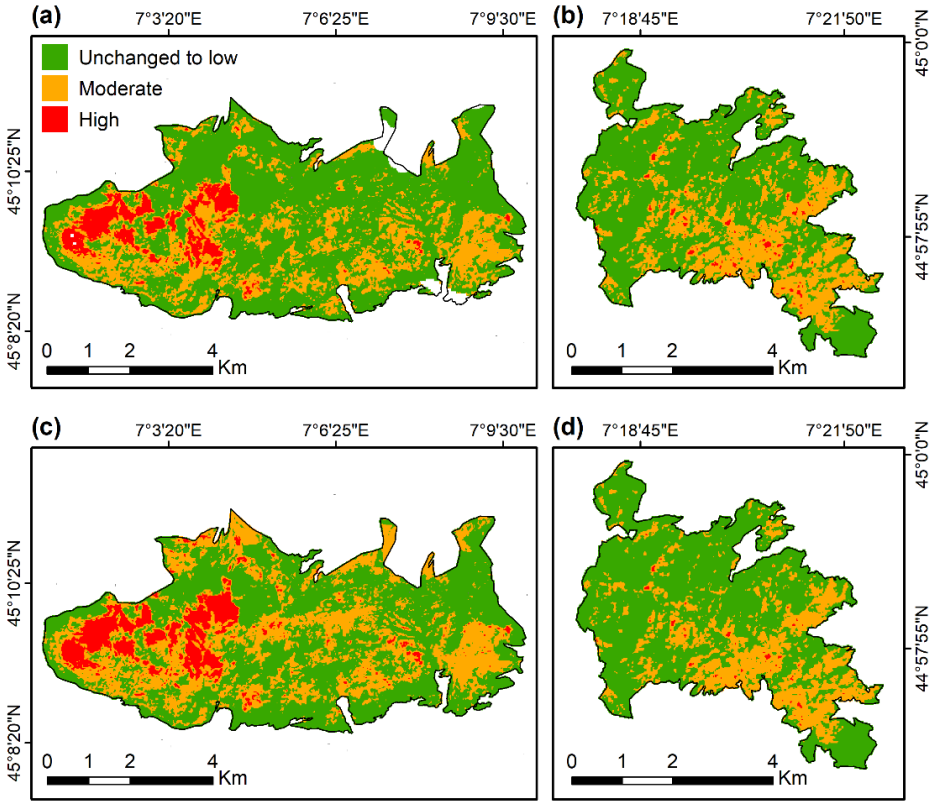

Figure 3.11. Burn severity maps of area 1 (**a**, **c**) and area 2 (**b, d**) obtained with calibrated RdNBR computed using paired images (**a**, **b**) or uncalibrated RdNBR

from reflectance composites (**c**, **d**). The black line indicates the official fire perimeters.

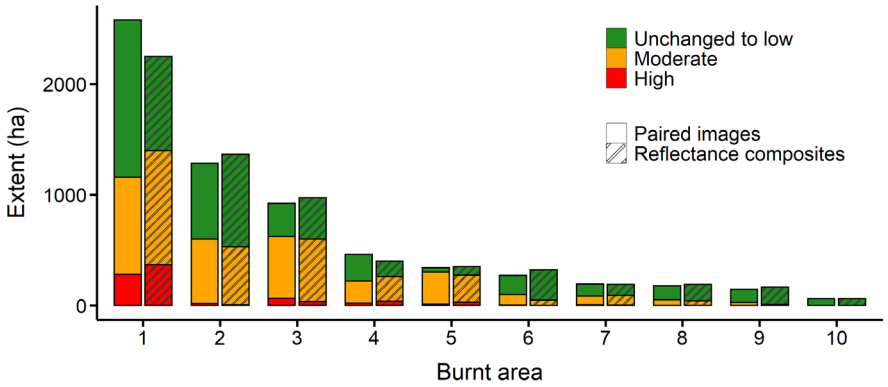

Figure 3.12. Extent of burn severity categories (unchanged to low, moderate and high) in each burnt area derived from maps obtained with calibrated RdNBR computed using paired images or uncalibrated RdNBR from reflectance composites.

3.4 Discussion

3.4.1 Reflectance composites

The 5-days revisit time offered by the Sentinel-2 mission since both S2A and S2B satellites have been in orbit, provided a considerable amount of clear observations within the time window, i.e. more than 10 observations for many pixel locations. The lower number of clear observations available in the 2017 growing season compared to that of 2018 (Figure 3.5, Figure S3.1) was caused by the availability of S2B images only since July 2017, after the completion of the ramp-up phase (Sudmanns et al., 2019).

Relying on long-term LSP metrics, our weighting system ignores inter-annual differences in plant phenology arising from different amounts of precipitation over the years, as in the case of the severe summer drought in 2017 (Rita et al., 2020). Divergent plant phenology between years has the potential to generate non-fire induced spectral changes (Veraverbeke et al., 2010a; Verbyla et al.,

2008). Reflectance composites showed greater overall stability of NBR values across the growing seasons of 2017 and 2018 in unburnt pixels compared to paired images (Figure 3.8). This suggests a limited impact of non-fire induced inter-annual variations on NBR values derived from reflectance composites. However, non-fire induced inter-annual differences in synthetic spectral values were noticeable in the SWIR wavelengths (MSI B11 and B12) and limited in the NIR narrow band (MSI B8A) (Figure 3.7d-f). The slope of the RMA fit lower than one in B11 and B12 is likely associated with low moisture conditions in plants and substrates during the pre-fire growing season of 2017 as a consequence of the severe drought. Pre-fire moisture content has been identified as the most critical variable for improving regression models between dNBR and CBI data (Soverel et al., 2011), suggesting its relevance in determining non-fire induced inter-annual changes at the spectral level.

Linear and positive correlation between spatial patterns of long-term LSP metrics relative to the greenup phase of the growing season and patterns of topography (Table S3.4) has been observed in mountainous landscapes. This is associated with the influence of elevation on temperature and snow cover, which are both dominant factors controlling spring onset at high altitudes (Elmore et al., 2012; Hwang et al., 2011; Xie et al., 2017). Limiting the influence of ephemeral land-cover changes and climate anomalies on the phenology-based weight improved the suitability of our weighting system for producing consistent reflectance composites throughout the years. Moreover, the coarse spatial scale at which long-term LSP metrics are implemented in the weighting system prevented the presence of artefacts in reflectance composites due to spatial discontinuities in LSP metrics associated with transitions between different land covers.

Spatial heterogeneity associated with the number of clear observations had a negligible influence on the radiometric consistency in space of reflectance composites (Figure 3.6). The weighted geometric median produced synthetic reflectance values that were statistically representative of the compositing period and preserved spectral relationships across bands (Roberts et al., 2019). Because of the two properties above, the (weighted) geometric median is defined as a

central and global indicator of the data distribution (Chaouch and Goga, 2012). Hence, synthetic reflectance values obtained with the weighted geometric median are suitable for the computation of spectral indices (Roberts et al., 2019, 2017). For missed invalid pixels that can occur using detection algorithms for clouds and cloud shadows currently available for Sentinel-2 imagery (Tarrio et al., 2020), the robustness of the weighted geometric median is considerably superior to that of the weighted mean (Roberts et al., 2019).

3.4.2 Burn severity mapping

When mapping burn severity is the primary aim, the exploitation of the weighted geometric median integrating long-term LSP metrics offers a threefold improvement over the usage of paired images. First, it provides reflectance data for the whole burnt area with no or minimal presence of outlying values. Second, it generates reflectance values representative of the optimal seasonal timing at every pixel location. Third, spectral matching between pre- and post-fire conditions is promoted by the weighting system anchored to fixed DOYs corresponding to the long-term LSP metrics.

Reflectance composites marginally increased the predictive performance of nonlinear regression models compared to paired images (Table 3.3). Results obtained with NBR mean composites were either similar (Parks et al., 2018) or opposite (Whitman et al., 2020) to ours. The exponential growth function correctly approximated the nonlinear asymptotic relationship between CBI and bi-temporal indices (Lentile et al., 2009) since values of these latter are not constrained to complete vegetation mortality (Miller et al., 2009). Mixing CBI plots dominated by either coniferous or broadleaved species did not prevent nonlinear regression models from achieving high predictive performance (R^2 >0.85). Moreover, the extensive preprocessing of Sentinel-2 images and the thoroughly collected CBI data likely enhanced the relationship between CBI data and bi-temporal indices.

The overall classification accuracy of burn severity maps derived from paired images was higher (approximately 6% – 7% differences) compared to similar studies using Landsat (Parks et al., 2018) or Sentinel-2 imagery (Mallinis et al., 2017). Reflectance composites outperformed NBR mean composites derived from Landsat imagery (Parks et al., 2018), increasing the overall accuracy of burn severity maps by between 8% – 10% depending on the bi-temporal index. User's and producer's accuracies of the high burn severity category (>95%) provided by uncalibrated RdNBR derived from reflectance composites were comparable to results obtained with the random forest classifier for the crown consumption class in fire severity maps (Collins et al., 2018; Gibson et al., 2020). Improvements in the overall classification accuracy offered by reflectance composites over paired images were maximal and statistically significant for uncalibrated bi-temporal indices (Table 3.5). Similarly, Parks et al. (2018) obtained significant improvements in the overall classification accuracy using uncalibrated RdNBR derived from NBR mean composites compared to paired images.

Our burn severity maps discriminated the moderate severity with a relatively low accuracy compared to the other categories (Table 3.4). Similar results have previously been reported when inferring burn severity from remotely sensed multispectral data (Miller et al., 2009; Soverel et al., 2010). In non-stand replacing fires, the assessment of mixed fire effects mostly impacting the understory vegetation through multispectral data is challenging as healthy and relatively dense tree canopy cover can mask fire effects (De Santis and Chuvieco, 2007). Recently, Yin et al. (2020) integrated tree canopy cover information in the parameterisation and backward inversion of a radiative transfer model to limit the underestimation of the moderate and high burn severity.

The calibration of bi-temporal indices with the dNBR offset reduced the classification accuracy of burn severity maps derived from reflectance composites (Table 3.4). In fact, the radiometric consistency in time between pre- and post-fire reflectance composites likely limited the utility of the dNBR offset. Drawbacks of using the dNBR offset are related to the selection of an appropriate set of unburnt pixels, as they should be representative of the pre-fire vegetation

in the burnt area (Parks et al., 2018; Picotte et al., 2020). Therefore, deriving the dNBR offset for large burnt areas characterised by a heterogeneous pre-fire vegetation can be subjective and prone to error. Our compositing method can improve the operational usage of bi-temporal indices by eliminating the need for further calibration.

The increase in the accuracy of burn severity maps provided by reflectance composites over paired images appeared to be related to higher thresholds of bi-temporal indices discriminating between burn severity categories (Table S3.5). In fact, a large range of values within each burn severity category favoured the discrimination capability of bi-temporal indices (Lentile et al., 2009). The priority given to observations close to the long-term peak of phenology enhanced the spectral contrast between healthy (pre-fire) and burnt vegetation, e.g. in the NIR region (Figure 3.9). A steady decrease in canopy greenness has been observed in deciduous forests during the greendown phase and has been implemented when modelling phenological transitions in forests using optical remote sensing data (Elmore et al., 2012; Klosterman et al., 2014; Melaas et al., 2013). In particular, the decline of reflectance in the near-infrared wavelengths throughout the summer months in deciduous forests (Jenkins et al., 2007) likely affects the temporal pattern of NBR mostly during the pre-fire growing season. Conversely, during the first post-fire growing season, the detection of fire induced changes can be heavily influenced by regeneration processes, particularly in quickly recovering ecosystems such as those of the Mediterranean basin (Veraverbeke et al., 2010a). In our burnt areas, the recovery of the herbaceous layer in wood-pastures and the abundant sprouting from stumps in broadleaved forests increasingly reduced the spectral contrast between pre- and post-fire conditions over time.

The optimisation of the seasonal timing in reflectance composites also increased the overall extent of the moderate and high burn severity categories (Figure 3.12). An underestimation of burn severity likely occurred when using paired images acquired during late summer (Figure S3.1) due to the weak contrast between pre- and post-fire spectral conditions, as observed by other authors (Chen et al., 2020;

Key, 2006; Veraverbeke et al., 2010a). On the contrary, the slight decrease in the extent of the moderate and high burn severity, e.g. in burnt area 2 and 3, when using reflectance composites was probably caused by higher thresholds of bi-temporal indices than those derived from paired images (Table S3.5).

Further investigation is needed to determine the applicability of our approach in certain fire-prone ecosystems where fire severity is of primary interest due to rapid vegetation regrowth (Parker et al., 2015; Picotte and Robertson, 2011; Veraverbeke et al., 2010a). As fire severity is assessed within a few weeks following the fire (Key, 2006), reflectance composites should be produced using a relatively short compositing period which would benefit from multispectral data with a high temporal resolution. In this sense, the Harmonized Landsat Sentinel-2 (HLS) dataset (Claverie et al., 2018) provides medium-resolution multispectral data with a relatively high temporal resolution (up to 2-3 days).

Though bi-temporal indices are widely used for mapping burn severity (Morgan et al., 2014), they typically make use of only two or three spectral bands, e.g. NBR, NDVI and EVI. Other methods based on optical remote sensing data make use of all the spectral bands available and proved to be effective in burn severity estimation (Morgan et al., 2014; Yin et al., 2020). Machine learning classifiers, e.g. random forest (Collins et al., 2018; Gibson et al., 2020), radiative transfer models (Yin et al., 2020) and spectral mixture analysis (Quintano et al., 2017) are among those approaches that could benefit from exploiting the full spectral information provided by reflectance composites.

3.5 Conclusions

In this study, we presented a compositing approach that offers the possibility to overcome some of the major limitations hindering burn severity mapping through bi-temporal indices derived from multispectral data. We highlighted that temporal constraints in the selection of appropriate paired images can significantly affect burn severity maps. Our approach provides new opportunities for operational burn severity mapping in areas characterised by persistent cloud

cover, such as mountainous landscapes. Moreover, phenologically coherent reflectance composites provide a standardised approach for mapping burn severity and avoid further processing to mitigate spectral mismatches. Among the advantages the proposed compositing algorithm provides, there is also its transferability to other optical sensors and multi-sensor data, such as surface reflectance provided by the HLS dataset (Claverie et al., 2018). In the context of forest ecology and forest disturbances mapping, several change detection techniques and classification algorithms could benefit from the use of phenologically coherent reflectance composites, thus being of broad interest to forest managers and researchers.

Acknowledgments

This work was supported by the Regione Piemonte through the “Piano straordinario di interventi di ripristino in seguito agli incendi dell'autunno 2017” approved with the Delibera Giunta Regionale (D.G.R.) n. 29-8813 on 18 April 2019, and was partially funded by Fondazione Cassa di Risparmio di Torino through the project “Strumenti per la valutazione del rischio di degradazione del suolo e la gestione dei boschi piemontesi percorsi da incendio”. We thank Fabio Meloni, Giulia Mantero, Alessia Bono, Emanuele Sibona, Massimo Ventura and Nicolò Giordana for their support in field surveys. Moreover, we thank David Frantz for providing the Framework for Operational Radiometric Correction for Environmental monitoring (FORCE) software. We are grateful to three anonymous reviewers for contributing to improve the quality of the paper through their constructive comments and suggestions.

Data availability statement

Burn severity maps generated and analysed in the current study are available in the Figshare repository, https://doi.org/10.6084/m9.figshare.13720735.v2.

References

Arpa Piemonte, 2017. Rapporto tecnico sulla qualità dell'aria e sulle attività dell'agenzia a supporto dell'emergenza per gli incendi boschivi in Piemonte nel mese di ottobre 2017.

Barbero, R., Curt, T., Ganteaume, A., Maillé, E., Jappiot, M., Bellet, A., 2019. Simulating the effects of weather and climate on large wildfires in France. Nat. Hazards Earth Syst. Sci. 19, 441–454. https://doi.org/10.5194/nhess-19-441-2019

Bebi, P., Seidl, R., Motta, R., Fuhr, M., Firm, D., Krumm, F., Conedera, M., Ginzler, C., Wohlgemuth, T., Kulakowski, D., 2017. Changes of forest cover and disturbance regimes in the mountain forests of the Alps. For. Ecol. Manage. 388, 43–56. https://doi.org/10.1016/j.foreco.2016.10.028

Bedia, J., Herrera, S., Camia, A., Moreno, J.M., Gutiérrez, J.M., 2014. Forest fire danger projections in the Mediterranean using ENSEMBLES regional climate change scenarios. Clim. Change 122, 185–199. https://doi.org/10.1007/s10584-013-1005-z

Bishop, C., 2006. Pattern Recognition and Machine Learning, 1st ed. Springer-Verlag, New York.

Bo, M., Mercalli, L., Pognant, F., Cat Berro, D., Clerico, M., 2020. Urban air pollution, climate change and wildfires: The case study of an extended forest fire episode in northern Italy favoured by drought and warm weather conditions. Energy Reports 6, 781–786. https://doi.org/10.1016/j.egyr.2019.11.002

Brang, P., Schonenberger, W., Frehner, M., Schwitter, R., Thormann, J.-J., Wasser, B., 2006. Management of protection forests in the European Alps: An overview. For. Snow Landsc. Res. 80, 23–44.

Brimberg, J., 1995. The Fermat—Weber location problem revisited. Math. Program. 71, 71–76. https://doi.org/10.1007/BF01592245

Cane, D., Wastl, C., Barbarino, S., Renier, L.A., Schunk, C., Menzel, A., 2013. Projection of fire potential to future climate scenarios in the Alpine area:

Some methodological considerations. Clim. Change 119, 733–746. https://doi.org/10.1007/s10584-013-0775-7

Cansler, C.A., McKenzie, D., 2012. How robust are burn severity indices when applied in a new region? Evaluation of alternate field-based and remote-sensing methods. Remote Sens. 4, 456–483. https://doi.org/10.3390/rs4020456

Cardot, H., 2020. Gmedian: Geometric Median, k-Median Clustering and Robust Median PCA.

Chaouch, M., Goga, C., 2012. Using Complex Surveys to Estimate the L 1 - Median of a Functional Variable: Application to Electricity Load Curves. Int. Stat. Rev. 80, 40–59. https://doi.org/10.1111/j.1751-5823.2011.00172.x

Chaudhuri, P., 1996. On a Geometric Notion of Quantiles for Multivariate Data. J. Am. Stat. Assoc. 91, 862–872. https://doi.org/10.1080/01621459.1996.10476954

Chen, D., Loboda, T. V., Hall, J. V., 2020. A systematic evaluation of influence of image selection process on remote sensing-based burn severity indices in North American boreal forest and tundra ecosystems. ISPRS J. Photogramm. Remote Sens. 159, 63–77. https://doi.org/10.1016/j.isprsjprs.2019.11.011

Claverie, M., Ju, J., Masek, J.G., Dungan, J.L., Vermote, E.F., Roger, J.-C., Skakun, S. V., Justice, C., 2018. The Harmonized Landsat and Sentinel-2 surface reflectance data set. Remote Sens. Environ. 219, 145–161. https://doi.org/10.1016/j.rse.2018.09.002

Cohen, M.B., Lee, Y.T., Miller, G., Pachocki, J., Sidford, A., 2016. Geometric median in nearly linear time, in: Proceedings of the 48th Annual ACM SIGACT Symposium on Theory of Computing - STOC 2016. ACM Press, New York, New York, USA, pp. 9–21. https://doi.org/10.1145/2897518.2897647

Collins, L., Griffioen, P., Newell, G., Mellor, A., 2018. The utility of Random Forests for wildfire severity mapping. Remote Sens. Environ. 216, 374–384. https://doi.org/10.1016/j.rse.2018.07.005

Conedera, M., Krebs, P., Valese, E., Cocca, G., Schunk, C., Menzel, A., Vacik, H., Cane, D., Japelj, A., Muri, B., Ricotta, C., Oliveri, S., Pezzatti, G.B., 2018. Characterizing Alpine pyrogeography from fire statistics. Appl. Geogr. 98, 87–99. https://doi.org/10.1016/j.apgeog.2018.07.011

De Santis, A., Chuvieco, E., 2009. GeoCBI: A modified version of the Composite Burn Index for the initial assessment of the short-term burn severity from remotely sensed data. Remote Sens. Environ. 113, 554–562. https://doi.org/10.1016/j.rse.2008.10.011

De Santis, A., Chuvieco, E., 2007. Burn severity estimation from remotely sensed data: Performance of simulation versus empirical models. Remote Sens. Environ. 108, 422–435. https://doi.org/10.1016/j.rse.2006.11.022

Eidenshink, J., Schwind, B., Brewer, K., Zhu, Z., Quayle, B., Howard, S., 2007. A Project for Monitoring Trends in Burn Severity. Fire Ecol. 3, 3–21. https://doi.org/10.4996/fireecology.0301003

Elmore, A.J., Guinn, S.M., Minsley, B.J., Richardson, A.D., 2012. Landscape controls on the timing of spring , autumn , and growing season length in mid-Atlantic forests. Glob. Chang. Biol. 656–674. https://doi.org/10.1111/j.1365-2486.2011.02521.x

European Environmental Agency, 2018a. Copernicus Land Monitoring Service – Dominant Leaf Type 2015 [WWW Document]. URL https://land.copernicus.eu/pan-european/high-resolution-layers/forests/dominant-leaf-type/status-maps/2015 (accessed 6.10.20).

European Environmental Agency, 2018b. Copernicus Land Monitoring Service – Tree Cover Density 2015 [WWW Document]. URL https://land.copernicus.eu/pan-european/high-resolution-layers/forests/tree-cover-density/status-maps/2015 (accessed 6.10.20).

Fay, M.P., 2010. Two-sided exact tests and matching confidence intervals for discrete data. R J. 2, 53–58. https://doi.org/10.32614/rj-2010-008

Flood, N., 2013. Seasonal composite Landsat TM/ETM+ Images using the medoid (a multi-dimensional median). Remote Sens. 5, 6481–6500. https://doi.org/10.3390/rs5126481

Frantz, D., 2019. FORCE-Landsat + Sentinel-2 analysis ready data and beyond. Remote Sens. 11. https://doi.org/10.3390/rs11091124

Frantz, D., Haß, E., Uhl, A., Stoffels, J., Hill, J., 2018. Improvement of the Fmask algorithm for Sentinel-2 images: Separating clouds from bright surfaces based on parallax effects. Remote Sens. Environ. 215, 471–481. https://doi.org/10.1016/j.rse.2018.04.046

Frantz, D., Röder, A., Stellmes, M., Hill, J., 2017. Phenology-adaptive pixel-based compositing using optical earth observation imagery. Remote Sens. Environ. 190, 331–347. https://doi.org/10.1016/j.rse.2017.01.002

Frantz, D., Röder, A., Stellmes, M., Hill, J., 2016. An operational radiometric landsat preprocessing framework for large-area time series applications. IEEE Trans. Geosci. Remote Sens. 54, 3928–3943. https://doi.org/10.1109/TGRS.2016.2530856

French, N., Kasischke, E.S., Hall, R.J., Murphy, K.A., Verbyla, D.L., Hoy, E.E., Allen, J.L., French A, N.H.F., Kasischke, E.S., Hall, R.J., Murphy, K.A., Verbyla, D.L., Hoy, E.E., Allen, J.L., 2008. Using Landsat data to assess fire and burn severity in the North American boreal forest region: an overview and summary of results. Int. J. Wildl. Fire 17, 443–462. https://doi.org/10.1071/WF08007

Friedl, M., Gray, J., Sulla-Menashe, D., 2019. MCD12Q2 MODIS/Terra+ Aqua Land Cover Dynamics Yearly L3 Global 500m SIN Grid V006 [WWW Document]. NASA EOSDIS L. Process. DAAC; NASA Washington, DC, USA. https://doi.org/10.5067/MODIS/MCD12Q2.006

Furniss, T.J., Kane, V.R., Larson, A.J., Lutz, J.A., 2020. Detecting tree mortality with Landsat-derived spectral indices: Improving ecological accuracy by examining uncertainty. Remote Sens. Environ. 237, 111497. https://doi.org/10.1016/j.rse.2019.111497

García, M.J.L., Caselles, V., 1991. Mapping burns and natural reforestation using thematic Mapper data. Geocarto Int. 6, 31–37. https://doi.org/10.1080/10106049109354290

Gibson, R., Danaher, T., Hehir, W., Collins, L., 2020. A remote sensing approach

to mapping fire severity in south-eastern Australia using sentinel 2 and random forest. Remote Sens. Environ. 240, 111702. https://doi.org/10.1016/j.rse.2020.111702

Gobiet, A., Kotlarski, S., 2020. Future Climate Change in the European Alps. https://doi.org/10.1093/acrefore/9780190228620.013.767

Gobiet, A., Kotlarski, S., Beniston, M., Heinrich, G., Rajczak, J., Stoffel, M., 2014. 21st century climate change in the European Alps-A review. Sci. Total Environ. 493, 1138–1151. https://doi.org/10.1016/j.scitotenv.2013.07.050

Griffiths, P., Kuemmerle, T., Baumann, M., Radeloff, V.C., Abrudan, I. V., Lieskovsky, J., Munteanu, C., Ostapowicz, K., Hostert, P., Grif, P., Kuemmerle, T., Baumann, M., Radeloff, V.C., Abrudan, I. V., Lieskovsky, J., Munteanu, C., Ostapowicz, K., Hostert, P., 2014. Forest disturbances, forest recovery, and changes in forest types across the carpathian ecoregion from 1985 to 2010 based on landsat image composites. Remote Sens. Environ. 151, 72–88. https://doi.org/10.1016/j.rse.2013.04.022

Griffiths, P., Nendel, C., Hostert, P., 2019. Intra-annual reflectance composites from Sentinel-2 and Landsat for national-scale crop and land cover mapping. Remote Sens. Environ. 220, 135–151. https://doi.org/10.1016/J.RSE.2018.10.031

Griffiths, P., van der Linden, S., Kuemmerle, T., Hostert, P., 2013. A Pixel-Based Landsat Compositing Algorithm for Large Area Land Cover Mapping. Sel. Top. Appl. Earth Obs. Remote Sensing, IEEE J. 6, 2088–2101. https://doi.org/10.1109/JSTARS.2012.2228167

Gudmundsson, L., Seneviratne, S.I., 2016. Anthropogenic climate change affects meteorological drought risk in Europe. Environ. Res. Lett. 11. https://doi.org/10.1088/1748-9326/11/4/044005

Hijmans, R.J., 2020. raster: Geographic Data Analysis and Modeling.

Hwang, T., Song, C., Vose, J.M., Band, L.E., 2011. Topography-mediated controls on local vegetation phenology estimated from MODIS vegetation index. Landsc. Ecol. 26, 541–556. https://doi.org/10.1007/s10980-011-

9580-8

Jenkins, J.P., Richardson, A.D., Braswell, B.H., Ollinger, S. V., Hollinger, D.Y., Smith, M.L., 2007. Refining light-use efficiency calculations for a deciduous forest canopy using simultaneous tower-based carbon flux and radiometric measurements. Agric. For. Meteorol. 143, 64–79. https://doi.org/10.1016/j.agrformet.2006.11.008

Keeley, J.E., 2009. Fire intensity, fire severity and burn severity: A brief review and suggested usage. Int. J. Wildl. Fire 18, 116–126. https://doi.org/10.1071/WF07049

Kennedy, R.E., Yang, Z., Gorelick, N., Braaten, J., Cavalcante, L., Cohen, W.B., Healey, S., 2018. Implementation of the LandTrendr algorithm on Google Earth Engine. Remote Sens. 10, 1–10. https://doi.org/10.3390/rs10050691

Key, C.H., 2006. Ecological and Sampling Constraints on Defining Landscape Fire Severity. Fire Ecol. 2, 34–59. https://doi.org/10.4996/fireecology.0202034

Key, C.H., Benson, N.C., 2006. Landscape assessment: Sampling and analysis methods, in: Lutes, D.C. (Ed.), FIREMON: Fire Effects Monitoring and Inventory System. U.S. Department of Agriculture, Forest Service, Rocky Mountain Research Station, Fort Collins, p. 55.

Klosterman, S.T., Hufkens, K., Gray, J.M., Melaas, E., Sonnentag, O., Lavine, I., Mitchell, L., Norman, R., Friedl, M.A., Richardson, A.D., 2014. Evaluating remote sensing of deciduous forest phenology at multiple spatial scales using PhenoCam imagery. Biogeosciences 11, 4305–4320. https://doi.org/10.5194/bg-11-4305-2014

Kobayashi, S., Sanga-Ngoie, K., 2008. The integrated radiometric correction of optical remote sensing imageries. Int. J. Remote Sens. 29, 5957–5985. https://doi.org/10.1080/01431160701881889

Kolden, C.A., Smith, A.M.S., Abatzoglou, J.T., 2015. Limitations and utilisation of Monitoring Trends in Burn Severity products for assessing wildfire severity in the USA. Int. J. Wildl. Fire 24, 1023–1028. https://doi.org/10.1071/WF15082

Kulakowski, D., Seidl, R., Holeksa, J., Kuuluvainen, T., Nagel, T.A., Panayotov, M., Svoboda, M., Thorn, S., Vacchiano, G., Whitlock, C., Wohlgemuth, T., Bebi, P., 2016. A walk on the wild side: Disturbance dynamics and the conservation and management of European mountain forest ecosystems. For. Ecol. Manage. 388, 2–7. https://doi.org/10.1016/j.foreco.2016.07.037

Lentile, L.B., Holden, Z. a., Smith, A.M.S., Falkowski, M.J., Hudak, A.T., Morgan, P., Benson, N.C.N.C., Lewis, S.A., Gessler, P.E., Benson, N.C.N.C., 2006. Remote sensing techniques to assess active fire characteristics and post-fire effects. Int. J. Wildl. Fire 15, 319–345. https://doi.org/10.1071/WF05097

Lentile, L.B., Smith, A.M.S., Hudak, A.T., Morgan, P., Bobbitt, M.J., Lewis, S.A., Robichaud, P.R., 2009. Remote sensing for prediction of 1-year post-fire ecosystem condition. Int. J. Wildl. Fire 594–608.

Leverkus, A.B., Rey Benayas, J.M., Castro, J., Boucher, D., Brewer, S., Collins, B.M., Donato, D., Fraver, S., Kishchuk, B.E., Lee, E.-J., Lindenmayer, D.B., Lingua, E., Macdonald, E., Marzano, R., Rhoades, C.C., Royo, A., Thorn, S., Wagenbrenner, J.W., Waldron, K., Wohlgemuth, T., Gustafsson, L., 2018. Salvage logging effects on regulating and supporting ecosystem services — a systematic map. Can. J. For. Res. 48, 983–1000. https://doi.org/10.1139/cjfr-2018-0114

Lopuhaa, H.P., Rousseeuw, P.J., 1991. Breakdown Points of Affine Equivariant Estimators of Multivariate Location and Covariance Matrices. Ann. Stat. 19, 229–248. https://doi.org/10.1002/9781118445112.stat08190

Louis, J., Debaecker, V., Pflug, B., Main-knorn, M., Bieniarz, J., 2016. SENTINEL-2 SEN2COR : L2A PROCESSOR FOR USERS 2016, 9–13.

Mallinis, G., Mitsopoulos, I., Chrysafi, I., 2017. Evaluating and comparing Sentinel 2A and Landsat-8 Operational Land Imager (OLI) spectral indices for estimating fire severity in a Mediterranean pine ecosystem of Greece. GIScience Remote Sens. 00, 1–18. https://doi.org/10.1080/15481603.2017.1354803

Meddens, A.J.H., Kolden, C.A., Lutz, J.A., 2016. Detecting unburned areas

within wildfire perimeters using Landsat and ancillary data across the northwestern United States. Remote Sens. Environ. 186, 275–285. https://doi.org/10.1016/j.rse.2016.08.023

Melaas, E.K., Friedl, M.A., Zhu, Z., 2013. Detecting interannual variation in deciduous broadleaf forest phenology using Landsat TM/ETM+ data. Remote Sens. Environ. 132, 176–185. https://doi.org/10.1016/j.rse.2013.01.011

Milasevic, P., Ducharme, G.R., 1987. Uniqueness of the Spatial Median. Ann. Stat. 15, 1332–1333. https://doi.org/10.1214/aos/1176350511

Miller, J.D., Knapp, E.E., Key, C.H., Skinner, C.N., Isbell, C.J., Creasy, R.M., Sherlock, J.W., 2009. Calibration and validation of the relative differenced Normalized Burn Ratio (RdNBR) to three measures of fire severity in the Sierra Nevada and Klamath Mountains, California, USA. Remote Sens. Environ. 113, 645–656. https://doi.org/10.1016/j.rse.2008.11.009

Miller, J.D., Thode, A.E., 2007. Quantifying burn severity in a heterogeneous landscape with a relative version of the delta Normalized Burn Ratio (dNBR). Remote Sens. Environ. 109, 66–80. https://doi.org/10.1016/j.rse.2006.12.006

Morgan, P., Keane, R.E., Dillon, G.K., Jain, T.B., Hudak, A.T., Karau, E.C., Sikkink, P.G., Holden, Z.A., Strand, E.K., 2014. Challenges of assessing fire and burn severity using field measures, remote sensing and modelling. Int. J. Wildl. Fire 23, 1045–1060. https://doi.org/10.1071/WF13058

Nevalainen, J., Larocque, D., Oja, H., 2007. A weighted spatial median for clustered data. Stat. Methods Appl. 15, 355–379. https://doi.org/10.1007/s10260-006-0031-7

Oja, H., 2013. Multivariate Median, in: Becker, C., Fried, R., Kuhnt, S. (Eds.), Robustness and Complex Data Structures. Springer, Verlag Berlin Heidelberg, pp. 3–15. https://doi.org/10.1007/978-3-642-35494-6_1

Parker, B.M., Lewis, T., Srivastava, S.K., 2015. Estimation and evaluation of multi-decadal fire severity patterns using Landsat sensors. Remote Sens. Environ. 170, 340–349. https://doi.org/10.1016/j.rse.2015.09.014

Parks, S.A., Dillon, G.K., Miller, C., 2014. A new metric for quantifying burn severity: The relativized burn ratio. Remote Sens. 6, 1827–1844. https://doi.org/10.3390/rs6031827

Parks, S.A., Holsinger, L.M., Voss, M.A., Loehman, R.A., Robinson, N.P., 2018. Mean composite fire severity metrics computed with google earth engine offer improved accuracy and expanded mapping potential. Remote Sens. 10, 1–15. https://doi.org/10.3390/rs10060879

Picotte, J.J., Bhattarai, K., Howard, D., Lecker, J., Epting, J., Quayle, B., Benson, N., Nelson, K., 2020. Changes to the Monitoring Trends in Burn Severity program mapping production procedures and data products. Fire Ecol. 16. https://doi.org/10.1186/s42408-020-00076-y

Picotte, J.J., Robertson, K., 2011. Timing constraints on remote sensing of wildland fire burned area in the southeastern US. Remote Sens. 3, 1680–1690. https://doi.org/10.3390/rs3081680

Qiu, S., Zhu, Z., He, B., 2019. Fmask 4.0: Improved cloud and cloud shadow detection in Landsats 4–8 and Sentinel-2 imagery. Remote Sens. Environ. 231, 111205. https://doi.org/10.1016/j.rse.2019.05.024

Quintano, C., Fernandez-Manso, A., Roberts, D.A., 2017. Burn severity mapping from Landsat MESMA fraction images and Land Surface Temperature. Remote Sens. Environ. 190, 83–95. https://doi.org/10.1016/j.rse.2016.12.009

R Core Team, 2021. R: A Language and Environment for Statistical Computing.

Regione Piemonte, 2019. Piano straordinario di interventi di ripristino del territorio percorso dagli incendi boschivi dell'autunno 2017.

Rita, A., Camarero, J.J., Nolè, A., Borghetti, M., Brunetti, M., Pergola, N., Serio, C., Vicente-Serrano, S.M., Tramutoli, V., Ripullone, F., 2020. The impact of drought spells on forests depends on site conditions: The case of 2017 summer heat wave in southern Europe. Glob. Chang. Biol. 26, 851–863. https://doi.org/10.1111/gcb.14825

Roberts, D., Mueller, N., Mcintyre, A., 2017. High-Dimensional Pixel Composites From Earth Observation Time Series. IEEE Trans. Geosci.

Remote Sens. 55, 6254–6264. https://doi.org/10.1109/TGRS.2017.2723896

Roberts, D., Wilford, J., Ghattas, O., 2019. Exposed soil and mineral map of the Australian continent revealing the land at its barest. Nat. Commun. 10. https://doi.org/10.1038/s41467-019-13276-1

Roy, D.P., Kovalskyy, V., Zhang, H.K., Vermote, E.F., Yan, L., Kumar, S.S., Egorov, A., 2016. Characterization of Landsat-7 to Landsat-8 reflective wavelength and normalized difference vegetation index continuity. Remote Sens. Environ. 185, 57–70. https://doi.org/10.1016/j.rse.2015.12.024

Roy, D.P., Li, J., Zhang, H.K., Yan, L., Huang, H., Li, Z., 2017a. Examination of Sentinel-2A multi-spectral instrument (MSI) reflectance anisotropy and the suitability of a general method to normalize MSI reflectance to nadir BRDF adjusted reflectance. Remote Sens. Environ. 199, 25–38. https://doi.org/10.1016/j.rse.2017.06.019

Roy, D.P., Li, Z., Zhang, H.K., 2017b. Adjustment of sentinel-2 multi-spectral instrument (MSI) red-edge band reflectance to nadir BRDF adjusted reflectance (NBAR) and quantification of red-edge band BRDF effects. Remote Sens. 9. https://doi.org/10.3390/rs9121325

Rufin, P., Frantz, D., Yan, L., Hostert, P., 2020. Operational Coregistration of the Sentinel-2A/B Image Archive Using Multitemporal Landsat Spectral Averages. IEEE Geosci. Remote Sens. Lett. 1–5. https://doi.org/10.1109/lgrs.2020.2982245

Schroeder, W., Oliva, P., Giglio, L., Csiszar, I.A., 2014. The New VIIRS 375m active fire detection data product: Algorithm description and initial assessment. Remote Sens. Environ. 143, 85–96. https://doi.org/10.1016/j.rse.2013.12.008

Schumacher, S., Bugmann, H., 2006. The relative importance of climatic effects, wildfires and management for future forest landscape dynamics in the Swiss Alps. Glob. Chang. Biol. 12, 1435–1450. https://doi.org/10.1111/j.1365-2486.2006.01188.x

Small, C.G., 1990. A Survey of Multidimensional Medians. Int. Stat. Rev. / Rev. Int. Stat. 58, 263. https://doi.org/10.2307/1403809

Smith, R.J., 2009. Use and misuse of the reduced major axis for line-fitting. Am. J. Phys. Anthropol. 140, 476–486. https://doi.org/10.1002/ajpa.21090

Soverel, N.O., Coops, N.C., Perrakis, D.D.B., Daniels, L.D., Gergel, S.E., 2011. The transferability of a dNBR-derived model to predict burn severity across 10 wildland fires in western Canada. Int. J. Wildl. Fire 20, 518–531. https://doi.org/10.1071/WF10081

Soverel, N.O., Perrakis, D.D.B., Coops, N.C., 2010. Estimating burn severity from Landsat dNBR and RdNBR indices across western Canada. Remote Sens. Environ. 114, 1896–1909. https://doi.org/10.1016/j.rse.2010.03.013

Sudmanns, M., Tiede, D., Augustin, H., Lang, S., 2019. Assessing global Sentinel-2 coverage dynamics and data availability for operational Earth observation (EO) applications using the EO-Compass. Int. J. Digit. Earth. https://doi.org/10.1080/17538947.2019.1572799

Tarrio, K., Tang, X., Masek, J.G., Claverie, M., Ju, J., Qiu, S., Zhu, Z., Woodcock, C.E., 2020. Comparison of cloud detection algorithms for Sentinel-2 imagery. Sci. Remote Sens. 2, 100010. https://doi.org/10.1016/j.srs.2020.100010

Tramblay, Y., Koutroulis, A., Samaniego, L., Vicente-Serrano, S.M., Volaire, F., Boone, A., Le Page, M., Llasat, M.C., Albergel, C., Burak, S., Cailleret, M., Kalin, K.C., Davi, H., Dupuy, J.L., Greve, P., Grillakis, M., Hanich, L., Jarlan, L., Martin-StPaul, N., Martínez-Vilalta, J., Mouillot, F., Pulido-Velazquez, D., Quintana-Seguí, P., Renard, D., Turco, M., Türkeş, M., Trigo, R., Vidal, J.P., Vilagrosa, A., Zribi, M., Polcher, J., 2020. Challenges for drought assessment in the Mediterranean region under future climate scenarios. Earth-Science Rev. 210, 103348. https://doi.org/10.1016/j.earscirev.2020.103348

Turco, M., Rosa-Cánovas, J.J., Bedia, J., Jerez, S., Montávez, J.P., Llasat, M.C., Provenzale, A., 2018. Exacerbated fires in Mediterranean Europe due to anthropogenic warming projected with non-stationary climate-fire models. Nat. Commun. 9, 1–9. https://doi.org/10.1038/s41467-018-06358-z

Van Doninck, J., Tuomisto, H., 2017. Influence of Compositing Criterion and

Data Availability on Pixel-Based Landsat TM/ETM+ Image Compositing over Amazonian Forests. IEEE J. Sel. Top. Appl. Earth Obs. Remote Sens. 10, 857–867. https://doi.org/10.1109/JSTARS.2016.2619695

Vancutsem, C., Pekel, J.F., Bogaert, P., Defourny, P., 2007. Mean Compositing, an alternative strategy for producing temporal syntheses. Concepts and performance assessment for SPOT VEGETATION time series. Int. J. Remote Sens. 28, 5123–5141. https://doi.org/10.1080/01431160701253212

Vardi, Y., Zhang, C., 2000. The multivariate L1-median and associated data depth 97, 1423–1426.

Veraverbeke, S., Lhermitte, S., Verstraeten, W.W., Goossens, R., 2010a. The temporal dimension of differenced Normalized Burn Ratio (dNBR) fire/burn severity studies: The case of the large 2007 Peloponnese wildfires in Greece. Remote Sens. Environ. 114, 2548–2563. https://doi.org/10.1016/j.rse.2010.05.029

Veraverbeke, S., Verstraeten, W.W., Lhermitte, S., Goossens, R., 2010b. Illumination effects on the differenced Normalized Burn Ratio's optimality for assessing fire severity 12, 60–70. https://doi.org/10.1016/j.jag.2009.10.004

Verbyla, D.L., Kasischke, E.S., Hoy, E.E., 2008. Seasonal and topographic effects on estimating fire severity from Landsat TM/ETM+ data. Int. J. Wildl. Fire 17, 527–534. https://doi.org/10.1071/WF08038

Wastl, C., Schunk, C., Lüpke, M., Cocca, G., Conedera, M., Valese, E., Menzel, A., 2013. Large-scale weather types, forest fire danger, and wildfire occurrence in the Alps. Agric. For. Meteorol. 168, 15–25. https://doi.org/10.1016/j.agrformet.2012.08.011

Wei, J., Huang, W., Li, Z., Sun, L., Zhu, X., Yuan, Q., Liu, L., Cribb, M., 2020. Cloud detection for Landsat imagery by combining the random forest and superpixels extracted via energy-driven sampling segmentation approaches. Remote Sens. Environ. 248, 112005. https://doi.org/10.1016/j.rse.2020.112005

Weiszfeld, E., 1937. Sur le point pour lequel la Somme des distances de n points

donnés est minimum. Tohoku Math. Journal, First Ser. 43, 355–386.

White, J.C., Wulder, M.A., Hobart, G.W., Luther, J.E., Hermosilla, T., Griffiths, P., Coops, N.C., Hall, R.J., Hostert, P., Dyk, A., Guindon, L., 2014. Pixel-based image compositing for large-area dense time series applications and science. Can. J. Remote Sens. 40, 192–212. https://doi.org/10.1080/07038992.2014.945827

Whitman, E., Parisien, M.A., Holsinger, L.M., Park, J., Parks, S.A., 2020. A method for creating a burn severity atlas: An example from Alberta, Canada. Int. J. Wildl. Fire. https://doi.org/10.1071/WF19177

Xie, J., Kneubühler, M., Garonna, I., Notarnicola, C., De Gregorio, L., De Jong, R., Chimani, B., Schaepman, M.E., 2017. Altitude-dependent influence of snow cover on alpine land surface phenology. J. Geophys. Res. Biogeosciences 122, 1107–1122. https://doi.org/10.1002/2016JG003728

Yin, C., He, B., Yebra, M., Quan, X., Edwards, A.C., Liu, X., Liao, Z., 2020. Improving burn severity retrieval by integrating tree canopy cover into radiative transfer model simulation. Remote Sens. Environ. 236, 111454. https://doi.org/10.1016/j.rse.2019.111454

Zumbrunnen, T., Pezzatti, G.B., Menéndez, P., Bugmann, H., Bürgi, M., Conedera, M., 2011. Weather and human impacts on forest fires: 100 years of fire history in two climatic regions of Switzerland. For. Ecol. Manage. 261, 2188–2199. https://doi.org/10.1016/j.foreco.2010.10.009

Supplementary material

Table S3.1. Details regarding Sentinel-2 images used for the assessment of fire severity.

Burnt area	**Tile**	**Pre-fire acquisition date (satellite)**	**Post-fire acquisition date (satellite)**
1	32TLR	2017/10/07 (S2A)	2017/11/01 (S2B)
2	32TLQ	2017/10/07 (S2A)	2017/11/16 (S2A)

3	32TLR	2017/10/07 (S2A)	2017/11/01 (S2B)
4	32TLQ	2017/09/12 (S2B)	2017/11/16 (S2A)
5	32TLR	2017/10/07 (S2A)	2017/11/01 (S2B)
6	32TLQ	2017/10/07 (S2A)	2017/11/01 (S2B)
7	32TLR	2017/10/07 (S2A)	2017/11/16 (S2A)
8	32TLQ	2017/10/07 (S2A)	2017/11/26 (S2A)
9	32TLQ	2017/10/07 (S2A)	2017/11/26 (S2A)
10	32TLR	2017/10/07 (S2A)	2017/11/16 (S2A)

Table S3.2. Details regarding Sentinel-2 images used for the assessment of burn severity.

Burnt area	**Tile**	**Pre-fire acquisition date (satellite)**	**Post-fire acquisition date (satellite)**
1	32TLR	2017/08/23 (S2B)	2018/08/28 (S2B)
2	32TLQ	2017/07/26 (S2A)	2018/07/26 (S2B)
3	32TLR	2017/07/26 (S2A)	2018/07/19 (S2B)
4	32TLQ	2017/08/23 (S2B)	2018/08/28 (S2B)
5	32TLR	2017/08/23 (S2B)	2018/08/28 (S2B)
6	32TLQ	2017/07/06 (S2A)	2018/07/06 (S2A)
7	32TLR	2017/06/19 (S2A)	2018/06/19 (S2B)
8	32TLQ	2017/07/06 (S2A)	2018/07/04 (S2A)
9	32TLQ	2017/07/04 (S2B)	2018/07/01 (S2A)
10	32TLR	2017/07/04 (S2B)	2018/07/04 (S2A)

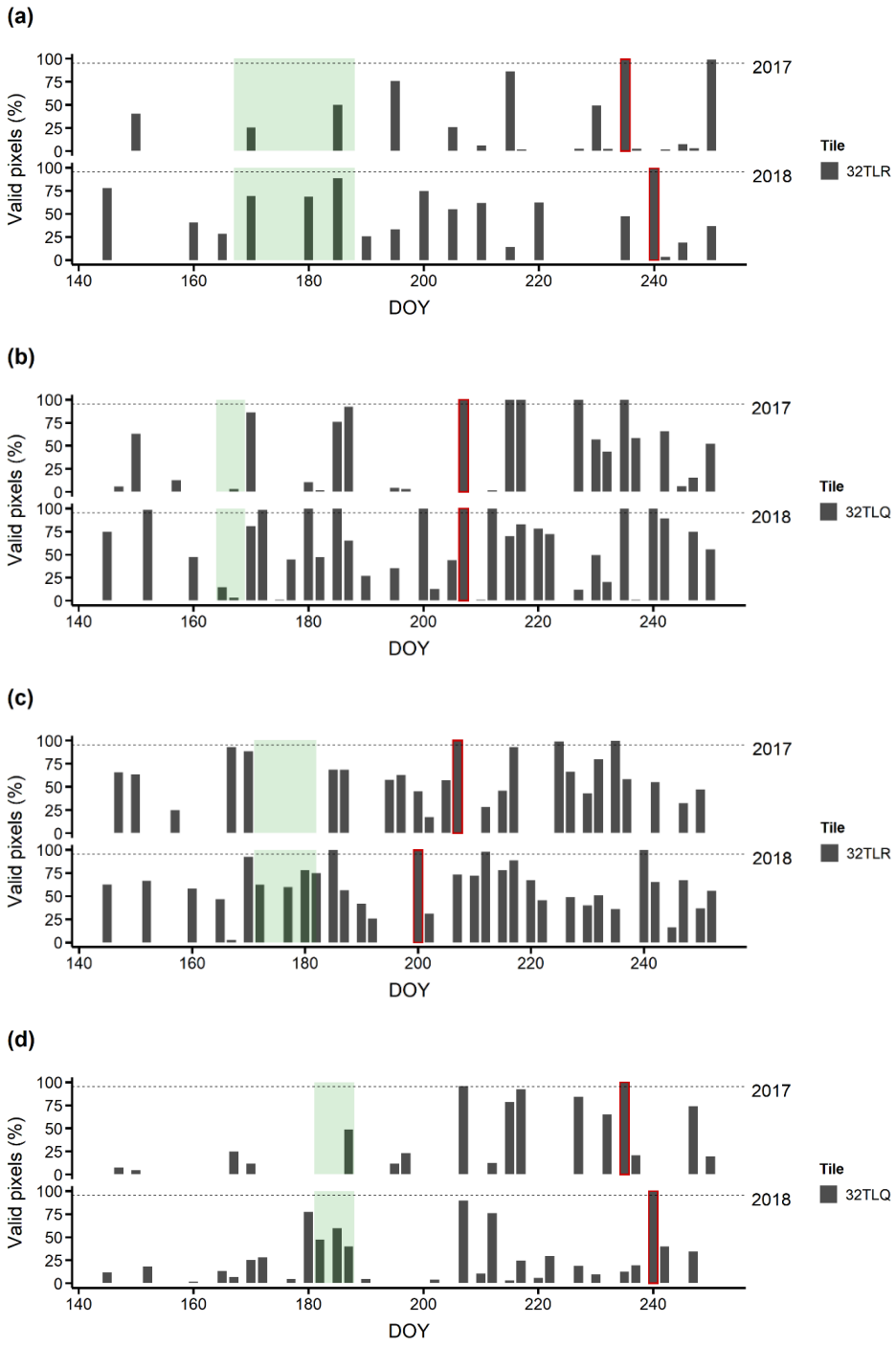
(a)
Valid pixels (%)
100
75
50
25
0
2017
2018
140
160
180
200
220
240
DOY
Tile
32TLR
(b)
Valid pixels (%)
2017
2018
DOY
Tile
32TLQ
(c)
Valid pixels (%)
2017
2018
DOY
Tile
32TLR
(d)
Valid pixels (%)
2017
2018
DOY
Tile
32TLQ

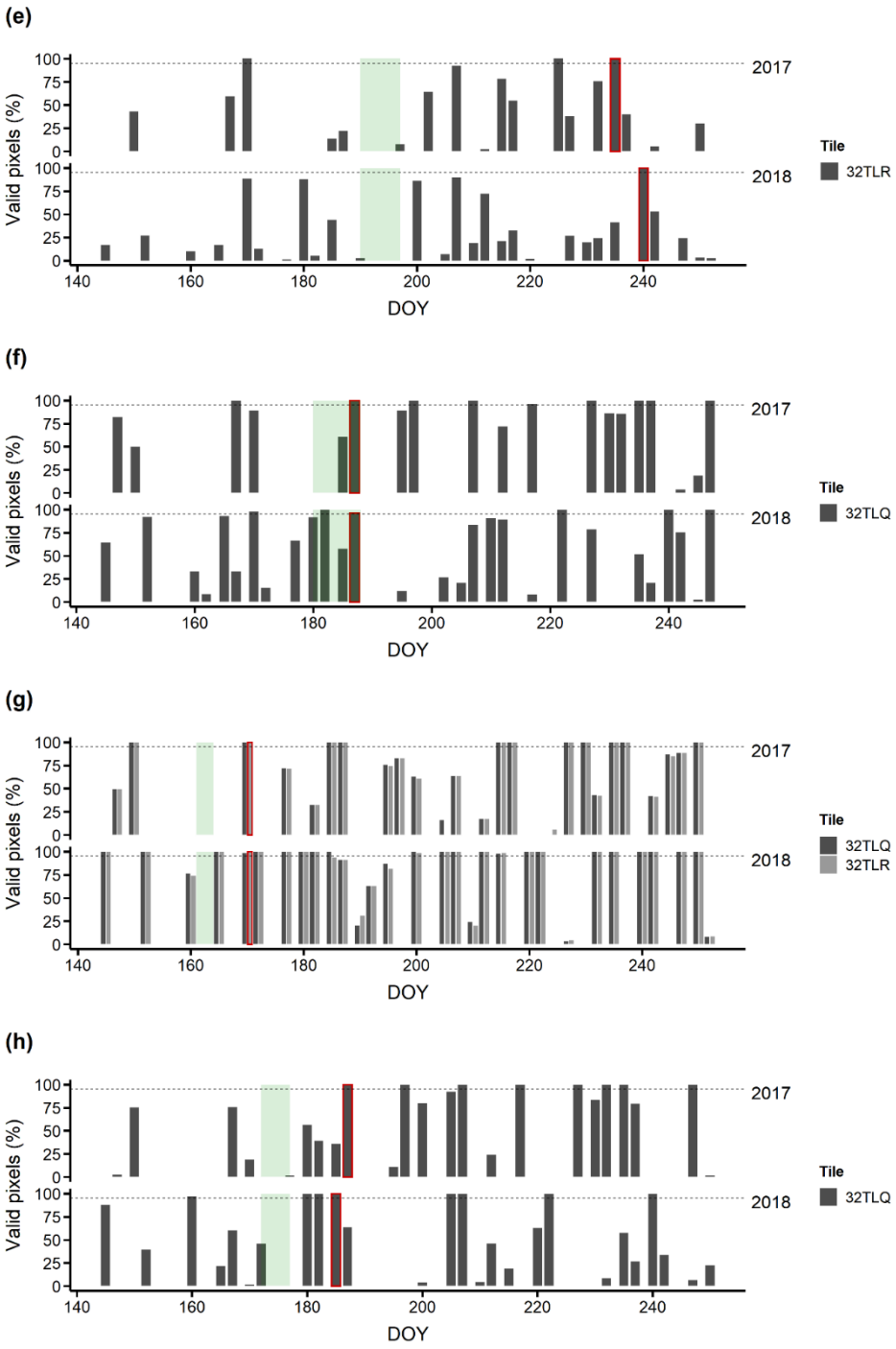
(e)
Valid pixels (%)
100
75
50
25
0
2017
2018
140
160
180
200
220
240
DOY
Tile
32TLR
(f)
Valid pixels (%)
2017
2018
DOY
Tile
32TLQ
(g)
Valid pixels (%)
2017
2018
DOY
Tile
32TLQ
32TLR
(h)
Valid pixels (%)
2017
2018
DOY
Tile
32TLQ

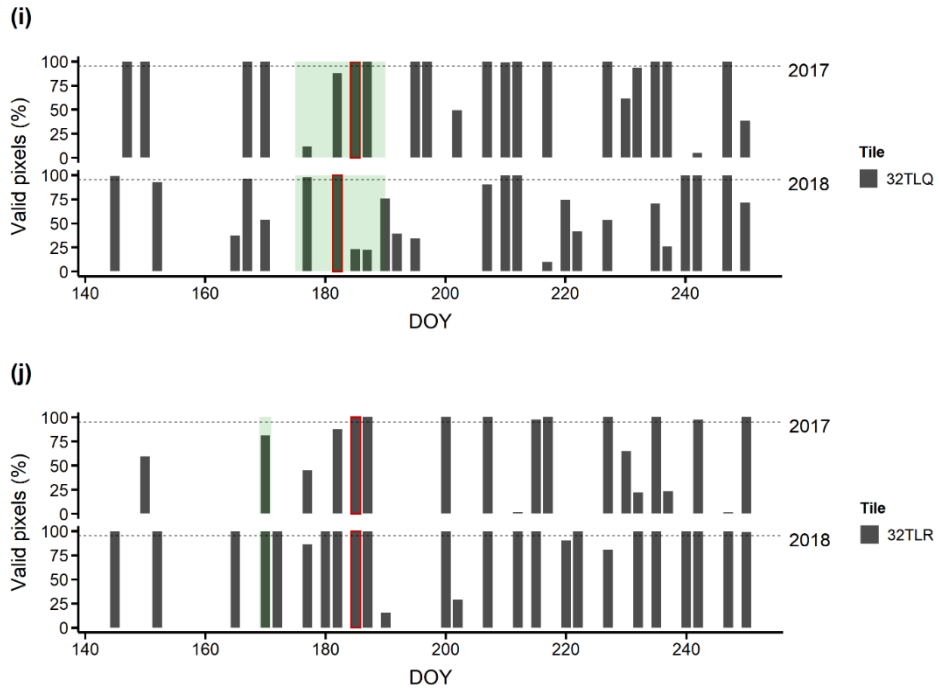

Figure S3.1. Barplots indicating the percentage of valid pixels for all the pre- and post-fire Sentinel-2 images acquired within each burnt area (1 – 10, letters a – j). The displayed time window spans from 20 May to 10 September. The dashed black line indicates the 95% threshold used for selecting paired images. Green boxes indicate the distribution of DOYs (Q1 – Q3) corresponding to the long-term peak derived from the MODIS MCD12Q2 product within each study area. Red contours indicate paired images selected for burn severity mapping.

Table S3.3. Distribution of CBI plots across burnt areas and severity categories.

Burnt area	**Unchanged to low (CBI ≤ 1.25)**	**Moderate (CBI > 1.25 and ≤ 2.25)**	**High (CBI > 2.25)**	**Total CBI plots**
1	26	30	32	88
2	16	24	0	40
3	28	11	0	39

4	6	0	0	6
5	14	1	0	15
6	3	3	3	9
7	9	13	1	23
8	6	2	0	8
9	6	0	3	9
10	14	0	0	14
All	**128**	**84**	**39**	**251**

Table S3.4. Pearson correlation coefficients between long-term LSP metrics derived from the MCD12Q2 Collection 6 product and elevation within each burnt area. All estimates were statistically significant ($p < 0.001$).

Burnt area	**Mid-Greenup (p_1)**	**Peak (p_2)**	**Senescence (p_3)**
1	0.97	0.95	0.85
2	0.84	0.86	0.42
3	0.90	0.85	0.58
4	0.87	0.86	0.76
5	0.93	0.91	0.34
6	0.90	0.90	0.71
7	0.91	0.66	0.72
8	0.84	0.79	0.53
9	0.92	0.88	0.84
10	0.79	0.76	-0.83

Table S3.5. Predicted values of bi-temporal indices (dNBR, RdNBR and RBR) discriminating between burn severity categories obtained using either paired images or reflectance composites (uncalibrated or calibrated with the dNBR offset).

Bi-temporal index	Transition between burn severity categories	Paired images		Reflectance composites	
		Uncalibrated	Calibrated	Uncalibrated	Calibrated
dNBR	Unchanged to low - moderate	124.4	121.5	138.4	132.9
	Moderate - high	485.7	484.2	519.3	514.4
RdNBR	Unchanged to low - moderate	153.6	150.3	171	164.5
	Moderate - high	600.9	597.5	639.6	633.7
RBR	Unchanged/Low - moderate	74.7	73.1	83.2	80
	Moderate - high	292.6	291.7	311.6	308.7

Chapter 4

Change detection by multispectral trends: a Landsat time series-based algorithm for forest disturbance mapping and beyond

Donato Morresi, Hyeyoung Maeng, Raffaella Marzano, Emanuele Lingua, Renzo Motta and Matteo Garbarino

This chapter has been submitted for publication to ISPRS Journal of Photogrammetry and Remote Sensing.

Abstract

Recent changes in spatial and temporal patterns of forest disturbances are mostly related to climate change and other anthropogenic factors, such as land-use change. Remote sensing data are critical to understand forest disturbance dynamics at the landscape scale. The spatial, temporal, and radiometric consistency of Landsat time series offers unprecedented insights into past disturbances that occurred during the last four decades. Many time series-based algorithms have been developed to automate the detection of land cover changes, including disturbances. Nevertheless, the sensitivity of these algorithms to low-severity and gradual disturbances has been reported to be somewhat limited. We developed the Change Detection by Multispectral Trends (CDMT) algorithm, which exploits the full spectral information provided by Landsat time series to maximise the accuracy of disturbance maps. The CDMT algorithm segments multivariate annual time series through a novel statistical procedure for changepoint detection. We designed CDMT to capture a wide range of disturbances, from non-stand-replacing to stand-replacing events. We tested CDMT to analyse trends in disturbances, including their severity, occurred in the Aosta Valley region (Italy) over a 34-year period. Our results highlighted that the user's and producer's accuracy systematically increased when moving from the

univariate to the multivariate setting. Specifically, the user's accuracy rose significantly compared to the producer's accuracy due to the lower influence of the band-dependent noise in the multivariate setting. The inclusion of multiple bands in the time series allowed CDMT to leverage the complementary information carried by bands from different portions of the electromagnetic spectrum, e.g. SWIR and NIR wavelengths. Overall, the best performing combination of bands, i.e. original spectral bands and indices, achieved an F1 score relative to the disturbed class equal to 83.1%, corresponding to a user's accuracy of 82.4% and a producer's accuracy of 83.9%. CDMT exhibited a high sensitivity to an ample spectrum of disturbance severities. For instance, it effectively captured abrupt and gradual spectral changes associated with drought-induced tree mortality. Among the strengths of CDMT, there is minimal parametrisation, which would promote its applicability in different forest ecosystems.

4.1 Introduction

Disturbances such as wildfires, windthrows, and insect or pathogen outbreaks are key components of forest ecosystems (Turner, 2010). They alter the state and trajectories of ecosystems and generate heterogeneity in space and time. The intensification of climate-driven changes in disturbance regimes has been observed globally, with negative impacts on the structure, functions and composition of forests (Forzieri et al., 2021; McDowell et al., 2020; Seidl et al., 2017). Shifts in disturbance patterns towards more frequent, larger and more severe events can drastically impair the resilience of forests and trigger transitions to a non-forest state (Johnstone et al., 2016; Millar and Stephenson, 2015; Seidl et al., 2016). Besides discrete disturbances, long-term studies based either on field (Andrus et al., 2021; Camarero et al., 2015) or remote sensing data (Cohen et al., 2016; Senf et al., 2018) highlighted increasing trends in tree mortality rates, associated with gradual, non-stand replacing disturbances. Warming temperatures and increases in severe and prolonged droughts driven by climate

change resulted in extensive forest decline globally (Allen et al., 2015, 2010). Apart from the direct effects of climate change, modifications of the interactions between disturbance agents (Seidl et al., 2017) and land-use change patterns such as land abandonment (Mantero et al., 2020) further drove shifts in disturbance regimes. Identifying changes in disturbance regimes that occurred over the last decades has crucial implications for current and future management policies (Leverkus et al., 2021). Forest ecosystems management should primarily focus on increasing resilience, for example, by favouring migration towards disturbance-adapted tree species and promoting heterogeneity of the landscape mosaic (Allen et al., 2015; Leverkus et al., 2021; Seidl, 2014).

Satellite-based remote sensing is a fundamental data source for forest ecologists as it enables a comprehensive understanding of ecological processes both in the spatial and temporal dimensions (Cohen et al., 2016; Hansen et al., 2013; Kennedy et al., 2014). In particular, continuously-acquired data of the land surface by Landsat satellites over the last four decades provide a unique opportunity to reconstruct long-term forest disturbance dynamics at the landscape scale (Hermosilla et al., 2015a; Kennedy et al., 2012; Senf et al., 2017; Wulder et al., 2019). The opening of the U.S. Geological Survey (USGS) Landsat archive in 2008 prompted a rapid increase in the use of time series for analysing forest ecosystems dynamics from regional to global scales (Banskota et al., 2014; Wulder et al., 2012).

Several automated change detection algorithms based on Landsat time series have been developed either to explicitly map forest dynamics or target a broader range of land cover changes (Cohen et al., 2017; Zhu, 2017). Zhu (2017) divided Landsat time series-based algorithms into categories defined by the mathematical approaches they rely on, i.e. thresholding, differencing, segmentation trajectory classification, statistical boundary and regression. Other characteristics like time series frequency and sensitivity to discrete and gradual events are useful for classifying these algorithms. For instance, offline algorithms operate on completely available time series, while online algorithms can process continuously-acquired data. Moreover, algorithms are either univariate or

multivariate (Zhu, 2017), depending on the number of bands, i.e. bands and indices *sensu* Cohen et al. (2020), they can simultaneously analyse. The widely-used algorithms for segmenting annual Landsat time series into linear trends like LandTrendr (Landsat-based Detection of Trends in Disturbance and Recovery; Kennedy et al., 2010) or C2C (Composite2Change C2C; Hermosilla et al., 2015b) are univariate. Conversely, algorithms based on intra-annual Landsat time series, e.g. CCDC (Continuous Change Detection and Classification; Zhu and Woodcock, 2014) and COLD (COntinuous monitoring of Land Disturbance; Zhu et al., 2019), are multivariate.

The sensitivity of time series-based automated algorithms towards low-severity forest disturbances, i.e. those causing partial canopy loss, has been reported to be somewhat limited compared, for example, to visual interpretation of spectral trajectories (Cohen et al., 2017) or bi-temporal burn severity indices (Rodman et al., 2021). While primarily used for calibration and validation purposes (Cohen et al., 2010; Olofsson et al., 2014), visual interpretation of spectral trajectories enabled to disclose shifts in patterns of forest disturbance over considerably large areas such as the U.S. (Cohen et al., 2016) and Europe (Senf et al., 2018). Extracting the weak signals associated with non-stand-replacing disturbances is hindered by noise in Landsat time series, which is generated by uncertainties in preprocessing operations like georeferencing and atmospheric correction (Cohen et al., 2017; Rodman et al., 2021; Vogelmann et al., 2016). A key issue when targeting low-severity disturbances is the proper optimisation of the parameters of an algorithm in order to balance omission and commission errors (Cohen et al., 2017; Ye et al., 2021). For instance, Ye et al. (2021) improved the detection of subtle changes induced by insect outbreaks by first optimising the parameters of the CCDC algorithm.

Recently, different ensemble approaches have been proposed to improve disturbance maps produced by Landsat time series-based algorithms (Bullock et al., 2020; Cohen et al., 2018; Healey et al., 2018; Hislop et al., 2019; Schultz et al., 2016). Ensemble approaches expanded disturbance detection capabilities in terms of accuracy and range of severities compared to those achieved with any

individual algorithm or band (Cohen et al., 2020, 2018; Healey et al., 2018). Algorithm ensembles are built using multiple change detection algorithms that are executed either in parallel (Cohen et al., 2020; Healey et al., 2018; Hislop et al., 2019) or sequentially (Bullock et al., 2020). Differences between these two approaches stem from the fact that results obtained with parallel ensembles need to be aggregated through a set of rules or using a supervised classifier (Cohen et al., 2020; Healey et al., 2018; Hislop et al., 2019). Conversely, sequentially running change detection algorithms requires the output from the first one to be used as input for the second one and so on. Multispectral ensembles (Cohen et al., 2018; Marzo et al., 2021; Schultz et al., 2016; Senf and Seidl, 2020) are built by first analysing several bands through multiple runs of a univariate algorithm. Results are then dissolved using a secondary classification model based on a supervised classifier, e.g. random forest. The advantages offered by multispectral ensembles are primarily related to the diversity of information provided by several bands (Cohen et al., 2020, 2018).

A marked growth of statistical methods for changepoint detection in multivariate time series has been observed in recent years (see reviews by Cho and Kirch, 2020 and Truong et al., 2020). The analysis of multivariate and possibly high-dimensional time series, i.e. time series with dimensions of the same order of magnitude of the observations or even larger, is a common task in many fields such as bioinformatics (Grundy et al., 2020), finance (Cho and Fryzlewicz, 2015) and telecommunications (Bardwell et al., 2019). To deal with the complexity associated with multivariate time series, one common approach is to aggregate a test statistic (Groen et al., 2013) or project the time series to a single dimension and then process the data with a univariate method (Wang and Samworth, 2018). Assumptions on the proportion of time series that undergo a change determine the most appropriate aggregation method (Groen et al., 2013). For example, the widely-used CUSUM statistic for detecting structural changes (Brown et al., 1975) has been aggregated across time series using either the average or the maximum (Groen et al., 2013; Jirak, 2015). Generally, the average of a test statistic performs better when a change occurs in the majority of the time series,

i.e. a dense change, while the maximum is more appropriate for changes occurring only in a fraction of them, i.e. a sparse change (Groen et al., 2013; Jirak, 2015). Current methods like those proposed by Enikeeva and Harchaoui (2019) and Tickle et al. (2021) highlighted their potential for detecting changes in multivariate time series when these occur both in the dense and the sparse scenarios. Changepoint methods have primarily focused on detecting changes in the mean associated with constant signals, though some approaches use piecewise polynomial models to segment time series (Cho and Kirch, 2020).

We hypothesise that segmenting annual Landsat time series through a multivariate approach could improve forest disturbance detection in a similar way to building a multispectral ensemble based on a univariate algorithm.

Here we present an automated algorithm named Change Detection by Multispectral Trends (CDMT) that we primarily developed to detect forest disturbances. CDMT is a pixel-based, offline algorithm for detecting changepoints through the segmentation of annual Landsat time series. Unlike existing segmentation algorithms, CDMT can analyse both univariate and multivariate time series, i.e. time series including multiple bands. Though CDMT can detect changes in linear trends associated with disturbances and recovery processes, here, we focused only on disturbance detection.

Our specific aims were to:

i) automate the detection of abrupt and gradual disturbances by leveraging the full spectral information provided by Landsat time series;
ii) assess how many and which bands to include in multivariate time series to maximise the accuracy relative to the detection of disturbances;
iii) analysing trends in forest disturbances and their severity in the Aosta Valley region (Italy), over a 34-year period, from 1986 to 2019.

4.2 Materials and methods

4.2.1 Study area

Our study area encompasses the Aosta Valley region in northwestern Italy and has an extension of 3262 Km^2 (Figure 4.1). The study area is covered by Path/Row 194/28, 195/28 and 196/28 of the Landsat World Reference System (WRS) 2 (Figure 4.1). Its territory is mostly mountainous, with an average elevation of 2100 m a.s.l. Forests account for 28.95% of the total area according to the Copernicus Dominant Leaf Type 2018 map (European Environmental Agency, 2020). Stands dominated by broadleaves occupy 515.61 Km^2, while those dominated by conifers amount to 428.87 Km^2. European larch (*Larix decidua* Mill.), Norway spruce (*Picea abies* (L.) Karst.) and Scots pine (*Pinus sylvestris* L.) are the dominant coniferous tree species. Common broadleaved tree species include silver birch (*Betula pendula* Roth.), maples (e.g. *Acer pseudoplatanus* L.), sweet chestnut (*Castanea sativa* Mill.) and downy oak (*Quercus pubescens* Willd.).

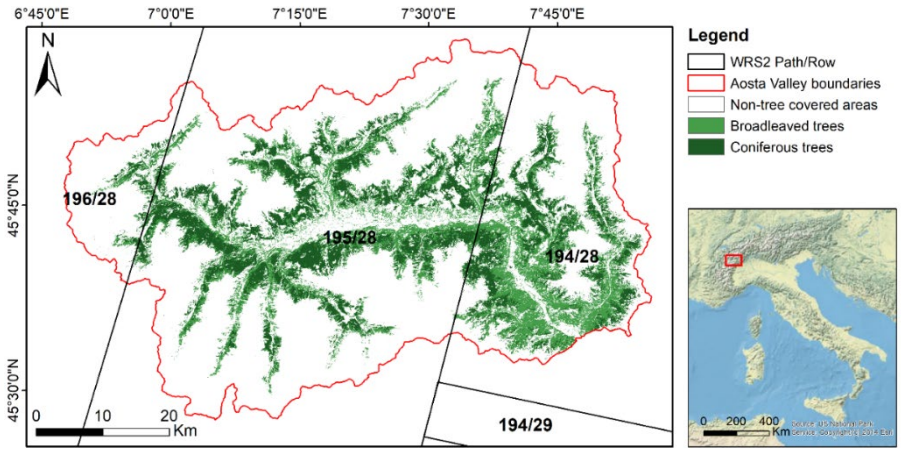

Figure 4.1. Geographic location of the study area with additional information regarding forest cover from the Dominant Leaf Type 2018 layer (European Environmental Agency, 2020) and Landsat data coverage (Path/Row) from the World Reference System (WRS) 2.

4.2.2 Landsat data

We collected all Landsat Thematic Mapper (TM), Enhanced Thematic Mapper + (ETM+) and Operational Land Imager (OLI) Level 1 Tier 1 imagery from Collection 1 acquired between 1985 and 2020 with < 80% cloud cover. We processed images at surface reflectance using the Framework for Operational Radiometric Correction for Environmental monitoring (FORCE) software (version 3.6.5, available at https://github.com/davidfrantz/force; Frantz, 2019). The FORCE Level 2 Processing System allowed us to: (i) perform atmospheric correction based on radiative transfer modelling including adjacency effects (Frantz et al., 2016) and (ii) compute Nadir BRDF (Bidirectional Reflectance Distribution Function)-Adjusted Reflectance (NBAR) through a fixed global set of MODIS (Moderate Resolution Imaging Spectroradiometer) BRDF kernel parameters (Roy et al., 2017a, 2017b). We removed pixels contaminated by clouds, cloud shadows and snow using the Quality Assessment (QA) band provided by the USGS for every Landsat Collection 1 Level 1 image. The QA band is produced using the C Function of Mask (CFmask) algorithm (Foga et al., 2017).

We produced yearly reflectance composites using all the six bands of the TM/ETM+ sensors and the corresponding OLI bands relative to the growing season using the geometric median approach (Roberts et al., 2017). For each year, we defined an adaptive compositing period spanning between June 1 and September 30 that iteratively widened up to 20 days at both of its sides until at least three clear observations were found. This approach allowed us to maximise the robustness of the geometric median (Morresi et al., 2022).

We computed eight spectral indices (Table 4.1) that are commonly used in the context of forest disturbance detection (Banskota et al., 2014; Cohen et al., 2018; DeVries et al., 2016).

Table 4.1. List of the spectral indices used in this study.

Index	Formulation	Direction of change caused by a disturbance	Reference
Normalized Difference Vegetation Index (NDVI)	(NIR – RED)/ (NIR + RED)	decrease	(Rouse et al., 1973)
Normalized Difference Moisture Index (NDMI)	(NIR – SWIR1)/ (NIR + SWIR1)	decrease	(Wilson and Sader, 2002)
Normalized Burn Ratio (NBR)	(NIR – SWIR2)/ (NIR + SWIR2)	decrease	(García and Caselles, 1991)
Moisture Stress Index (MSI)	NIR/SWIR1	increase	(Hunt Jr and Rock, 1989)
Tasseled Cap Brightness (TCB)	0.3037∗BLUE+0.2793∗ GREEN+0.4743∗RED+ 0.5585∗NIR+0.5082∗ SWIR1+0.1863∗SWIR2	increase	(Crist, 1985)
Tasseled Cap Greenness (TCG)	−0.2848∗BLUE−0.2435∗ GREEN−0.4743∗RED+ 0.7243∗NIR+0.0840∗ SWIR1−0.1800∗SWIR2	decrease	(Crist, 1985)
Tasseled Cap Wetness (TCW)	0.1509∗BLUE+0.1973∗ GREEN+0.3279∗RED+ 0.34065∗NIR−0.7112∗ SWIR1−0.4572∗SWIR2	decrease	(Crist, 1985)
Tasseled Cap Angle (TCA)	arctan(TCB/TCG)	decrease	(Powell et al., 2010)

4.2.3 Overview of the algorithm

CDMT builds on a novel statistical procedure to segment multivariate Landsat time series into linear trends and detects changepoints. Linear trends are suitable approximations of annual Landsat time series that enable algorithms to detect abrupt and gradual changes associated with forest disturbance and recovery processes (Hermosilla et al., 2015b; Hughes et al., 2017; Kennedy et al., 2010). Operationally, CDMT builds multispectral time series by extracting values from time-ordered sequences of data cubes (Figure 4.2). The High-dimensional Trend Segmentation (HiTS) procedure (Maeng, 2019, publicly available at https://github.com/hmaeng/HiTS) is at the core of our algorithm. The HiTS procedure was designed to detect multiple changepoints in multivariate and possibly high-dimensional data sequences. It is a generalisation into higher dimensions of the TrendSegment procedure (Maeng and Fryzlewicz, 2019) that partitions univariate data sequences into linear trends to detect multiple changepoints.

We note that CDMT can also analyse univariate time series and does not detect changes either in the first or in the last year of the time series. Specifically, the HiTS procedure can detect changepoints at every time point except the first, while CDMT needs an observation after each changepoint to remove impulsive noise (Section 2.4.1).

As CDMT and the HiTS procedure heavily rely on matrix-based operations and are written in plain R (R Core Team, 2021), we optimised computational efficiency using the “matrixStats” package (Bengtsson, 2021). We employed the “terra” package (Hijmans, 2022) to manipulate raster data and parallelise processing.

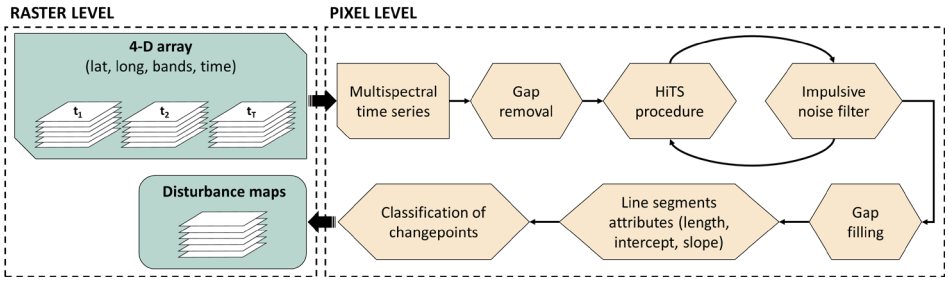

Figure 4.2. Flowchart of the processing steps performed by CDMT at the raster and pixel-level when analysing multispectral time series. Input data consist of four-dimensional arrays where bands and time form the third and fourth dimensions, respectively.

4.2.4 Processing of multispectral time series

CDMT processes only time series containing one-year gaps and removes them at the beginning of the processing. This implies that those time series with gaps longer than one year are discarded. CDMT employs an iterative procedure to discern between changepoints associated with forest dynamics and those caused by impulsive noise, i.e. outliers in the spectral signal that are associated, for example, with undetected clouds, cloud shadows or haze (Hermosilla et al., 2015b; Kennedy et al., 2010). The iterative procedure for removing spurious changepoints continues until either all are removed, or five iterations are performed. If changepoints and gaps co-occur in a multispectral time series, CDMT updates the corresponding year of change depending on the number of gaps preceding each changepoint. It imputes gaps in each band using values of linear segments previously estimated by the HiTS procedure. Specifically, gaps located at the vertices of segments of at least three years in length are imputed using linear extrapolation based on the two preceding values. Otherwise, gaps are filled using the preceding value. Gaps located in the middle of a segment are filled using linear interpolation between the preceding and the following values. This approach is similar to that proposed by Hermosilla et al. (2015b) and determines that changepoints co-occurring with gaps are detected with a one-year lag.

4.2.5 Impulsive noise filter

CDMT removes impulsive noise through a two-stage procedure consisting of the identification of candidate time points and their verification. CDMT leverages the ability of the HiTS procedure to detect point anomalies (Section 4.2.6), as these may correspond to spurious changepoints. Furthermore, CDMT computes two change magnitudes for each band:

$$d_1 = |v_{t-1} - v_t|, \quad (1)$$

$$d_2 = |v_{t-1} - v_{t+1}|,$$

where *t* corresponds either to a changepoint or to the time point preceding that changepoint. It then checks if, in any band, the following condition is satisfied: d_1 is greater than four times the estimated standard deviation (Equation 3), and d_2 is smaller than the standard deviation. These values ensure that changepoints followed by anomalously rapid spectral recovery are included among candidate time points.

CDMT re-analyses multispectral time series during the verification stage by iteratively removing each candidate time point. When it detects a changepoint at the candidate time point or nearby, considering a one-year offset, it labels the changepoint as an actual change. Otherwise, CDMT replaces invalid values through linear interpolation based on the preceding and following observations.

4.2.6 Modified HiTS procedure

In this section, we first provide a brief description of the HiTS procedure proposed in Maeng (2019) and then describe how we modified it for analysing Landsat time series. The changepoint model proposed by HiTS considers a multivariate time series data containing *n* variates of length *T* as follows:

$$X_{i,t} = f_{i,t} + \varepsilon_{i,t}, \quad (2)$$

where $f_i = (f_{i,1}, \dots, f_{i,T})^\top$ is the piecewise linear signal of the time series $X_i = (X_{i,1}, \dots, X_{i,T})^\top$ and $\varepsilon_i = (\varepsilon_{i,1}, \dots, \varepsilon_{i,T})^\top$ is the independent Gaussian random error

with mean zero and variance σ^2. The model assumes that the signal vectors $\{f_i\}_{i=1}^n$ have the form of a piecewise linear function and share N distinct changepoints at unknown locations $\eta_1, \ldots, \eta_N$ in the sense that at each changepoint, at least one signal vector undergoes a change in its linear trend, whether in the intercept or the slope or both. HiTS was designed to work well in detecting multiple changepoints corresponding to linear trend changes or point anomalies, which are large deviations of the signal from its neighbouring segments. It consists of four main steps: (1) High-dimensional Tail-Greedy Unbalanced Wavelet (HiTGUW) transform, (2) thresholding, (3) inverse HiTGUW transformation and (4) post-processing.

The core ingredient of the HiTS procedure is the HiTGUW transform, a bottom-up transformation of multivariate time series data through constructing a data-driven wavelet basis. Starting from the finest scale, i.e. using raw input data of dimension $n \times T$, the HiTGUW transform recursively merges neighbouring regions of the data from bottom to top and is completed after $T - 2$ local orthonormal transformations that result in a multiscale decomposition of the input matrix with $n \times (T-2)$ detail-type coefficients and $n \times 2$ smooth-type coefficients. The detail coefficient plays an important role in deciding which region should be merged first, as its size indicates the strength of local linearity; the detail coefficient becomes zero only when the raw observations in the corresponding merged region have a perfect linear trend. The merges are performed by giving priority to the interval whose (aggregated) detail coefficient has the smallest size, where the aggregation strategy is based on computing the maximum detail coefficient over n time series that corresponds to the maximum deviation from linearity over n time series at a given time interval. The resulting HiTGUW transform enables the sparse representation of the data in that the bulk of variance of the input data is encoded in only a few detail coefficients obtained at later merges. This justifies thresholding as the following step, where the pruning is performed in a way of deciding the significance of the sparse representation of the input data. Note that HiTS can deal with the case when the standard deviation of the error, σ_i, varies across time series X_i, as it can be estimated using the

median absolute deviation (Hampel, 1974) that is adjusted for achieving asymptotic normal consistency (Equation 3).

$$\hat{\sigma}_i = \left(MAD\left(X_{i,1} - 2X_{i,2} + X_{i,3}, \ldots, X_{i,T-2} - 2X_{i,T-1} + X_{i,T}\right) \times 1.4826\right)/\sqrt{6} \quad (3)$$

In thresholding, the detail coefficient matrix obtained in the HiTGUW transform is used. For each changepoint candidate, the corresponding detail coefficients are aggregated over n time series, and if its size is greater than a pre-specified threshold, it survives. The threshold used to detect significant deviations from linearity is computed as follows:

$$\lambda = C\sqrt{2log\ (nT)}, \quad (4)$$

where n is the number of time series, T is their length, and C = 1.2 is recommended in Maeng (2019). The inverse HiTGUW transformation performs inverted, i.e. transposed, orthonormal transformations in reverse order to that in which they were initially performed. This step uses the thresholded detail coefficients to produce the estimated piecewise linear signal composed of best linear regression fits (i.e. minimising the sum of squared errors) for each estimated segment. Lastly, in the post-processing step, non-significant changepoints are removed by performing the first three steps of the HiTS procedure using the estimated functions computed by the inverse HiTGUW transformation as input data. The reader is referred to Maeng (2019) for more details on the HiTS procedure.

The original HiTS procedure was designed to prioritise the detection of sparse and high magnitude changes, irrespective of their duration, i.e. the length of the linear segment following a changepoint (Maeng, 2019). For instance, we consider two types of change: the change that is sparse across n time series with high magnitude and the change that is dense across the panel with low magnitude. If both types of change exist in a multivariate time series, the HiTS procedure prioritises the sparse change detection. This behaviour was determined by the aggregation approach of the detail coefficients in the HiTGUW transformation and thresholding step, which is based on the maximum among the individual time series. Our modification of the HiTS procedure aims at reducing its sensitivity to

noise while extending the range of disturbance severities to include persistent and low-severity events. These latter correspond to non-stand replacing disturbances such as those caused by insects, disease and drought-induced mortality (Cohen et al., 2016; Coops et al., 2020).

First, at every iteration of the HiTGUW transformation, we multiplied the detail coefficients of each band by a weight w_p, computed as follows:

$$w_p = \frac{\sum_{i=1}^{n-1} R_{pi}^2}{(n-1)} \; for \; i \neq p, \tag{5}$$

where R_{pi}^2 is the coefficient of determination relative to the pairwise linear regression between bands p and i. Our weighting system follows an opposite rationale compared to that proposed by Bullock et al. (2020), who prioritised uncorrelated Landsat bands when aggregating the test statistic for the Chow test. We regarded the average pairwise coefficient of determination as a proxy metric for the predictive power of each band.

Second, in the HiTGUW transformation, we aggregated the detail coefficients by summing the maximum and the average. This modification allowed us to prioritise dense and persistent changes over extremely sparse and ephemeral ones.

Third, in the thresholding step, we aggregated the detail coefficients using either the maximum or the weighted average based on band-specific weights (Equation 5). To select the optimal aggregation method, we employed the modified Bayesian Information Criterion (BIC) proposed by Hall et al. (2013), which contains the following penalty term:

$$P(N) = k(N+1) + 3N, \tag{6}$$

where k is the number of parameters that define each linear segment, i.e. intercept and slope, and N is the number of changepoints. We summarised the BIC among bands for each aggregation method through the weighted average, using weights assigned to each band (Equation 5). The penalty term in Equation 6 effectively limited data overfitting, which was a condition arising mainly with the maximum statistics. Nevertheless, the maximum pointwise detail coefficient among bands

allowed CDMT to detect abrupt and non-stand-replacing disturbances, e.g. diffuse windthrows, producing a weak signal in the majority of the bands.
Finally, we applied the finite sample bias correction factor proposed by Park et al. (2019) to the MAD (Equation 3) to improve the estimation of the standard deviation performed by the HiTS procedure.

4.2.7 Classification of changepoints

CDMT employs a decision tree to classify changepoints detected by the HiTS procedure into three classes: abrupt disturbances, gradual disturbances, and other events, e.g. post-disturbance reforestation (Figure 4.3). It evaluates each node based on the majority vote of the bands while it regards ties as negative outcomes. CDMT first determines whether a changepoint is associated with an abrupt or a gradual change by determining if it occurred mainly in the intercept or slope, as segments in the piecewise linear model estimated by the HiTS procedure are discontinuous. Specifically, CDMT computes two change magnitudes:

$$m_1 = v_{t-1} - v_t, \tag{7}$$

$$m_2 = v_{t-1} - v_{t+1},$$

where v and t correspond to the values estimated by the HiTS procedure and the time index of the changepoint, respectively. These change magnitudes (m_1 *and* m_2) correspond to those in Equation 1, although CDMT retains the information regarding the direction of change. Specifically, it compares the absolute values of m_1 and m_2 with the standard deviation of the time series (Equation 3) and checks for the concordance of their sign. Abrupt changes require that both m_1 and m_2 are greater than the standard deviation and that their signs have the same direction (Figure 4.3). Depending on whether the change was abrupt or gradual, CDMT evaluates the direction of change using either the sign of m_1 or the slope of the segment beginning at the changepoint (Figure 4.3). We note that CDMT requires the reference direction of change for each band as ancillary information (Table 4.1).

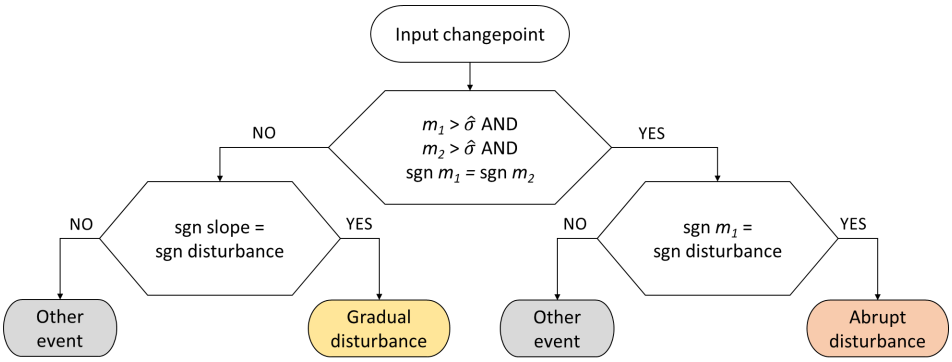

Figure 4.3. Decision tree employed by CDMT to classify changepoints in multispectral time series. The sign function is abbreviated with "sgn". The majority vote among bands determines the outcome at each node.

After classifying changepoints, CDMT computes the duration of disturbances. Abrupt events last for one year, i.e. the frequency of the time series, while the duration of gradual disturbances corresponds to the length of the segment beginning with the changepoint.

4.2.8 Spectral change magnitude and disturbance severity

For every band, the change magnitude associated with an abrupt disturbance is equal to m_1 (Equation 7). Conversely, the spectral change magnitude of a gradual disturbance corresponds to the difference between the values estimated by the HiTS procedure at the onset and ending years of that event, i.e. the vertices of the segment beginning with the changepoint. CDMT computes a synthetic spectral change magnitude for every disturbance, which is the median of the change magnitudes among bands in relative terms. Following Cohen et al. (2016), spectral change magnitudes are relativised by dividing for the estimated pre-disturbance value.

We converted the synthetic spectral change magnitude into disturbance severity, discriminating between stand-replacing and non-stand-replacing disturbances, as proposed by Senf and Seidl (2020). Specifically, we employed a logistic regression to predict the disturbance severity associated with synthetic spectral

change magnitude. Disturbance severity corresponded to the probability for a given pixel of being disturbed by a stand-replacing or a non-stand-replacing event. We selected the optimal threshold discriminating between these two classes *a posteriori*, using the "MinROCdist" criteria in the "PresenceAbsence" R package (Freeman and Moisen, 2008a, 2008b). This threshold minimises the distance between the receiver operating characteristic (ROC) curve and the upper-left corner in the ROC plot.

To locate Landsat pixels corresponding to stand-replacing samples, we employed a comprehensive set of stand-replacing patches provided by the Regional Forest Service of the Aosta Valley. The perimeters of these patches were either delineated through the collection of GPS points during field surveys or by visual digitisation of aerial orthophotos. We randomly sampled 1500 Landsat pixels equally distributed among three main disturbance types: wildfires, windthrows and downslope mass movements, including snow avalanches and landslides. Stratification by disturbance type allowed us to account for differences in spectral changes, e.g. fire typically caused higher spectral change magnitudes compared to other disturbances. We located non-stand-replacing samples within the same disturbed patches, but outside stand-replacing perimeters and employed the same procedure described for the collection of stand-replacing samples, holding the sample size constant.

4.2.9 Algorithm parametrisation

CDMT requires a few parameters to be set prior to analyse multispectral time series. Our tests highlighted that the coefficient associated with standard deviation for detecting spurious changepoints (Section 4.2.5) had a negligible impact on the accuracy of the algorithm. The threshold (λ) controlling the significance of changepoints is the most important parameter in the HiTS procedure (Equation 4). When the length of the multispectral time series is held constant, λ varies as a function of both the number of bands included in multispectral time series and the parameter C (Figure 4.4). We tested the effect

of the parameter *C* on accuracy metrics using values comprised in the interval [1, 1.3].

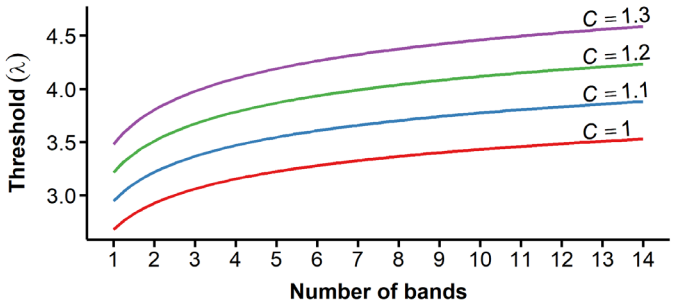

Figure 4.4. Example of thresholds (λ) employed in the HiTS procedure for detecting changepoints using different values of the parameter *C* (Equation 4). Thresholds varied as a function of the number of bands included in a multispectral time series. The length of this latter is equal to 36 and corresponds to the length of annual Landsat time series in the present study.

Selecting the bands to be included in multispectral time series is crucial, as these are characterised by different sensitivity to forest disturbances, e.g. Cohen et al. (2018); DeVries et al. (2016); Schultz et al. (2016). To evaluate the influence of each band on the detection accuracy of disturbances (Section 4.2.11), we tested all the unique combinations based on six Landsat reflectance bands (Blue, Green, Red, NIR, SWIR1 and SWIR2) and eight spectral indices (Table 4.1). The length of the unique combinations ranged from a single band to all of them, i.e. 14.

4.2.10 Accuracy assessment

Following other studies, e.g. Cohen et al. (2016); Hermosilla et al. (2015a), our definition of forest disturbance was as broad as possible. We included every spectral change in the direction of a forest disturbance irrespective of whether it was associated with a stand-replacing or non-stand-replacing event. Changes had to be discernible at least in Landsat time series and low-severity and gradual

disturbances had to last for at least three years. This was necessary for avoiding confusion between disturbances and normal inter-annual fluctuations.

We assessed the accuracy of CDMT in detecting abrupt and gradual disturbances by considering them as individual events in space and time, following the approach proposed in other studies (Bullock et al., 2020; Cohen et al., 2017; Zhu et al., 2019). In particular, we evaluated either the year when an abrupt disturbance was detectable or the onset year of a gradual disturbance. We determined the occurrence of a disturbance event by simultaneously visualising annual multispectral Landsat time series at the plot level and the corresponding raster data in QGIS software. Raster data comprised RGB false-colour composites derived from Landsat yearly reflectance data (R=SWIR2, G=NIR, B=Red) and high-resolution imagery. Among high-resolution aerial imagery, there were historical black and white orthophotos acquired within the periods 1988-1989 and 1994-1997, and natural colour orthophotos acquired within the period 1999-2000 and in 2006 and 2012. High-resolution satellite imagery included those provided free-of-charge by Google, Bing and Esri. Furthermore, we employed disturbance perimeters provided by the Regional Forest Service of the Aosta Valley (Section 2.7) as reference data for those plots located within them.

Our reference dataset included 1408 plots, each corresponding to a Landsat pixel: disturbed plots were 630 in total while those undisturbed were 778. By evaluating individual years for each plot, we obtained 50724 sample units, of which 726 were disturbance events as some plots were disturbed multiple times. Using a confusion matrix, we computed three accuracy metrics relative to the disturbed class: user's accuracy (UA; equation 8), producer's accuracy (PA; equation 9) and F1 score (equation 10).

$$UA = \frac{True\ Positive}{(True\ Positive + False\ Positive)} \times 100 \quad (8)$$

$$PA = \frac{True\ Positive}{(True\ Positive + False\ Negative)} \times 100 \quad (9)$$

$$F1\ score = 2 \times \frac{UA \times PA}{UA + PA} \quad (10)$$

To build the reference dataset, we initially selected 2000 pixels among those detected by CDMT as disturbed or undisturbed through stratified random sampling. The disturbance map that we used for the selection of validation plots was derived from the analysis of multispectral time series formed by six bands: SWIR1 and SWIR2 Landsat bands, NBR, NDMI, TCW and TCA. Cohen et al. (2018) highlighted that these bands are particularly effective for detecting forest disturbances through annual Landsat time series due to their high Disturbance Signal To Noise Ratio (DSNR). We spatially constrained the selection of pixels through a forest mask built by merging the forest classes of the Corine Land Cover (CLC) maps relative to the years 1990 and 2018. Specifically, we included the following classes: broadleaved forest, conifer forest, mixed forest and transitional woodland. Moreover, we retained only those pixels that were covered by at least 50% of tree canopies at any time within the analysis period.

4.3 Results

4.3.1 Algorithm assessment: impulsive noise

CDMT was robust towards impulsive noise due to two mechanisms: the filter and the insensitivity of the modified HiTS procedure to sparse and ephemeral changes. Impulsive noise occurring in all the bands caused a dense change that was detected by the HiTS procedure, identified and then removed by CDMT (Figure 4.5a). Conversely, when impulsive noise occurred sparsely across bands, the HiTS procedure did not detect any changepoint during these years (Figure 4.5b). Hence, CDMT did not activate the filter when impulsive noise was overlooked by the HiTS procedure (Figure 4.5b).

The sensitivity of the modified HiTS procedure to dense and persistent changes allowed the CDMT algorithm to effectively discriminate between forest disturbances and impulsive noise (Figure 4.5c). The spectral signal associated with a disturbance, e.g. wildfire, can resemble that of impulsive noise when rapid

post-disturbance vegetation recovery occurs. However, spectral changes associated with disturbances can be still detected during the following years, even if the strength of the signal decreased heterogeneously across bands (Figure 4.5c).

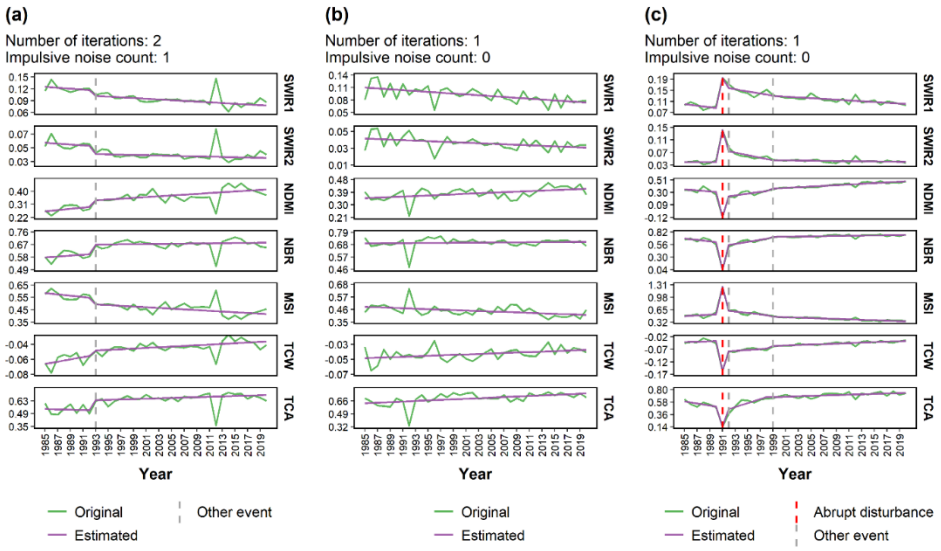

Figure 4.5. Example of multispectral time series relative to three different pixels, containing either impulsive noise (**a, b**) or spectral changes caused by a wildfire (**c**). Vertical dashed lines indicate changepoints. Impulsive noise occurred in 2012 (**a**), 1992 and 1996 (**b**). CDMT correctly retained the changepoint associated with a wildfire in 1991, despite its similarity with impulsive noise due to the rapid post-fire recovery of some bands.

By analysing univariate time series, i.e. each individual band separately, we were able to disentangle the effect of the impulsive noise filter on the user's and producer's accuracy (Figure 4.6, Table S4.1). When CDMT removed impulsive noise, the user's accuracy increased for all the bands (Figure 4.6b), and the median increase was 3.2%. Differences with unfiltered data ranged from 1.7% (Blue and SWIR1) to 5.6% (Red). Conversely, the producer's accuracy slightly decreased for most of the bands and increased for some: differences with unfiltered data varied from -3% (SWIR1) to 0.7% (TCA). In general, the median

decrease in producer's accuracy among bands was equal to 0.5%.

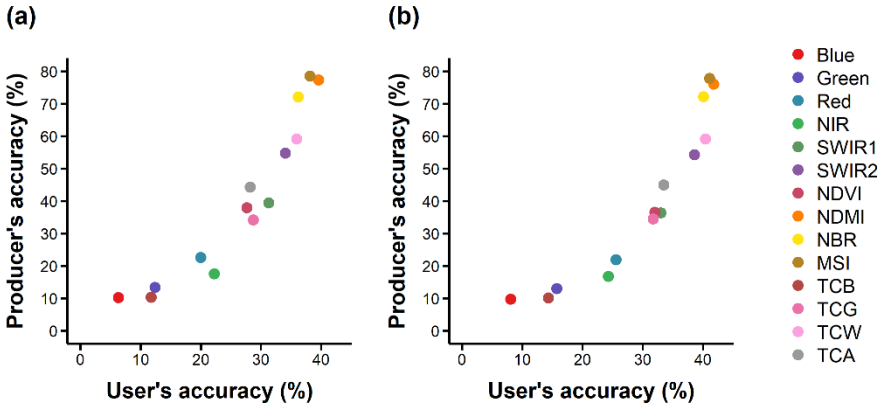

Figure 4.6. User's and producer's accuracy achieved by the CDMT algorithm using univariate time series. The impulsive noise filter was either deactivated (**a**) or activated (**b**) during the analysis of the time series.

The capability of CDMT to separate the spectral signal associated with forest dynamics from impulsive noise and fill gaps was noticeable by comparing input bands and estimated values (Figure 4.7). In 2012, for instance, only images acquired by the ETM+ sensor onboard Landsat 7 were available, which caused a widespread presence of artefacts and gaps in the input bands (Figure 4.7a, d) due to the scan-line corrector failure in 2003 (Ju and Roy, 2008). On the contrary, the values estimated by CDMT were gap-filled and natural-looking, as they exhibited similarity with their neighbourhood (Figure 4.7b, e). The absolute residuals (Figure 4.7c, f) highlighted the location of those artefacts correctly detected by CDMT.

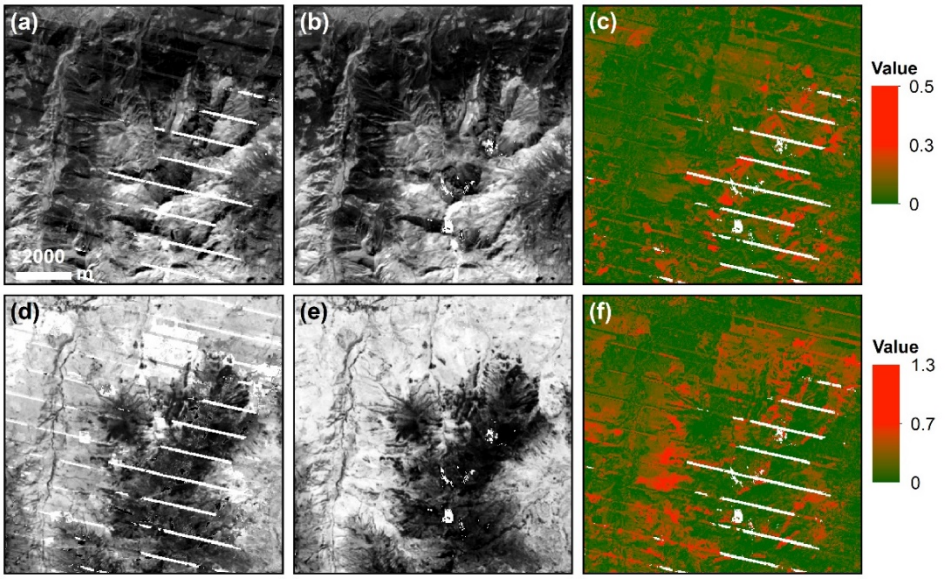

Figure 4.7. Spatial subset of the study area showing data of 2012 relative to the SWIR1 band (**a-c**) and TCA index (**d-f**). The first column (**a, d**) contains input data for the CDMT algorithm. Only Landsat 7 ETM+ images were available to generate pixel-based reflectance composites in 2012. The second column (**b**, **e**) contains values estimated and gap-filled by the CDMT algorithm while third column depicts absolute residuals (**c, f**). Vegetated areas correspond either to darker (**a**, **b**) or brighter patches (**d, e**) and were located in the upper and left part the subset.

4.3.2 Algorithm assessment: weights and change thresholds

Weights influenced accuracy metrics relative to the disturbed class when we included at least three bands: the effects on the user's and producer's accuracy were dissimilar, while they mostly increased the F1 score (Figure 4.8). In particular, the user's accuracy of weighted bands was lower than for those unweighted, albeit differences diminished when the number of bands increased (Figure 4.8a). On the contrary, the producer's accuracy generally increased, particularly when the number of bands was equal to or higher than four (Figure 4.8b-c). Considering the best performing combination in terms of F1 score (Table

4.2), bands contrasting NIR and SWIR bands, i.e. NDMI, NBR and MSI, as well as TCW, had higher median weights compared to individual SWIR1 and SWIR2 bands (Figure 4.9, Table S4.2). The median TCA weight was slightly higher than that of the SWIR1 band (Figure 4.9, Table S4.2).

Regarding parameter *C* (Equation 4), we achieved the best performance in terms of the F1 score when we set it at 1.2 (Figure S4.1, Table S4.3). The producer's accuracy increased when we decreased the parameter *C,* albeit the decrease in the user's accuracy was much higher. For example, we consider the combination length that resulted in the maximum F1 score, i.e. seven weighted bands (Table 4.2): decreasing the parameter *C* from 1.2 to 1 increased the maximum producer's accuracy by 4.3%, vice versa, the maximum user's accuracy decreased by 9.2% (Table S4.3).

4.3.3 Algorithm assessment: bands combinations

Accuracy metrics relative to disturbed pixels benefited from the inclusion of multiple bands in the time series to different extents (Figure 4.8). User's accuracy asymptotically rose, with a sharp increase from univariate to bivariate time series (Figure 4.8a). Conversely, the producer's accuracy marginally increased, as its maximum values slightly rose until we included five (unweighted) or seven (weighted) bands. Adding more bands decreased the producer's accuracy markedly (Figure 4.8b). The median F1 score steeply rose until three bands were included, reached a peak at five bands and then slightly decreased (Figure 4.8c). Conversely, the maximum F1 score reached a peak at six (unweighted) or seven (weighted) bands (Figure 4.8c, Table 4.2). Overall, the best performing combination in terms of F1 score included seven weighted bands, i.e. SWIR1, SWIR2, NDMI, NBR, MSI, TCW and TCA. Its value was equal to 83.1%, corresponding to a user's accuracy of 82.4% and a producer's accuracy of 83.9% (Table 4.2). The bands above also corresponded to those included more often in the best performing combinations of every length (Table 4.3).

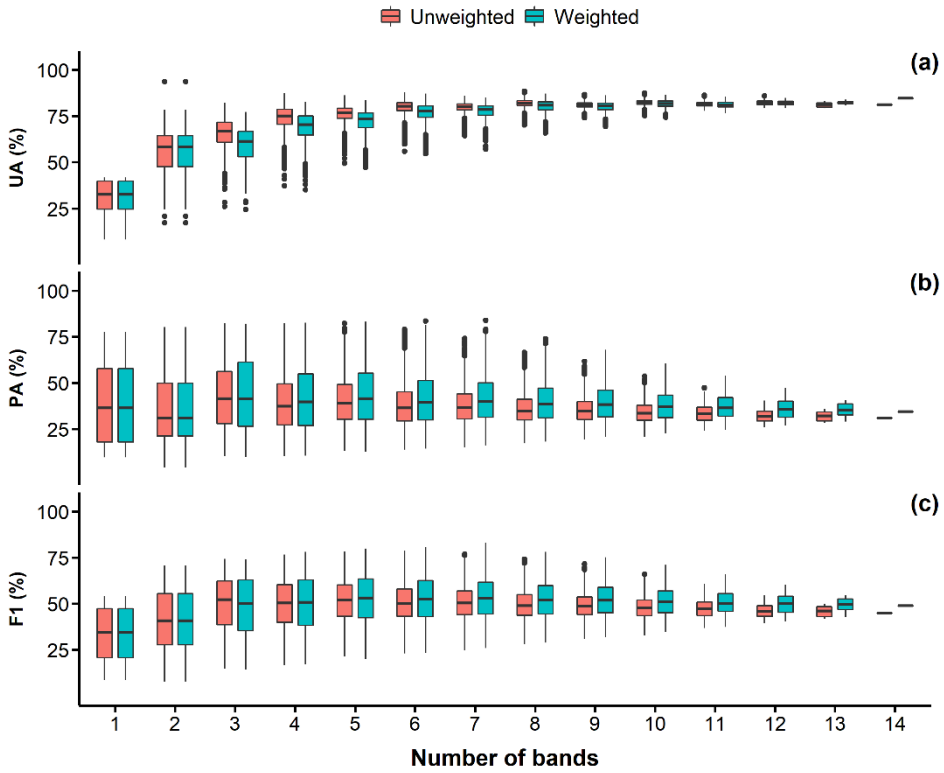

Figure 4.8. Distributions of each accuracy metric relative to all the unique combinations computed by including one to 14 bands in the CDMT algorithm: (**a**) user's accuracy (UA), (**b**) producer's accuracy (PA) and (**c**) F1 score. We also reported the effects on the distributions of accuracy metrics induced by weighting bands.

Table 4.2. Details relative to the maximum F1 score among all the unique combinations of weighted bands, with a length from one to 14. We also reported the corresponding user's and producer's accuracy and the bands included in the best performing combination.

Combination length (unique combinations)	**Maximum F1 (%)**	**UA (%)**	**PA (%)**	**Bands**
1 (14)	54.0	41.8	76.0	NDMI
2 (91)	70.8	65.7	76.7	SWIR2, NDMI
3 (364)	74.1	71.0	77.5	NDMI, TCW, TCA
4 (1001)	78.1	79.5	76.7	SWIR2, MSI, TCW, TCA
5 (2002)	79.9	79.3	80.4	SWIR1, NBR, MSI, TCW, TCA
6 (3003)	80.6	77.8	83.6	SWIR2, NDMI, NBR, MSI, TCW, TCA
7 (3432)	83.1	82.4	83.9	SWIR1, SWIR2, NDMI, NBR, MSI, TCW, TCA
8 (3003)	78.0	82.9	73.7	SWIR1, SWIR2, NDMI, NBR, MSI, TCG, TCW, TCA
9 (2002)	75.2	84.1	67.9	NIR, SWIR1, SWIR2, NDMI, NBR, MSI, TCG, TCW, TCA
10 (1001)	71.0	86.1	60.5	NIR, SWIR1, SWIR2, NDVI, NDMI, NBR, MSI, TCG, TCW, TCA
11 (364)	66.0	85.2	53.9	BLUE, NIR, SWIR1, SWIR2, NDVI, NDMI, NBR, MSI, TCG, TCW, TCA

12 (91)	60.4	83.7	47.2	BLUE, NIR, SWIR1, SWIR2, NDVI, NDMI, NBR, MSI, TCB, TCG, TCW, TCA
13 (14)	54.7	83.1	40.8	BLUE, RED, NIR, SWIR1, SWIR2, NDVI, NDMI, NBR, MSI, TCB, TCG, TCW, TCA
14 (1)	49.0	84.7	34.4	BLUE, RED, Green, NIR, SWIR1, SWIR2, NDVI, NDMI, NBR, MSI, TCB, TCG, TCW, TCA

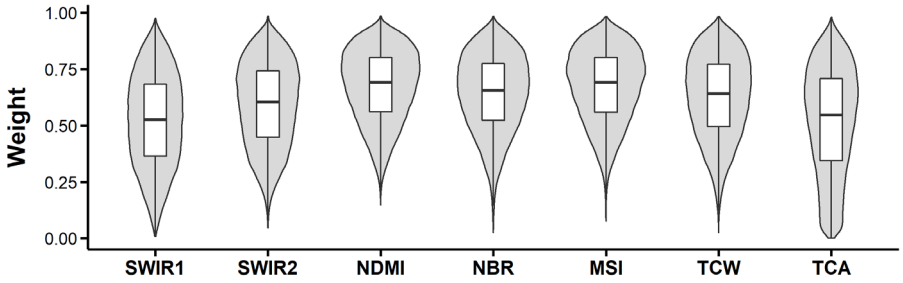

Figure 4.9. Distribution of weights assigned to each band considering the best performing combination in terms of F1 score. We randomly sampled 200000 pixels among those disturbed in the study area.

Table 4.3. Number of times each weighted band was included in the best performing combination in terms of F1 score, irrespective of their length.

Band	**Number of times**	**Rank**
NDMI	12	1
TCW	12	1
TCA	12	1
SWIR2	11	2
MSI	11	2
NBR	10	3
SWIR1	9	4
TCG	7	5
NIR	6	6
NDVI	5	7
Blue	4	8
TCB	3	9
Red	2	10
Green	1	11

4.3.4 Disturbance detection and severity assessment in the Aosta Valley

CDMT detected forest patches that were disturbed either by discrete disturbance agents like fire and wind or associated with adverse climate conditions, such as exceptional drought and heatwaves (Figure 4.10, Figure 4.11). Climate-induced canopy mortality following a particularly unfavourable year produced heterogeneous spectral signals. In particular, CDMT detected non-stand-replacing disturbances either as abrupt or gradual events, depending on their effect on linear trends in multispectral time series (Figure 4.11). Nonetheless, a qualitative assessment of the disturbed patches detected by CDMT through a comparison with high-resolution imagery highlighted good spatial agreement between these data (e.g. Figure 4.11).

We converted the synthetic spectral change magnitude derived from the best performing combination in terms of F1 score (Table 4.2) into disturbance severity. We reported this latter as the predicted probability for a given pixel of being disturbed by a non-stand-replacing or stand-replacing event (Figure 4.12). The distribution of disturbance severity values among training pixels showed that this approach effectively discriminated between non-stand-replacing and stand-replacing disturbances (Figure S4.1). The binary classification achieved an overall accuracy of 74.8%. The user's and producer's accuracy were 76.1% and 72.3% for non-stand-replacing disturbances, respectively. For stand-replacing disturbances, these metrics achieved values equal to 73.6% and 77.3%, respectively. The ample range of values assumed by disturbance severity, i.e. 0.1 – 1, highlighted the sensitivity of CDMT to a wide spectrum of disturbance severities (Figure 4.13).

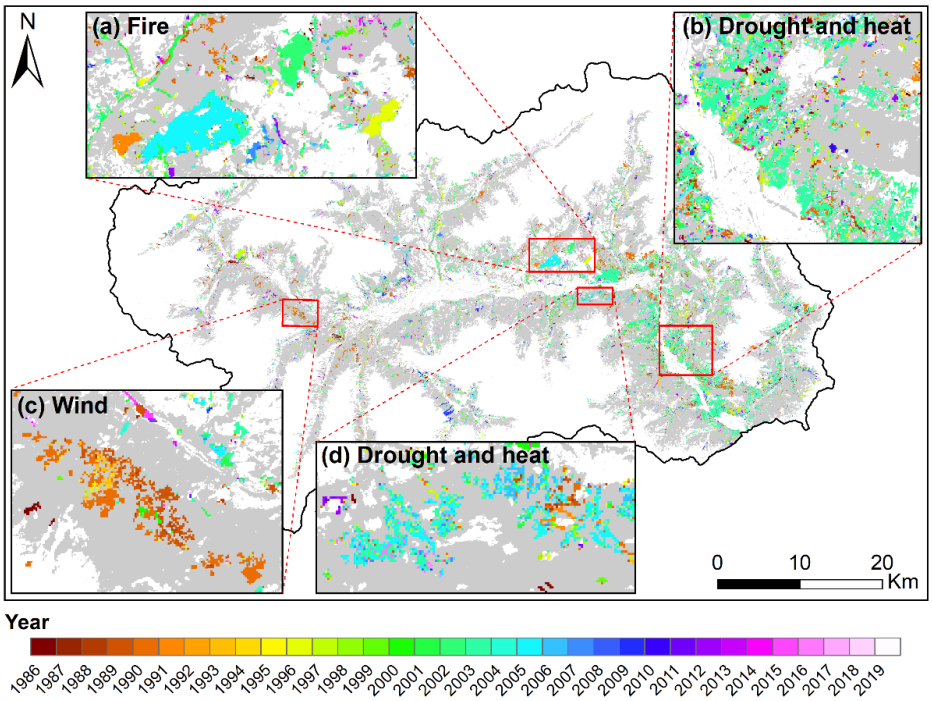

Figure 4.10. Map of the study area depicting the year when CDMT detected the maximum synthetic spectral change magnitude. Inset maps (**a**-**d**) show geographic areas where forests were disturbed mainly by a single disturbance agent. Forested areas from the Dominant Leaf Type 2018 layer (European Environmental Agency, 2020) are depicted in grey. The exceptional drought and heatwave occurred in 2003 caused extensive mortality of tree canopies in stands dominated by broadleaves, e.g. downy oak (**b**), and conifers, e.g. Scots pine (**d**). We masked non-forest pixels and applied a minimum mapping unit equal to 5 Landsat pixels (0.45 hectares).

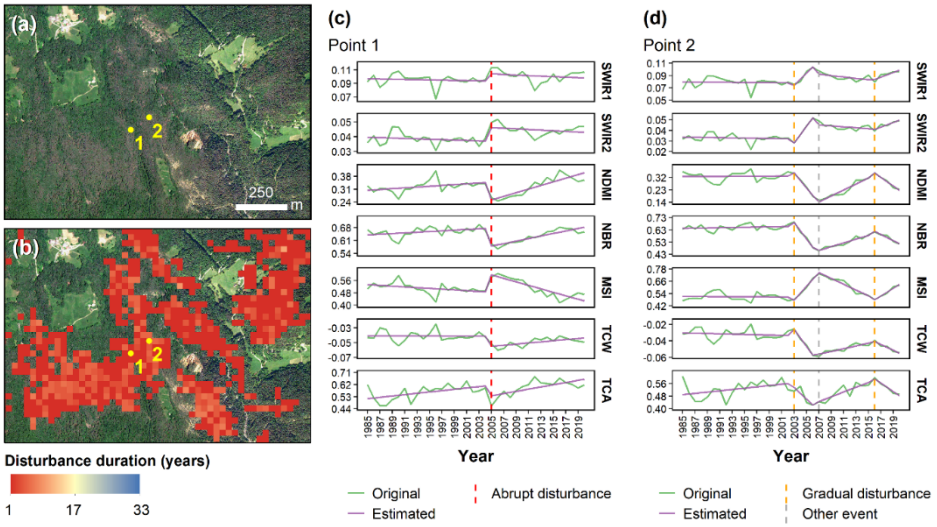

Figure 4.11. Example of a forest stand dominated by Scots pine that was disturbed by the exceptional drought and heat occurred in 2003 (spatial subset from Figure 4.10d). The high-resolution satellite image from Bing was acquired in June 2014 and displayed brown patches associated with diffuse canopy mortality (**a**). The disturbance duration map (**b**) indicates that CDMT detected abrupt or gradual changes in linear trends. These differences were evident when looking at multispectral time series of two near pixels: one experienced an abrupt change in 2005 (**c**) while the other experienced a decline since 2003 (**d**). We masked non-forest pixels and applied a minimum mapping unit equal to 5 Landsat pixels (0.45 hectares).

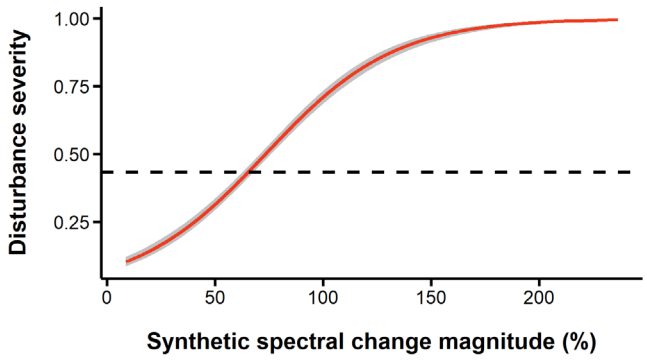

Figure 4.12. The logistic regression model used for converting synthetic spectral change magnitude into disturbance severity. This latter corresponds to the probability for a given pixel of being disturbed by a non-stand replacing or a stand-replacing event. The dashed line indicates the optimal a posteriori threshold discriminating between the two severity classes.

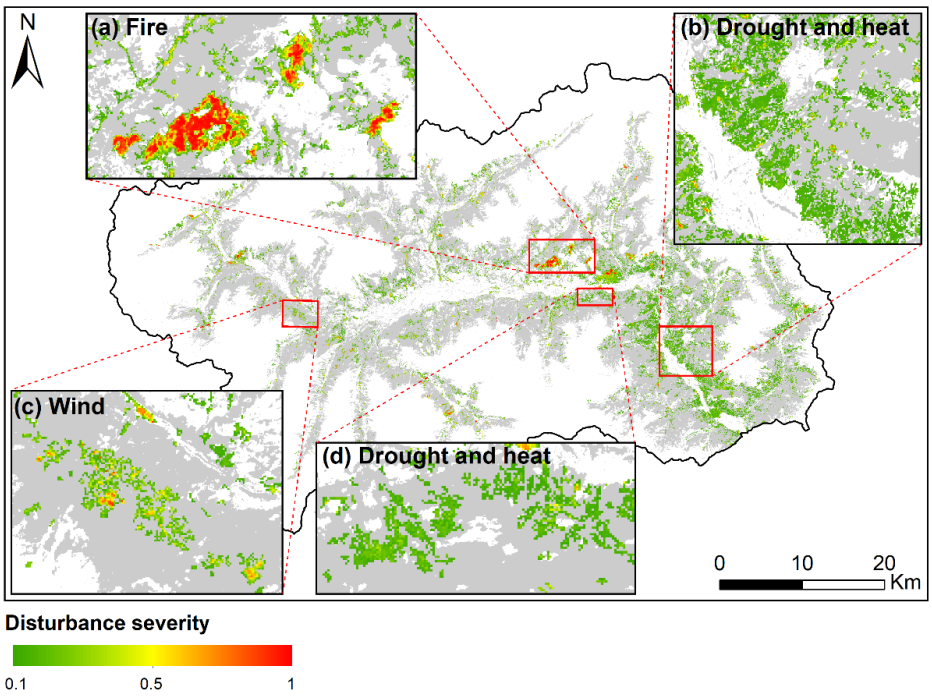

Figure 4.13. Map of the study area depicting the maximum disturbance severity occurred within the analysis period (1986 – 2019). Disturbance severity is expressed as the probability for a pixel of being disturbed by a non-stand replacing or a stand-replacing event. Inset maps (**a**-**d**) show geographic areas where forests were disturbed mainly by a single disturbance agent. The exceptional drought and heatwave occurred in 2003 impacted extensive forest patches and was characterised by very low severity (**b**, **d**). We masked non-forest pixels and applied a minimum mapping unit equal to 5 Landsat pixels (0.45 hectares).

4.3.5 Trends in forest disturbances in the Aosta Valley

We computed yearly disturbance rates by first summing the area of all disturbed pixels within the forest mask in a single year and then dividing by the total forest area (Section 2.9). The average yearly disturbance rate was 0.3 ± 0.64% standard deviation, considering the whole analysis period (Figure 4.14). The average yearly disturbance rate in the late 20th century (1986-2000) was equal to 0.19 ± 0.27% standard deviation. The most critical years within this period were 1990, 1997 and 1989, with a disturbance rate equal to 1.01%, 0.6% and 0.27%, respectively. Notably, the average yearly disturbance rate in the early 21st century (2001-2019) increased to 0.36 ± 0.8% standard deviation. During these years, the disturbance rate reached a peak in 2003 (3.7%), followed by 2001 (0.62%), 2002 (0.52%) and 2009 (0.43%).

Regarding disturbance severity, the average proportion between non-stand-replacing and stand-replacing disturbances in the late 20th century was 95.6% to 4.4% (Figure 4.15). In the early 21st century, stand-replacing disturbances increased on average by ~ 0.5%, i.e. to 4.9% of the total disturbed area. Overall, the proportion of stand-replacing disturbances remained somewhat stable throughout the whole analysis period, and the average was equal to 4.7 ± 3.7% standard deviation.

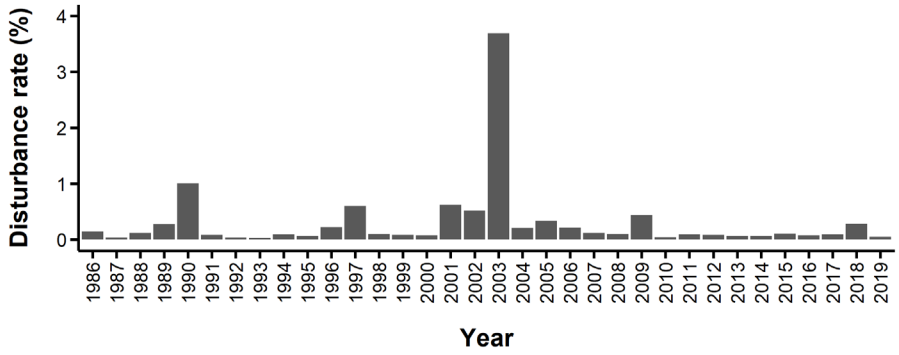

Figure 4.14. Yearly disturbance rate in the Aosta Valley region between 1986 and 2019. We included both non-stand replacing and stand-replacing disturbances.

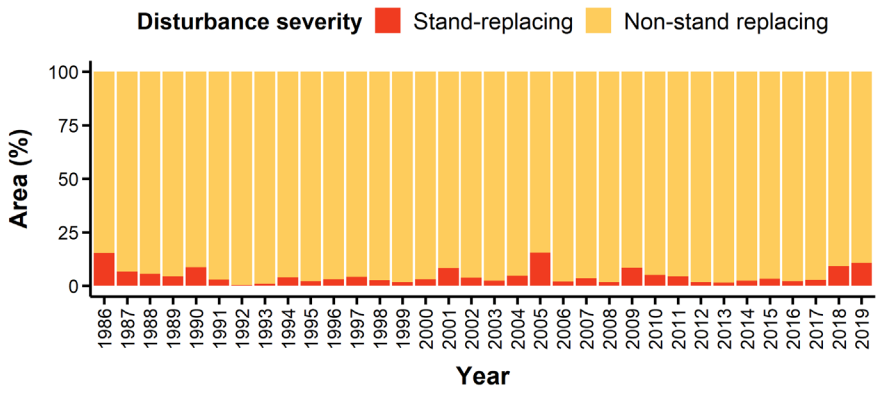

Figure 4.15. The yearly proportion of stand-replacing and non-stand replacing disturbances between 1986 and 2019.

4.4 Discussion

4.4.1 Assessment of the algorithm

When we employed univariate time series, the performances of CDMT in terms of user's and producer's accuracy were highly imbalanced towards the latter (Figure 4.6, Figure 4.8, Table 4.2). The low user's accuracy highlighted the difficulty of CDMT to distinguish between subtle spectral changes associated with low-severity forest disturbances and noise in annual Landsat time series in a similar way to other automated algorithms (Cohen et al., 2020, 2018, 2017). Conversely, CDMT detected low-severity and gradual disturbances, attaining a relatively high producer's accuracy, e.g. 76% using NDMI (Table 4.2). This result is likely related to the bottom-up, i.e. agglomerative, approach employed by the HiTS procedure (Section 4.2.6). When applied for the segmentation of various types of signals, bottom-up approaches outperform those based on sliding windows and top-down algorithms (Keogh et al., 2004). For instance, the C2C algorithm (Hermosilla et al., 2015b) is based on a bottom-up approach to segment annual Landsat time series. Considering the HiTGUW transform (i.e. the first stage of the HiTS procedure), the outperformance comes from its bottom-up nature, focusing on local features in its early stages before identifying global

features, which enables HiTS to perform well in detecting abrupt local changes, including point anomalies. To be specific, the ability of HiTS to detect point anomalies is obtained in the process of building an adaptive wavelet basis by recursively applying the conditionally orthonormal transformations.

Several studies, such as Cohen et al. (2017) and Healey et al. (2018), explored the differences between disturbance maps derived from diverse Landsat time series-based algorithms by considering a broad range of severities. They highlighted a tendency of those algorithms based on the widely-used temporal segmentation methods like LandTrendr (Kennedy et al., 2018, 2010) and VeRDET (Hughes et al., 2017) to achieve a relatively high producer's accuracy at the cost of a somewhat low user's accuracy. Conversely, algorithms relying on another popular mathematical approach, the statistical boundary, produced heterogeneous results regarding disturbance detection accuracy (Cohen et al., 2017; Healey et al., 2018). In particular, CCDC (Zhu and Woodcock, 2014) had a lower producer's accuracy and a higher user's accuracy compared to segmentation algorithms. On the contrary, EWMACD (Exponentially Weighted Moving Average Change Detection; Brooks et al., 2014) behaved similarly to segmentation algorithms as it was explicitly designed to detect non-stand-replacing disturbances.

In the multivariate setting, the user's accuracy of CDMT increased to the level of the producer's accuracy (Figure 4.8, Table 4.2). Similarly, the secondary classification model employed to fuse results of multispectral ensembles primarily increased the user's accuracy of LandTrendr (Cohen et al., 2020, 2018; Senf and Seidl, 2020). As highlighted by the F1 score (Figure 4.8c, Table 4.2), the balance between user's and producer's accuracy peaked when we included four to seven bands in multispectral time series. This result is consistent with Cohen et al. (2020, 2018), who found that balanced errors reached an asymptote between four to seven bands using multispectral ensembles built with outputs of LandTrendr. Moreover, it also allowed the algorithm to maximise the producer's accuracy as the spectral change filter designed to eliminate spurious breaks, i.e. increase the user's accuracy, was unnecessary (Cohen et al., 2020, 2018). Moving

from univariate to multivariate time series, the producer's accuracy of CDMT increased up to ~ 8% (Table 4.2). This was likely related to band-specific weights (Figure 4.9), as CDMT prioritised those bands that provided the best performances when employed alone (Figure 4.6).

Unlike multispectral ensembles, CDMT does not require collecting a comprehensive set of disturbance samples for training a secondary classification model, e.g. random forest. Moreover, the statistical approach employed by CDMT, i.e. the modified HiTS procedure, allows the algorithm to exploit the multispectral information during every stage of the analysis (Section 4.2.6). The HiTGUW transform, for example, builds an adaptive unbalanced wavelet basis by evaluating deviations from linearity occurring in every input band at the same time interval. This feature ensures that the temporal segmentation is unique among bands. Conversely, the most widely-used multivariate algorithms like CCDC (Zhu and Woodcock, 2014) or COLD (Zhu et al., 2019) fit harmonic models to the time series in parallel, i.e. separately, and then aggregate the results across bands to identify changepoints.

The increase in the user's accuracy provided by multispectral time series is likely related to a decreased sensitivity of CDMT towards the band-dependent noise (Figure 4.5b). The presence of this latter clearly emerged from the results of the impulsive noise filter, which increased the user's accuracy unevenly among bands (Figure 4.6, Table S4.1). For example, cirrus clouds in Landsat imagery alter surface reflectance heterogeneously among wavelengths, with a lower impact on the SWIR bands than on the others (Qiu et al., 2020). Conversely, forest disturbances and band-independent noise typically caused dense changes in the time series (Figure 4.5, Figure 4.11), though the latter were effectively removed by the impulsive noise filter (Figure 4.6, Table S4.1).

In our study, the best performing bands in the univariate setting were based on the SWIR bands, i.e. MSI, NDMI and NBR, followed by TCW, SWIR2 band and TCA (Figure 4.6, Table S4.1). The effectiveness of those bands contrasting NIR and SWIR wavelengths for forest disturbance detection was reported by several studies based on different change detection algorithms (Cohen et al., 2018; Hislop

et al., 2019; Schultz et al., 2016). The combination that produced the highest accuracy in terms of F1 score included the top-six best performing bands taken individually plus the SWIR1 (Table 4.2). Apart from MSI, which was not included in their study, the top-six bands in terms of DSNR metric in Cohen et al. (2018) corresponded to those in the best performing combination with seven bands (Table 4.2). Notably, the rank of these bands based on the median band-specific weight assigned by CDMT (Figure 4.9, Table S4.2) coincided with that based on the median DNSR. The most frequent bands in the top-performing combinations of every length were NDMI, TCW and TCA (Table 4.3). Following the classification proposed by Cohen et al. (2020), NDMI and TCW belong to SWIR bands, while TCA belongs to NIR bands. With reference to their study and others (DeVries et al., 2016; Schultz et al., 2016), our results support the prevailing importance of SWIR bands over NIR bands and their complementarity for detecting forest disturbance using Landsat time series.

Concerning the parametrisation of the HiTS procedure, the performances of CDMT showed that parameter *C*, which controls the change threshold (Equation 4), had a relatively low influence on the detection of changepoints (Figure S4.1, Table S4.3). Yet, decreasing *C* values from its recommended value, i.e. 1.2, to 1 primarily reduced the user's accuracy, as spurious changepoints were detected more frequently. This suggests the utility of parameter *C* in limiting the influence of inter-annual noise. Moreover, as the HiTS procedure normalises each time series X_i by the standard deviation (Equation 3), its sensitivity to disturbances likely depends on the noise level in the time series.

4.4.2 Disturbance severity assessment and trends in forest disturbances

Disturbance severity gave an ecological meaning to the synthetic spectral change magnitude. Discerning between non-stand-replacing and stand-replacing events was an effective strategy to cope with different disturbance agents, as proposed in other studies (Cohen et al., 2016; Hermosilla et al., 2015a; Senf and Seidl, 2020). In this sense, both classes attained relatively high accuracy, i.e. user's and

producer's accuracy higher than 70%. The relationship between spectral change magnitude and disturbance severity was nonlinear, particularly for stand-replacing events (Figure 4.12). This is consistent with other studies that employed remotely sensed change metrics to infer disturbance severity, e.g. Morresi et al. (2022).

Our results indicated an increase in both disturbance rate and severity during the first two decades of the 21st century compared to the late 20th century (Figure 4.14, Figure 4.15). An increase in tree canopy mortality during the early 21st century in Europe was also highlighted in other studies (Seidl et al., 2014; Senf et al., 2021, 2018). Considering the whole analysis period, higher disturbance rates during certain years (Figure 4.14) were associated with the co-occurrence of discrete events, such as windthrows and wildfires in 1990 or drought and heatwaves in 2003 (Figure 4.10, Figure 4.11). In 1990, the winter storm Vivian severely impacted forests across the Alps (Wohlgemuth et al., 2017), including those in the Aosta Valley (Bottero et al., 2013). In the same year, seven wildfires occurred in the region, two of which had an extent larger than 300 hectares. The exceptional drought and heat that occurred in Europe during the summer of 2003 (Rebetez et al., 2006) heavily decreased the primary productivity of both broadleaved and conifer forests, thus impairing their carbon sequestration capacity (Ciais et al., 2005). Moreover, this event triggered diffuse mortality of Scots pine in many parts of Europe (Allen et al., 2010), including the Aosta Valley region (Vacchiano et al., 2012). Our results showed that, albeit non-stand-replacing, this anomalous event affected forest stands by an unprecedented extension (Figure 4.14). Moreover, CDMT captured the heterogeneity of the mortality response to drought and heat from different groups of Scots pine individuals, e.g. either delayed and abrupt or timely and gradual (Figure 4.11). Delayed mortality of Scots pine after drought has been observed after several years or decades as an effect of crown defoliation (Bigler et al., 2006). Among the consequences of such extreme droughts, Rouault et al. (2006) observed an increased susceptibility of various tree species, including Scots pine, to attacks from secondary pest insects. Moreover, Camarero et al. (2015) reported an

increase in the incidence of blue-stain fungi in the wood of Scots Pine. In the long-term, drought-induced decline of Scots pine population leads this species to disappear (Camarero et al., 2015) and being replaced by different tree species, e.g. downy oak (Rigling et al., 2013).

4.5 Conclusions

The CDMT algorithm offers new opportunities for automating forest change detection thanks to a novel multivariate statistical method for segmenting annual Landsat time series. While providing similar advantages as multispectral ensembles based on univariate algorithms, CDMT provides a more direct approach for exploiting multispectral time series. Here we focused on assessing its capabilities for disturbance detection over a wide range of severities, from non-stand-replacing to stand-replacing. However, like similar algorithms, CDMT can detect changes in spectral trends associated with growth and post-disturbance recovery. Testing the algorithm in a highly mountainous area, characterised by complex topography and data scarcity due to persistent snow and cloud cover, allowed us to explore its potential. In particular, we highlighted the advantages offered by the exploitation of the complete spectral information provided by Landsat imagery for disturbance detection. The low requirements in terms of parametrisation and the robust statistical approach should ease the applicability of CDMT in forest ecosystems different from those in our study area. Moreover, the methods implemented in CDMT are general enough to be employed with satellite time series from different optical sensors, e.g. the Multispectral Instrument onboard Sentinel-2 satellites.

Data availability statement

The R code of the CDMT algorithm is publicly available via the GitHub repository of the first author, https://github.com/donatomorresi/cdmt.

Acknowledgments

We acknowledge the Corpo Forestale (Forest Service) of the Aosta Valley Autonomous Region for providing data on forest disturbances. In particular, we wish to thank Giancarlo Cesti of the Forest fire Service and Ivan Rollet of the Forest health monitoring Service. Moreover, we acknowledge the U.S. Geological Survey for distributing Landsat imagery and Dr. David Frantz for providing the Framework for Operational Radiometric Correction for Environmental monitoring (FORCE) software.

References

Allen, C.D., Breshears, D.D., McDowell, N.G., 2015. On underestimation of global vulnerability to tree mortality and forest die-off from hotter drought in the Anthropocene. Ecosphere 6, 1–55. https://doi.org/10.1890/ES15-00203.1

Allen, C.D., Macalady, A.K., Chenchouni, H., Bachelet, D., McDowell, N., Vennetier, M., Kitzberger, T., Rigling, A., Breshears, D.D., Hogg, E.H. (Ted., Gonzalez, P., Fensham, R., Zhang, Z., Castro, J., Demidova, N., Lim, J.H., Allard, G., Running, S.W., Semerci, A., Cobb, N., 2010. A global overview of drought and heat-induced tree mortality reveals emerging climate change risks for forests. For. Ecol. Manage. 259, 660–684. https://doi.org/10.1016/j.foreco.2009.09.001

Andrus, R.A., Chai, R.K., Harvey, B.J., Rodman, K.C., Veblen, T.T., 2021. Increasing rates of subalpine tree mortality linked to warmer and drier summers. J. Ecol. 109, 2203–2218. https://doi.org/10.1111/1365-2745.13634

Banskota, A., Kayastha, N., Falkowski, M.J., Wulder, M.A., Froese, R.E., White, J.C., 2014. Forest Monitoring Using Landsat Time Series Data: A Review. Can. J. Remote Sens. 40, 362–384. https://doi.org/10.1080/07038992.2014.987376

Bardwell, L., Fearnhead, P., Eckley, I.A., Smith, S., Spott, M., 2019. Most Recent

Changepoint Detection in Panel Data. Technometrics 61, 88–98. https://doi.org/10.1080/00401706.2018.1438926

Bengtsson, H., 2021. matrixStats: Functions that Apply to Rows and Columns of Matrices (and to Vectors).

Bigler, C., Bräker, O.U., Bugmann, H., Dobbertin, M., Rigling, A., 2006. Drought as an Inciting Mortality Factor in Scots Pine Stands of the Valais, Switzerland 9, 330–343. https://doi.org/10.1007/sl0021-005-0126-2

Bottero, A., Garbarino, M., Long, J.N., Motta, R., 2013. The interacting ecological effects of large-scale disturbances and salvage logging on montane spruce forest regeneration in the western European Alps. For. Ecol. Manage. 292, 19–28. https://doi.org/10.1016/j.foreco.2012.12.021

Brooks, E.B., Wynne, R.H., Thomas, V.A., Blinn, C.E., Coulston, J.W., 2014. On-the-fly massively multitemporal change detection using statistical quality control charts and landsat data. IEEE Trans. Geosci. Remote Sens. 52, 3316–3332. https://doi.org/10.1109/TGRS.2013.2272545

Brown, R.L., Durbin, J., Evans, J.M., 1975. Techniques for Testing the Constancy of Regression Relationships Over Time. J. R. Stat. Soc. Ser. B 37, 149–163. https://doi.org/10.1111/j.2517-6161.1975.tb01532.x

Bullock, E.L., Woodcock, C.E., Holden, C.E., 2020. Improved change monitoring using an ensemble of time series algorithms. Remote Sens. Environ. 238, 111165. https://doi.org/10.1016/j.rse.2019.04.018

Camarero, J.J., Gazol, A., Sangüesa-Barreda, G., Oliva, J., Vicente-Serrano, S.M., 2015. To die or not to die: Early warnings of tree dieback in response to a severe drought. J. Ecol. 103, 44–57. https://doi.org/10.1111/1365-2745.12295

Cho, H., Fryzlewicz, P., 2015. Multiple-change-point detection for high dimensional time series via sparsified binary segmentation. J. R. Stat. Soc. Ser. B Stat. Methodol. 77, 475–507. https://doi.org/10.1111/rssb.12079

Cho, H., Kirch, C., 2020. Data segmentation algorithms: Univariate mean change and beyond. Econom. Stat. https://doi.org/10.1016/j.ecosta.2021.10.008

Ciais, P., Reichstein, M., Viovy, N., Granier, A., Ogée, J., Allard, V., Aubinet,

M., Buchmann, N., Bernhofer, C., Carrara, A., Chevallier, F., De Noblet, N., Friend, A.D., Friedlingstein, P., Grünwald, T., Heinesch, B., Keronen, P., Knohl, A., Krinner, G., Loustau, D., Manca, G., Matteucci, G., Miglietta, F., Ourcival, J.M., Papale, D., Pilegaard, K., Rambal, S., Seufert, G., Soussana, J.F., Sanz, M.J., Schulze, E.D., Vesala, T., Valentini, R., 2005. Europe-wide reduction in primary productivity caused by the heat and drought in 2003. Nature 437, 529–533. https://doi.org/10.1038/nature03972

Cohen, W.B., Healey, S.P., Yang, Z., Stehman, S. V., Brewer, C.K., Brooks, E.B., Gorelick, N., Huang, C., Hughes, M.J., Kennedy, R.E., Loveland, T.R., Moisen, G.G., Schroeder, T.A., Vogelmann, J.E., Woodcock, C.E., Yang, L., Zhu, Z., 2017. How Similar Are Forest Disturbance Maps Derived from Different Landsat Time Series Algorithms? Forests 8, 1–19. https://doi.org/10.3390/f8040098

Cohen, W.B., Healey, S.P., Yang, Z., Zhu, Z., Gorelick, N., 2020. Diversity of algorithm and spectral band inputs improves landsat monitoring of forest disturbance. Remote Sens. 12, 1–15. https://doi.org/10.3390/rs12101673

Cohen, W.B., Yang, Z., Healey, S.P., Kennedy, R.E., Gorelick, N., 2018. A LandTrendr multispectral ensemble for forest disturbance detection. Remote Sens. Environ. 205, 131–140. https://doi.org/10.1016/j.rse.2017.11.015

Cohen, W.B., Yang, Z., Kennedy, R., 2010. Detecting trends in forest disturbance and recovery using yearly Landsat time series: 2. TimeSync - Tools for calibration and validation. Remote Sens. Environ. 114, 2911–2924. https://doi.org/10.1016/j.rse.2010.07.010

Cohen, W.B., Yang, Z., Stehman, S. V., Schroeder, T.A., Bell, D.M., Masek, J.G., Huang, C., Meigs, G.W., 2016. Forest disturbance across the conterminous United States from 1985-2012: The emerging dominance of forest decline. For. Ecol. Manage. 360, 242–252. https://doi.org/10.1016/j.foreco.2015.10.042

Coops, N.C., Shang, C., Wulder, M.A., White, J.C., Hermosilla, T., 2020. Change in forest condition: Characterizing non-stand replacing disturbances using

time series satellite imagery. For. Ecol. Manage. 474, 118370. https://doi.org/10.1016/j.foreco.2020.118370

Crist, E.P., 1985. A TM tasseled cap equivalent transformation for reflectance factor data. Remote Sens. Environ. 17, 301–306.

DeVries, B., Pratihast, A.K., Verbesselt, J., Kooistra, L., Herold, M., 2016. Characterizing Forest Change Using Community-Based Monitoring Data and Landsat Time Series. PLoS One 11, e0147121. https://doi.org/10.1371/journal.pone.0147121

Enikeeva, F., Harchaoui, Z., 2019. High-dimensional change-point detection under sparse alternatives. Ann. Stat. 47, 2051–2079. https://doi.org/10.1214/18-AOS1740

European Environmental Agency, 2020. Copernicus Land Monitoring Service – Dominant Leaf Type 2018 [WWW Document]. URL https://land.copernicus.eu/pan-european/high-resolution-layers/forests/dominant-leaf-type (accessed 1.6.21).

Foga, S., Scaramuzza, P.L., Guo, S., Zhu, Z., Dilley, R.D., Beckmann, T., Schmidt, G.L., Dwyer, J.L., Joseph Hughes, M., Laue, B., 2017. Cloud detection algorithm comparison and validation for operational Landsat data products. Remote Sens. Environ. 194, 379–390. https://doi.org/10.1016/j.rse.2017.03.026

Forzieri, G., Girardello, M., Ceccherini, G., Spinoni, J., Feyen, L., Hartmann, H., Beck, P.S.A., Camps-Valls, G., Chirici, G., Mauri, A., Cescatti, A., 2021. Emergent vulnerability to climate-driven disturbances in European forests. Nat. Commun. 12, 1–12. https://doi.org/10.1038/s41467-021-21399-7

Frantz, D., 2019. FORCE-Landsat + Sentinel-2 analysis ready data and beyond. Remote Sens. 11. https://doi.org/10.3390/rs11091124

Frantz, D., Röder, A., Stellmes, M., Hill, J., 2016. An operational radiometric landsat preprocessing framework for large-area time series applications. IEEE Trans. Geosci. Remote Sens. 54, 3928–3943. https://doi.org/10.1109/TGRS.2016.2530856

Freeman, E.A., Moisen, G., 2008a. PresenceAbsence: An R package for

PresenceAbsence analysis. J. Stat. Softw. 23, 1–31. https://doi.org/10.18637/jss.v023.i11

Freeman, E.A., Moisen, G.G., 2008b. A comparison of the performance of threshold criteria for binary classification in terms of predicted prevalence and kappa. Ecol. Modell. 217, 48–58. https://doi.org/10.1016/j.ecolmodel.2008.05.015

García, M.J.L., Caselles, V., 1991. Mapping burns and natural reforestation using thematic Mapper data. Geocarto Int. 6, 31–37. https://doi.org/10.1080/10106049109354290

Groen, J.J.J., Kapetanios, G., Price, S., 2013. Multivariate methods for monitoring structural change. J. Appl. Econom. 28, 250–274. https://doi.org/10.1002/jae.1272

Grundy, T., Killick, R., Mihaylov, G., 2020. High-dimensional changepoint detection via a geometrically inspired mapping. Stat. Comput. 30, 1155–1166. https://doi.org/10.1007/s11222-020-09940-y

Hall, A.R., Osborn, D.R., Sakkas, N., 2013. Inference on structural breaks using information criteria. Manchester Sch. 81, 54–81. https://doi.org/10.1111/manc.12017

Hampel, F.R., 1974. The influence curve and its role in robust estimation. J. Am. Stat. Assoc. 69, 383–393. https://doi.org/10.1080/01621459.1974.10482962

Hansen, M.C., Potapov, P. V., Moore, R., Hancher, M., Turubanova, S.A., Tyukavina, A., Thau, D., Stehman, S. V., Goetz, S.J., Loveland, T.R., Kommareddy, A., Egorov, A., Chini, L., Justice, C.O., Townshend, J.R.G., 2013. High-resolution global maps of 21st-century forest cover change. Science (80-.). 342, 850–853. https://doi.org/10.1126/science.1244693

Healey, S.P., Cohen, W.B., Yang, Z., Kenneth Brewer, C., Brooks, E.B., Gorelick, N., Hernandez, A.J., Huang, C., Joseph Hughes, M., Kennedy, R.E., Loveland, T.R., Moisen, G.G., Schroeder, T.A., Stehman, S. V., Vogelmann, J.E., Woodcock, C.E., Yang, L., Zhu, Z., 2018. Mapping forest change using stacked generalization: An ensemble approach. Remote Sens.

Environ. 204, 717–728. https://doi.org/10.1016/j.rse.2017.09.029

Hermosilla, T., Wulder, M.A., White, J.C., Coops, N.C., Hobart, G.W., 2015a. Regional detection, characterization, and attribution of annual forest change from 1984 to 2012 using Landsat-derived time-series metrics. Remote Sens. Environ. 170, 121–132. https://doi.org/10.1016/j.rse.2015.09.004

Hermosilla, T., Wulder, M.A., White, J.C., Coops, N.C., Hobart, G.W., 2015b. An integrated Landsat time series protocol for change detection and generation of annual gap-free surface reflectance composites. Remote Sens. Environ. 158, 220–234. https://doi.org/10.1016/j.rse.2014.11.005

Hijmans, R.J., 2022. terra: Spatial Data Analysis.

Hislop, S., Jones, S., Soto-Berelov, M., Skidmore, A., Haywood, A., Nguyen, T.H., 2019. A fusion approach to forest disturbance mapping using time series ensemble techniques. Remote Sens. Environ. 221, 188–197. https://doi.org/10.1016/j.rse.2018.11.025

Hughes, M.J., Kaylor, S.D., Hayes, D.J., 2017. Patch-based forest change detection from Landsat time series. Forests 8, 1–22. https://doi.org/10.3390/f8050166

Hunt Jr, E.R., Rock, B.N., 1989. Detection of changes in leaf water content using near-and middle-infrared reflectances. Remote Sens. Environ. 30, 43–54.

Jirak, M., 2015. Uniform change point tests in high dimension. Ann. Stat. 43, 2451–2483. https://doi.org/10.1214/15-AOS1347

Johnstone, J.F., Allen, C.D., Franklin, J.F., Frelich, L.E., Harvey, B.J., Higuera, P.E., Mack, M.C., Meentemeyer, R.K., Metz, M.R., Perry, G.L.W., Schoennagel, T., Turner, M.G., 2016. Changing disturbance regimes, ecological memory, and forest resilience. Front. Ecol. Environ. 14, 369–378. https://doi.org/10.1002/fee.1311

Ju, J., Roy, D.P., 2008. The availability of cloud-free Landsat ETM+ data over the conterminous United States and globally. Remote Sens. Environ. 112, 1196–1211. https://doi.org/10.1016/j.rse.2007.08.011

Kennedy, R.E., Andréfouet, S., Cohen, W.B., Gomez, C., Griffiths, P., Hais, M., Healey, S.P., Helmer, E.H., Hostert, P., Lyons, M.B., Meigs, G.W.,

Pflugmacher, D., Phinn, S.R., Powell, S.L., Scarth, P., Sen, S., Schroeder, T.A., Schneider, A., Sonnenschein, R., Vogelmann, J.E., Wulder, M.A., Zhu, Z., 2014. Bringing an ecological view of change to landsat-based remote sensing. Front. Ecol. Environ. 12, 339–346. https://doi.org/10.1890/130066

Kennedy, R.E., Yang, Z., Cohen, W.B., 2010. Detecting trends in forest disturbance and recovery using yearly Landsat time series: 1. LandTrendr - Temporal segmentation algorithms. Remote Sens. Environ. 114, 2897–2910. https://doi.org/10.1016/j.rse.2010.07.008

Kennedy, R.E., Yang, Z., Cohen, W.B., Pfaff, E., Braaten, J., Nelson, P., 2012. Spatial and temporal patterns of forest disturbance and regrowth within the area of the Northwest Forest Plan. Remote Sens. Environ. 122, 117–133. https://doi.org/10.1016/j.rse.2011.09.024

Kennedy, R.E., Yang, Z., Gorelick, N., Braaten, J., Cavalcante, L., Cohen, W.B., Healey, S., 2018. Implementation of the LandTrendr algorithm on Google Earth Engine. Remote Sens. 10, 1–10. https://doi.org/10.3390/rs10050691

Keogh, E., Chu, S., Hart, D., Pazzani, M., 2004. Segmenting Time Series: a Survey and Novel Approach 1–21. https://doi.org/10.1142/9789812565402_0001

Leverkus, A.B., Thorn, S., Gustafsson, L., Noss, R., Müller, J., Pausas, J.G., Lindenmayer, D.B., 2021. Environmental policies to cope with novel disturbance regimes–steps to address a world scientists' warning to humanity. Environ. Res. Lett. 16. https://doi.org/10.1088/1748-9326/abdc5a

Maeng, H., 2019. Adaptive Multiscale Approaches to Regression and Trend Segmentation. The London School of Economics and Political Science (LSE).

Maeng, H., Fryzlewicz, P., 2019. Detecting linear trend changes and point anomalies in data sequences. arXiv.

Mantero, G., Morresi, D., Marzano, R., Motta, R., Mladenoff, D.J., Garbarino, M., 2020. The influence of land abandonment on forest disturbance

regimes: a global review. Landsc. Ecol. 35, 2723–2744. https://doi.org/10.1007/s10980-020-01147-w

Marzo, T. De, Pflugmacher, D., Baumann, M., Lambin, E.F., Gasparri, I., Kuemmerle, T., De Marzo, T., Pflugmacher, D., Baumann, M., Lambin, E.F., Gasparri, I., Kuemmerle, T., 2021. Characterizing forest disturbances across the Argentine Dry Chaco based on Landsat time series. Int. J. Appl. Earth Obs. Geoinf. 98, 102310. https://doi.org/10.1016/j.jag.2021.102310

McDowell, N.G., Allen, C.D., Anderson-Teixeira, K., Aukema, B.H., Bond-Lamberty, B., Chini, L., Clark, J.S., Dietze, M., Grossiord, C., Hanbury-Brown, A., Hurtt, G.C., Jackson, R.B., Johnson, D.J., Kueppers, L., Lichstein, J.W., Ogle, K., Poulter, B., Pugh, T.A.M., Seidl, R., Turner, M.G., Uriarte, M., Walker, A.P., Xu, C., 2020. Pervasive shifts in forest dynamics in a changing world. Science (80-.). 368. https://doi.org/10.1126/science.aaz9463

Millar, C.I., Stephenson, N.L., 2015. Temperate forest health in an era of emerging megadisturbance. Science (80-.). 349, 823–826. https://doi.org/10.1126/science.aaa9933

Morresi, D., Marzano, R., Lingua, E., Motta, R., Garbarino, M., 2022. Mapping burn severity in the western Italian Alps through phenologically coherent reflectance composites derived from Sentinel-2 imagery. Remote Sens. Environ. 269. https://doi.org/10.1016/j.rse.2021.112800

Olofsson, P., Foody, G.M., Herold, M., Stehman, S. V., Woodcock, C.E., Wulder, M.A., 2014. Good practices for estimating area and assessing accuracy of land change. Remote Sens. Environ. 148, 42–57. https://doi.org/10.1016/j.rse.2014.02.015

Park, C., Kim, H., Wang, M., 2019. Investigation of finite-sample properties of robust location and scale estimators. Commun. Stat. Simul. Comput. 0, 1–27. https://doi.org/10.1080/03610918.2019.1699114

Powell, S.L., Cohen, W.B., Healey, S.P., Kennedy, R.E., Moisen, G.G., Pierce, K.B., Ohmann, J.L., 2010. Quantification of live aboveground forest biomass dynamics with Landsat time-series and field inventory data: A

comparison of empirical modeling approaches. Remote Sens. Environ. 114, 1053–1068. https://doi.org/10.1016/j.rse.2009.12.018

Qiu, S., Zhu, Z., Woodcock, C.E., 2020. Cirrus clouds that adversely affect Landsat 8 images : What are they and how to detect them ? Remote Sens. Environ. 246, 111884. https://doi.org/10.1016/j.rse.2020.111884

Rebetez, M., Mayer, H., Dupont, O., Schindler, D., Gartner, K., Kropp, J.P., Menzel, A., 2006. Heat and drought 2003 in Europe: A climate synthesis. Ann. For. Sci. 63, 569–577. https://doi.org/10.1051/forest:2006043

Rigling, A., Bigler, C., Eilmann, B., Feldmeyer-Christe, E., Gimmi, U., Ginzler, C., Graf, U., Mayer, P., Vacchiano, G., Weber, P., Wohlgemuth, T., Zweifel, R., Dobbertin, M., 2013. Driving factors of a vegetation shift from Scots pine to pubescent oak in dry Alpine forests. Glob. Chang. Biol. 19, 229–240. https://doi.org/10.1111/gcb.12038

Roberts, D., Mueller, N., McIntyre, A., 2017. High-Dimensional Pixel Composites From Earth Observation Time Series. IEEE Trans. Geosci. Remote Sens. 55, 6254–6264. https://doi.org/10.1109/TGRS.2017.2723896

Rodman, K.C., Andrus, R.A., Veblen, T.T., Hart, S.J., 2021. Disturbance Detection in Landsat Time Series is Influenced By Tree Mortality Agent and Severity, Not By Prior Disturbance. Remote Sens. Environ. 254, 112244. https://doi.org/10.1016/j.rse.2020.112244

Rouault, G., Candau, J.N., Lieutier, F., Nageleisen, L.M., Martin, J.C., Warzée, N., 2006. Effects of drought and heat on forest insect populations in relation to the 2003 drought in Western Europe. Ann. For. Sci. 63, 613–624. https://doi.org/10.1051/forest:2006044

Rouse, J.W., Hass, R.H., Schell, J.A., Deering, D.W., 1973. Monitoring vegetation systems in the great plains with ERTS. Third Earth Resour. Technol. Satell. Symp. 1, 309–317. https://doi.org/citeulike-article-id:12009708

Roy, D.P., Li, J., Zhang, H.K., Yan, L., Huang, H., Li, Z., 2017a. Examination of Sentinel-2A multi-spectral instrument (MSI) reflectance anisotropy and the suitability of a general method to normalize MSI reflectance to nadir BRDF

adjusted reflectance. Remote Sens. Environ. 199, 25–38. https://doi.org/10.1016/j.rse.2017.06.019

Roy, D.P., Li, Z., Zhang, H.K., 2017b. Adjustment of sentinel-2 multi-spectral instrument (MSI) red-edge band reflectance to nadir BRDF adjusted reflectance (NBAR) and quantification of red-edge band BRDF effects. Remote Sens. 9. https://doi.org/10.3390/rs9121325

Schultz, M., Clevers, J.G.P.W., Carter, S., Verbesselt, J., Avitabile, V., Quang, H.V., Herold, M., 2016. Performance of vegetation indices from Landsat time series in deforestation monitoring. Int. J. Appl. Earth Obs. Geoinf. 52, 318–327. https://doi.org/10.1016/j.jag.2016.06.020

Seidl, R., 2014. The shape of ecosystem management to come: Anticipating risks and fostering resilience. Bioscience 64, 1159–1169. https://doi.org/10.1093/biosci/biu172

Seidl, R., Schelhaas, M.J., Rammer, W., Verkerk, P.J., 2014. Increasing forest disturbances in Europe and their impact on carbon storage. Nat. Clim. Chang. 4, 806–810. https://doi.org/10.1038/nclimate2318

Seidl, R., Spies, T.A., Peterson, D.L., Stephens, S.L., Hicke, J.A., 2016. Searching for resilience: Addressing the impacts of changing disturbance regimes on forest ecosystem services. J. Appl. Ecol. 53, 120–129. https://doi.org/10.1111/1365-2664.12511

Seidl, R., Thom, D., Kautz, M., Martin-Benito, D., Peltoniemi, M., Vacchiano, G., Wild, J., Ascoli, D., Petr, M., Honkaniemi, J., Lexer, M.J., Trotsiuk, V., Mairota, P., Svoboda, M., Fabrika, M., Nagel, T.A., Reyer, C.P.O., 2017. Forest disturbances under climate change. Nat. Clim. Chang. 7, 395–402. https://doi.org/10.1038/nclimate3303

Senf, C., Pflugmacher, D., Hostert, P., Seidl, R., 2017. Using Landsat time series for characterizing forest disturbance dynamics in the coupled human and natural systems of Central Europe. ISPRS J. Photogramm. Remote Sens. 130, 453–463. https://doi.org/10.1016/j.isprsjprs.2017.07.004

Senf, C., Pflugmacher, D., Zhiqiang, Y., Sebald, J., Knorn, J., Neumann, M., Hostert, P., Seidl, R., 2018. Canopy mortality has doubled in Europe's

temperate forests over the last three decades. Nat. Commun. 9, 1–8. https://doi.org/10.1038/s41467-018-07539-6

Senf, C., Sebald, J., Seidl, R., 2021. Increasing canopy mortality affects the future demographic structure of Europe's forests. One Earth 4, 749–755. https://doi.org/10.1016/j.oneear.2021.04.008

Senf, C., Seidl, R., 2020. Mapping the forest disturbance regimes of Europe. Nat. Sustain. 4, 63–70. https://doi.org/10.1038/s41893-020-00609-y

Tickle, S.O., Eckley, I.A., Fearnhead, P., 2021. A computationally efficient, high-dimensional multiple changepoint procedure with application to global terrorism incidence. J. R. Stat. Soc. Ser. A Stat. Soc. 184, 1303–1325. https://doi.org/10.1111/rssa.12695

Truong, C., Oudre, L., Vayatis, N., 2020. Selective review of offline change point detection methods. Signal Processing 167, 107299. https://doi.org/10.1016/j.sigpro.2019.107299

Turner, M.G., 2010. Disturbance and landscape dynamics in a changing world 1. Ecology 91, 2833–2849. https://doi.org/10.1890/10-0097.1

Vacchiano, G., Garbarino, M., Borgogno Mondino, E., Motta, R., 2012. Evidences of drought stress as a predisposing factor to Scots pine decline in Valle d'Aosta (Italy). Eur. J. For. Res. 131, 989–1000. https://doi.org/10.1007/s10342-011-0570-9

Vogelmann, J.E., Gallant, A.L., Shi, H., Zhu, Z., 2016. Perspectives on monitoring gradual change across the continuity of Landsat sensors using time-series data. Remote Sens. Environ. 185, 258–270. https://doi.org/10.1016/j.rse.2016.02.060

Wang, T., Samworth, R.J., 2018. High dimensional change point estimation via sparse projection. J. R. Stat. Soc. Ser. B Stat. Methodol. 80, 57–83. https://doi.org/10.1111/rssb.12243

Wilson, E.H., Sader, S.A., 2002. Detection of forest harvest type using multiple dates of Landsat TM imagery 80, 385–396. https://doi.org/10.1016/S0034-4257(01)00318-2

Wohlgemuth, T., Schwitter, R., Bebi, P., Sutter, F., Brang, P., 2017. Post-

windthrow management in protection forests of the Swiss Alps. Eur. J. For. Res. 136, 1029–1040. https://doi.org/10.1007/s10342-017-1031-x

Wulder, M.A., Loveland, T.R., Roy, D.P., Crawford, C.J., Masek, J.G., Woodcock, C.E., Allen, R.G., Anderson, M.C., Belward, A.S., Cohen, W.B., Dwyer, J., Erb, A., Gao, F., Griffiths, P., Helder, D., Hermosilla, T., Hipple, J.D., Hostert, P., Hughes, M.J., Huntington, J., Johnson, D.M., Kennedy, R., Kilic, A., Li, Z., Lymburner, L., McCorkel, J., Pahlevan, N., Scambos, T.A., Schaaf, C., Schott, J.R., Sheng, Y., Storey, J., Vermote, E., Vogelmann, J., White, J.C., Wynne, R.H., Zhu, Z., 2019. Current status of Landsat program, science, and applications. Remote Sens. Environ. 225, 127–147. https://doi.org/10.1016/j.rse.2019.02.015

Wulder, M.A., Masek, J.G., Cohen, W.B., Loveland, T.R., Woodcock, C.E., 2012. Opening the archive: How free data has enabled the science and monitoring promise of Landsat. Remote Sens. Environ. 122, 2–10. https://doi.org/10.1016/j.rse.2012.01.010

Ye, S., Rogan, J., Zhu, Z., Hawbaker, T.J., Hart, S.J., Andrus, R.A., Meddens, A.J.H., Hicke, J.A., Eastman, J.R., Kulakowski, D., 2021. Detecting subtle change from dense Landsat time series: Case studies of mountain pine beetle and spruce beetle disturbance. Remote Sens. Environ. 263. https://doi.org/10.1016/j.rse.2021.112560

Zhu, Z., 2017. Change detection using landsat time series: A review of frequencies, preprocessing, algorithms, and applications. ISPRS J. Photogramm. Remote Sens. 130, 370–384. https://doi.org/10.1016/j.isprsjprs.2017.06.013

Zhu, Z., Woodcock, C.E., 2014. Continuous change detection and classification of land cover using all available Landsat data. Remote Sens. Environ. 144, 152–171. https://doi.org/10.1016/j.rse.2014.01.011

Zhu, Z., Zhang, J., Yang, Z., Aljaddani, A.H., Cohen, W.B., Qiu, S., Zhou, C., 2019. Continuous monitoring of land disturbance based on Landsat time series. Remote Sens. Environ. 238, 111116. https://doi.org/10.1016/j.rse.2019.03.009

Supplementary material

Table S4.1. Effects of the impulsive noise filter on the user's and producer's accuracy when the CDMT algorithm analysed univariate time series, i.e. individual bands.

Band	User's accuracy (%)			Producer's accuracy (%)		
	Unfiltered	Filtered	Difference	Unfiltered	Filtered	Difference
Blue	6.4	8.1	1.7	10.2	9.6	-0.6
Green	12.4	15.7	3.3	13.4	12.9	-0.5
Red	20.0	25.6	5.6	22.6	21.9	-0.7
NIR	22.3	24.3	2.0	17.5	16.7	-0.8
SWIR1	31.3	33.0	1.7	39.4	36.4	-3.0
SWIR2	34.0	38.6	4.6	54.7	54.3	-0.4
NDVI	27.7	32.0	4.3	37.9	36.5	-1.4
NDMI	39.6	41.8	2.2	77.3	76.0	-1.3
NBR	36.2	40.1	3.9	72.0	72.2	0.2
MSI	38.2	41.1	2.9	78.5	77.8	-0.7
TCB	11.8	14.3	2.5	10.3	10.1	-0.2
TCG	28.8	31.8	3.0	34.2	34.4	0.2
TCW	35.9	40.4	4.5	59.1	59.1	0
TCA	28.2	33.5	5.3	44.2	44.9	0.7

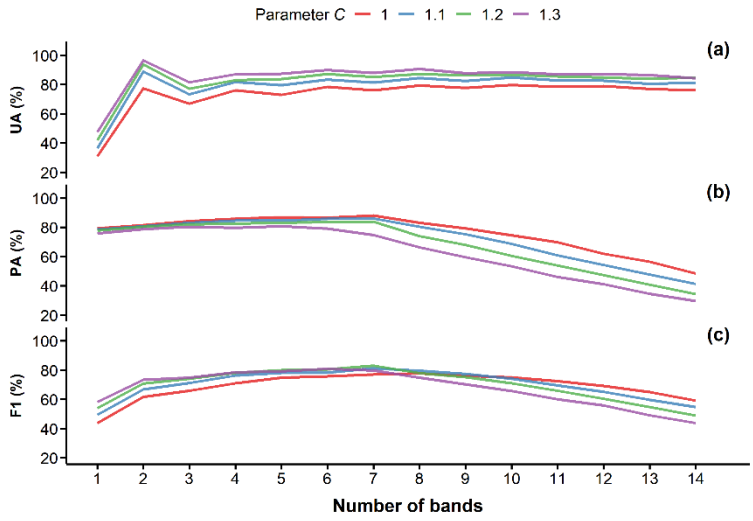

Figure S4.1. Maximum value achieved by each accuracy metrics among all the unique combinations of weighted bands, with a length from one to 14. User's accuracy (UA), Producer's accuracy (PA) and F1 score varied as a function of the number of bands included in the time series. They were also influenced by the parameter *C* that controls the thresholds (λ) employed in the HiTS procedure for detecting changepoints (Equation 4).

Table S4.2. Median weights assigned to each band considering the best performing combination in terms of F1 score. We randomly sampled total of 200000 pixels, equally distributed between undisturbed and disturbed ones.

Band	Disturbed (undisturbed)	Rank
MSI	0.69 (0.56)	1
NDMI	0.69 (0.56)	1
NBR	0.66 (0.51)	2
TCW	0.64 (0.52)	3
SWIR2	0.6 (0.46)	4
TCA	0.55 (0.39)	5
SWIR1	0.53 (0.45)	6

Table S4.3. Maximum value achieved by each accuracy metric among all the unique combinations of weighted bands, with a length from one to 14 and with different values of the parameter *C*. This latter controls the thresholds (λ) employed in the HiTS procedure for detecting changepoints (Equation 4).

	Combination length	**Parameter *C***			
		1	**1.1**	**1.2**	**1.3**
Maximum UA (%)	1	30.9	36.4	41.8	47.5
	2	77.3	88.9	93.8	96.6
	3	67.0	73.3	77.2	81.5
	4	76.1	81.7	82.9	87.0
	5	72.9	79.6	83.7	87.3
	6	78.5	83.4	87.2	90.0
	7	76.0	81.4	85.2	88.0
	8	79.4	84.4	87.2	90.6
	9	77.7	82.5	86.2	87.7
	10	79.7	84.8	86.7	88.6
	11	78.4	82.9	85.5	86.9
	12	78.9	82.7	84.9	87.2
	13	77.0	80.4	83.9	86.5
	14	76.0	81.3	84.7	84.3
Maximum PA (%)	1	79.3	78.5	77.8	75.8
	2	81.4	80.7	80.3	78.8

	3	84.3	83.2	82.1	80.3
	4	86.0	84.6	82.6	79.8
	5	86.9	84.6	83.2	80.7
	6	86.6	85.8	83.6	79.2
	7	88.2	86.1	83.9	74.7
	8	83.2	80.3	74.0	66.3
	9	79.3	75.3	67.9	59.5
	10	74.5	68.7	60.5	53.4
	11	69.8	60.9	53.9	46.1
	12	62.0	54.3	47.2	41.2
	13	56.5	47.7	40.8	34.6
	14	48.5	41.3	34.4	29.6
Maximum F1 (%)	1	43.8	49.5	54.0	58.3
	2	61.8	66.7	70.8	73.4
	3	65.9	71.2	74.1	74.8
	4	71.0	76.3	78.1	78.5
	5	74.8	78.2	79.9	79.2
	6	75.8	78.4	80.6	80.9
	7	77.0	81.2	83.1	79.8
	8	77.8	79.6	78.0	74.8
	9	76.1	77.3	75.2	70.4

	10	75.1	74.2	71.0	65.7
	11	72.5	69.5	66.0	60.0
	12	69.2	65.2	60.4	55.8
	13	65.1	59.7	54.7	49.1
	14	59.2	54.8	49.0	43.8

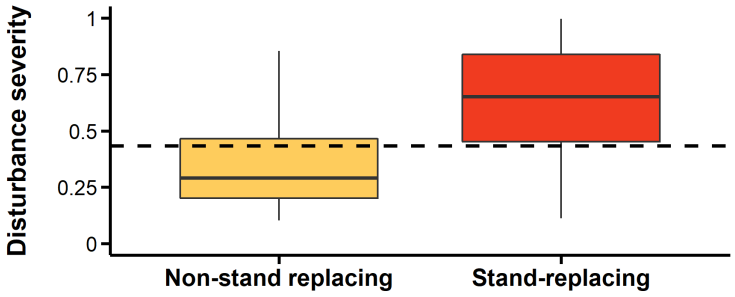

Figure S4.2. Distribution of the disturbance severity of training pixels disturbed either by non-stand replacing or stand-replacing events. Disturbance severity corresponds to the probability predicted by the logistic regression. The horizontal dashed line indicates the a posteriori threshold separating between the probabilities associated with each disturbance severity class.

Chapter 5

Conclusions

The consequences of climate-induced shifts in disturbance regimes have been observed on forest ecosystems at different spatial and temporal scales globally. Therefore, the demand for spatially and temporally explicit information regarding forest disturbance dynamics is rising among researchers and land managers. The research chapters presented in this thesis provide new methodological insights into applications of satellite optical remote sensing for the assessment of forest disturbance dynamics at the landscape scale, including post-fire forest recovery (Chapter 2), burn severity mapping (Chapter 3) and disturbance detection (Chapter 4). Landsat and Sentinel-2 time series proved to be powerful tools for accurately detecting abrupt and gradual changes occurring to forests, from the stand- to the landscape-scale. The novel remote sensing approaches introduced in this thesis were tested in forest landscapes of the Alps and the Apennines. Nevertheless, a crucial aspect to be addressed when developing novel methodologies based on remote sensing data is their applicability to different forest ecosystems and datasets. The implementation of robust mathematical and statistical procedures into these methodologies promotes their transferability to various datasets and geographic areas as well as their operational usage. In this framework, the approaches proposed in this thesis rely on highly generalisable methods, such as the Theil-Sen estimator (Chapter 2), the weighted geometric median (Chapter 3) and the HiTS procedure (Chapter 4). The robustness of these methods was stressed through their application in mountainous landscapes, where unfavourable conditions often hinder multitemporal analyses based on optical remote sensing data. For instance, persistent clouds, snow cover and topographic complexity reduce data availability and introduce noise in the time series, thus limiting the applicability of change detection techniques. Nowadays, the availability of multispectral data with high temporal resolution such as the Harmonized Landsat and Sentinel-2 (HLS) surface reflectance dataset (Claverie

et al., 2018) or PlanetScope imagery (Roy et al., 2021) is increasing. Specifically, PlanetScope imagery provides both high spatial, i.e. 3 m, and temporal resolution, i.e. around 24 hours of revisit time at many locations globally (Roy et al., 2021). The major limitations of the methods proposed in this thesis are related to the relatively low spatial resolution provided by Landsat and Sentinel-2 data as well as the limited frequency of the time series, i.e. annual. Future improvements should be aimed at analysing optical remote sensing data with higher temporal and spatial resolution. While still limited in their whole temporal coverage, multispectral data such as that acquired by the PlanetScope constellation will likely improve the detection and assessment of forest disturbance dynamics. In particular, PlanetScope imagery will allow studying transient phenomena, which occur at spatial scales not resolved by medium resolution satellite images.

Future applications of the approaches proposed in this thesis will concern, for example, the use of phenologically coherent reflectance composites (Chapter 3) in operational projects for burn severity mapping. Similarly, future applications of the CDMT algorithm (Chapter 4) will focus on extending the study area to the regional scale for evaluating the effects of climate change on forest disturbance dynamics in the Alpine region.

References

Claverie, M., Ju, J., Masek, J.G., Dungan, J.L., Vermote, E.F., Roger, J.-C.C., Skakun, S. V., Justice, C., 2018. The Harmonized Landsat and Sentinel-2 surface reflectance data set. Remote Sens. Environ. 219, 145–161. https://doi.org/10.1016/j.rse.2018.09.002

Roy, D.P., Huang, H., Houborg, R., Martins, V.S., 2021. A global analysis of the temporal availability of PlanetScope high spatial resolution multi-spectral imagery. Remote Sens. Environ. 264, 112586. https://doi.org/10.1016/j.rse.2021.112586